

UNIVERSITY OF OSLO  
DEPARTMENT OF PHYSICS

MASTER'S THESIS

---

# Nickel Diffusion and Configuration in Crystalline Zinc Oxide

---

Thomas Neset SKY

*A thesis submitted in partial fulfilment of the requirements  
for the degree of MSc*

*in*

Condensed Matter Physics

May 2014



UNIVERSITY OF OSLO  
Department of Physics

## *Abstract*

Condensed Matter Physics

MSc

### **Nickel Diffusion and Configuration in Crystalline Zinc Oxide**

by Thomas Neset SKY

The main objective of this thesis is to achieve an understanding of the diffusion behaviour and configuration of intentionally introduced Nickel in mono-crystalline Zinc Oxide. The diffusion of Nickel has been examined by secondary ion mass spectrometry, while Fourier transform infrared spectroscopy has been applied to inspect the configuration of the Nickel impurity. An activation energy of 4.3 eV and a pre-exponential factor of  $6 \cdot 10^4 \text{ cm}^2 \text{ s}^{-1}$  have been estimated for the diffusivity. It has been found that the diffusion of Nickel is strongly affected by the oxygen partial pressure, and it is suggested that both a vacancy mediated and an interstitial mechanism are involved in the transition between oxygen-rich and zinc-rich conditions. Infrared absorption lines at 4216, 4240 and 4247  $\text{cm}^{-1}$  have been found to correlate with the measured concentration of Nickel, supporting the previous assignments of these lines as internal electronic transitions of substitutional  $\text{Ni}_{\text{Zn}}^{2+}$ . An absorption strength of  $\epsilon \geq 1.5 \cdot 10^{-17} \text{ cm}$  has been deduced for the  $\text{Ni}_{\text{Zn}}^{2+}$  defect.

# *Acknowledgements*

I would like to express my utmost gratitude to Dr. Klaus Magnus Johansen, who has been my day-to-day supervisor throughout this work. I have greatly appreciated your desire to pass on your knowledge and expertise in this field of science, which has contributed to making these last two years very enjoyable and stimulating. Thank you for your patience when teaching me how to use the SIMS and for revising this thesis; a thesis that had not been possible without your guidance.

I especially want to thank my main supervisor prof. Bengt G. Svensson for introducing me into the field of semiconductor physics, and for guiding me through this endeavor. I am grateful for your clarifying advices and for revising my thesis.

Thank you Heine Nygard Riise for teaching me how to use the magnetron sputtering system, and for carrying out Hall effect Measurements on my samples. I would also like to thank Dr. Vishnukanthan Venkatachalapathy for performing XRD analysis on my samples and assoc. prof. Øystein Prytz for helping me with the SEM measurements.

Finally, a big thanks to everyone at LENS for making MiNaLab such a pleasant place to work.

# Contents

<b>Abstract</b>	<b>i</b>
<b>Acknowledgements</b>	<b>ii</b>
<b>1 Introduction</b>	<b>1</b>
<b>2 Theory and background</b>	<b>3</b>
2.1 Crystals and defects . . . . .	3
2.1.1 Point defects . . . . .	4
2.2 Diffusion in crystalline materials . . . . .	5
2.2.1 Mathematical basis of diffusion . . . . .	5
2.2.2 Microscopic interplay . . . . .	7
2.2.3 Mechanisms of diffusion . . . . .	9
2.3 Infrared spectroscopy . . . . .	11
2.3.1 Vibrational transitions . . . . .	11
2.3.2 Quantitative analysis . . . . .	13
2.4 Crystalline Zinc Oxide . . . . .	14
2.4.1 Crystal structure . . . . .	15
2.4.2 Single crystal growth . . . . .	15
2.4.3 Semiconductor – fundamentals . . . . .	17
2.4.4 Unintentional n-type conductivity . . . . .	18
2.4.5 Residual impurities . . . . .	18
2.5 Previous work – Ni configuration in ZnO . . . . .	19
<b>3 Experimental techniques and procedure</b>	<b>21</b>
3.1 Secondary Ion Mass Spectrometry . . . . .	21
3.1.1 Instrumentation . . . . .	22
3.1.2 The sputtering process . . . . .	22
3.1.3 Mass-to-charge analysis . . . . .	24
3.1.4 Data analysis . . . . .	25
3.2 Fourier Transform Infrared Spectroscopy . . . . .	26
3.2.1 Michelson interferometer . . . . .	26
3.2.2 Formation of the interferogram . . . . .	27
3.2.3 Instrumentation . . . . .	30
3.2.4 Data analysis . . . . .	30
3.3 Four-point probe . . . . .	31

3.4	Magnetron Sputtering . . . . .	33
3.5	Electron Beam Evaporation . . . . .	33
3.6	Experimental procedure . . . . .	34
3.6.1	Samples and methodology . . . . .	35
3.6.2	Introduction of Ni from gas phase . . . . .	37
3.6.3	Introduction of Ni from predeposited NiO-film . . . . .	38
3.6.4	Introduction of Ni from predeposited ZnO:Ni-film . . . . .	39
<b>4</b>	<b>Results and discussion</b>	<b>41</b>
4.1	Ni impurities in as-grown ZnO samples . . . . .	41
4.2	Diffusion profiles – introduced from Ni gas phase . . . . .	41
4.2.1	Doping by Ni-wire . . . . .	41
4.2.2	Doping with a Ni-wire cut into pieces . . . . .	45
4.2.3	Comprehending the diffusive behavior . . . . .	50
4.3	Diffusion profiles – introduced from NiO-film . . . . .	51
4.4	Diffusion profiles – introduced from ZnO:Ni-film . . . . .	53
4.5	IR absorption spectra measured on as-grown samples . . . . .	56
4.6	IR absorption spectra after Ni-introduction . . . . .	58
4.6.1	Ni related absorption lines . . . . .	58
4.6.2	Effect of doping on the IR-transmission in the $\vec{k} \perp \vec{c}$ -direction . . . . .	63
4.6.3	O-H localized vibrational modes . . . . .	65
4.6.4	Thermal stability . . . . .	67
4.7	Ni absorption strength . . . . .	68
<b>5</b>	<b>Summary</b>	<b>72</b>
5.1	Conclusion . . . . .	72
5.2	Suggestions for further research . . . . .	73
<b>A</b>	<b>IR peak intensities</b>	<b>74</b>
<b>B</b>	<b>Process development</b>	<b>76</b>
B.1	NiO-film deposition by E-beam evaporation . . . . .	76
B.2	Ni-doped ZnO film deposition by magnetron sputtering . . . . .	78
<b>C</b>	<b>Documentation of Python script</b>	<b>80</b>
	<b>Bibliography</b>	<b>83</b>

# Chapter 1

## Introduction

The great progress in the quality of life for the past half century is in many respects rooted in the semiconductor industry. Semiconductors have revolutionized the way we communicate, work, treat diseases, and harvest energy. As the early development of the semiconductor technology was founded on silicon, this is still the dominant material in electronics today. Silicon has many beneficial features as a semiconductor, especially in terms of processing and abundance. However, as the electronics industry has advanced, silicon is reaching its theoretical limit in terms of device performance. Moreover, due to its indirect bandgap, silicon is not immediately applicable for optoelectronic devices, as this requires a direct bandgap. There are, however, several other semiconductor materials that possess this characteristic, and one class which is currently in use today as materials for light emitting diodes (LED's), is the III-V compounds (GaAs, InP, InAs etc.). Nevertheless, there is still considerable potential for improvements, and one way to realize this is by wide bandgap semiconductors. Wide bandgap semiconductors have the potential to operate at higher frequencies, temperatures and voltages, which all contribute to an increased efficiency.

Zinc Oxide (ZnO) is a direct and wide bandgap ( $\sim 3.4$  eV [1]) semiconductor that has attracted much attention for short wavelength optical device applications. It has several potential advantages over the currently utilized material for short wavelength optoelectronics, gallium nitride (GaN). Some of these advantages include availability of large area single crystals at relatively low cost, a large exciton binding energy ( $\sim 60$  meV [2]), and being environmentally friendly. ZnO is also an attractive candidate as a transparent conducting oxide (TCO), which could lower the costs and improve the performance of the current solar cells. Moreover, theoretical predictions have shown that ZnO is a promising host material for transition metals (TM's) in order to realize dilute magnetic

semiconductors (DMS), with Curie temperature above room temperature.[3] Such a device would have paved the way for a whole new class of applications, wherein both the carrier charge and carrier spin could be exploited. Nickel (Ni) is a ferromagnetic TM, and Ni-doped ZnO has been considered to be among the candidates in attaining DMS operating at room temperature, even though not yet proven successful experimentally.

There is, however, one major issue with ZnO, which challenges the realization of ZnO based diodes. It has proven to be very difficult to achieve low resistive p-type ZnO, which is necessary in order to take the full advantage of all its features. The reason for this, and its intrinsic n-type conductivity, have long been a contentious subject. Besides, controlling the diffusion of impurities, as well as understanding their preferred configuration, remains a major challenge for ZnO.

In order to prevail over these challenges, and allow ZnO to unfold its unique properties, fundamental research on ZnO is of vital importance. In this thesis, the diffusion and configuration of Ni in hydrothermally grown single crystalline ZnO have been investigated by the use of secondary ion mass spectrometry (SIMS) and Fourier transform infrared spectroscopy (FTIR), respectively. Ni was intentionally introduced into as-grown ZnO bulk material from gas phase, predeposited NiO-film and Ni-doped ZnO-film. By combining the very different, but complementary techniques, SIMS and FTIR, it is possible to study the absorption strength of different Ni-impurity configurations and provide a more direct identification of the defects.

## Chapter 2

# Theory and background

Fundamental concepts of crystalline defects, atomistic diffusion, and vibrational spectroscopy will be expounded in the following sections. The general properties of Zinc Oxide (ZnO), together with previous work conducted on Nickel configuration in ZnO are provided in the closing sections of the chapter.

### 2.1 Crystals and defects

A crystal is a three-dimensional periodic array of identical building blocks, apart from any imperfections and impurities that may accidentally be included or built into the structure.[4] The building blocks are atoms or groups of atoms, and are called the basis which forms a minimum volume cell that preserves translational symmetry, the primitive unit cell. Mathematically, an ideal crystal is constructed by an infinite repetition of the basis, attached to a set of points that forms a lattice.

At finite temperature ( $T > 0$  K) intrinsic imperfections will inevitably be present in the crystal as this maximizes the entropy. Such deviations in the crystal structure are called defects, which may exist as a single point defect or extend in 1- 2- or 3-dimensions. The extended defects play an essential role in semiconductors, as they can act as sources and sinks for point defects. However, it is beyond the reach of this project to quantify this mechanism, and thus only the point defects will be expounded in this text. For a survey of defects extended in space (e.g., dislocation loops, grain-boundaries etc.), the reader is referred to the text by Holt and Yacobi [5].



### 2.1.1 Point defects

The most common point defects in crystals are vacant lattice sites (vacancies), extra atoms displaced from regular lattice position (interstitials), and impurities of another element. In compound semiconductors (e.g., ZnO), an additional point defect is possible when host atoms of different element exchange positions. This is called an antisite defect.

The nomenclature commonly used for describing point defects is:  $X_s^q$ , where  $X$  is the species (e.g., a host atom, an impurity atom, or a vacancy),  $s$  is the lattice site at occupation, and  $q$  corresponds to the electronic charge of the species relative to the site it occupies. The vacancy is represented by the symbol  $V$ , such that a neutral vacancy situated at a Zn-site in a ZnO crystal is designated by  $V_{Zn}^0$ . Moreover, if the species is located in an interstitial position the symbol  $i$  is used.

The simplest point defect is the vacancy, in which a single atom is missing from a lattice site. The vacancies can be formed by two mechanisms. One possibility is by an atom transferring from its lattice site to a lattice site on the surface or to a lattice site in an extended defect. This leaves a vacancy behind and is known as a Schottky defect. The other mechanism is by transferring an atom from its lattice site to an interstitial position. This mechanism will create an interstitial defect in addition to the vacancy, and is called a Frenkel defect pair. Furthermore, if the crystal is a compound material, there can be two, or more, kind of vacancies, one for each component that may be in various charged states.

The probability  $W$  that a given site is vacant is proportional to the Boltzmann factor for thermal equilibrium:  $W \propto \exp(-G_f/k_B T)$ , where  $G_f$  is the energy required to form a vacancy and  $k_B$  is the Boltzmann constant ( $8.617 \cdot 10^{-5}$  eVK<sup>-1</sup>)[6], with  $T$  as the absolute temperature. If there are  $N$  atoms, the equilibrium number of vacancies,  $n$ , is given by[4]

$$\frac{n}{N - n} \propto e^{-(G_f/k_B T)}. \quad (2.1)$$

Another possible point defect is the interstitial defect, where an extra atom occupies space between the normal lattice sites. They can be formed from the aforementioned Frenkel process, or they can form by migration of atoms from the surface or from other bulk sources. When the interstitial defect is a host atom, it is termed a self-interstitial. Interstitial defects are generally high energy configurations, at least in the case for a closed packed structure as the wurtzite ZnO. Nevertheless, this configuration may be energetically favourable at certain conditions, and especially when dealing with small-sized impurities like hydrogen and lithium.

Impurity atoms may occur either as interstitials or in the place of normal atoms (substitutional). Since the impurity by definition is of a different radii than the host atoms, a local strain or stress will arise also in the substitutional case. Moreover, if the atom that is substituting the host atom is of a different oxidation state, it will change the local electronic band structure. This aliovalent substitution is precisely what is being done when modifying semiconductor materials.

## 2.2 Diffusion in crystalline materials

Diffusion in solid-state materials is a kinetic process that leads to homogenization of the involved elements. The mixing occurs only at the atomic or molecular level, as opposed to fluids where the mixing may occur on many length scales due to macroscopic flow. To a first approximation, diffusion can be well described in the classical picture by considering some of the transport laws in physics. However, in many cases this facile description does not hold and an understanding of the microscopic interplay, and thus a thermodynamical picture, is necessary. These two modelling procedures will be expounded in the next two subsections.

### 2.2.1 Mathematical basis of diffusion

In order to predict the evolution of diffusion one has to obtain a model that correlates with the actual measured diffusion profile gathered by any microsectioning technique (e.g., SIMS as will be described in section 3.1). One way of developing such a model is to consider the diffusion in a macroscopic view and ignore what is happening on the atomic scale. This is what Adolf Fick did in his experiments on a salt-water system undergoing diffusion in 1855.[7] Based on empirical observations and an intuition that diffusion could be described by the same mathematical formalism as Fourier's law of heat conduction, he was able to describe diffusion by differential equations that sufficiently predicted the evolution of diffusion. These equations are now well established phenomenological laws in any area that are concerned with transport of mass.

In one dimension and under the assumption of steady state, Fick's first law relates the flux density  $J$  to the concentration  $C$ [8]:

$$J = -D \frac{\partial C(z)}{\partial z}, \quad (2.2)$$

where  $D$  is the diffusion coefficient or diffusivity in dimensions of  $\text{cm}^2\text{s}^{-1}$ . This law is analogous to Fourier's law of heat flow and Ohm's law for flow of electric charge, discovered in the same epoch.

To describe diffusion in non-steady state conditions, that is, when the flux is dependent on time, one must combine Eq. 2.2 with an equation for material balance. This is the equation of continuity[9]:

$$\frac{\partial J}{\partial z} = -\frac{\partial C(z, t)}{\partial t}. \quad (2.3)$$

Combining Fick's first law (Eq. 2.2) and the equation of continuity (Eq. 2.3) gives,

$$\frac{\partial C(z, t)}{\partial t} = -\frac{\partial J}{\partial z} = \frac{\partial}{\partial z} \left( D \frac{\partial C(z, t)}{\partial z} \right). \quad (2.4)$$

This second order partial differential equation is a general diffusion equation. It can only be solved analytically when the diffusivity ( $D$ ) is independent on the concentration. Then Eq. 2.4 can be written as

$$\frac{\partial C(z, t)}{\partial t} = D \frac{\partial^2 C(z, t)}{\partial z^2}, \quad (2.5)$$

which is known as Fick's second law. There are different analytical solutions to this linear diffusion equation (Eq. 2.5), for different initial and boundary conditions. One type of solution occurs when the source is fixed at the surface of the material for all times greater than zero. This situation is commonly known as the semi-infinite source model, and the boundary conditions (one for time and two for position) are

$$\begin{aligned} C(z, 0) &= 0 \\ C(0, t) &= C_s \\ C(\infty, t) &= 0 \end{aligned} \quad (2.6)$$

The solution for these conditions is given by[10]

$$C(z, t) = C_s \text{erfc} \left( \frac{z}{2\sqrt{Dt}} \right), \quad t > 0 \quad (2.7)$$

where  $C_s$  is the fixed surface concentration and  $\text{erfc}$  is the complementary error function ( $\text{erfc}(z) = 1 - \text{erf}(z)$ ).

Another solution to Eq. 2.5 is the limited source model, where the source is finite. In this case the boundary conditions are

$$\begin{aligned}
 C(z, 0) &= 0, \quad z \neq 0 \\
 \frac{dC(0, t)}{dz} &= 0 \\
 C(\infty, t) &= 0 \\
 \int_0^\infty C(z, t) dz &= Q_T = \text{constant}
 \end{aligned} \tag{2.8}$$

where  $Q_T$  is the initial amount of impurity. The solution for these conditions is a Gaussian centered at  $z = 0$ [10]:

$$C(z, t) = \frac{Q_T}{\sqrt{\pi Dt}} e^{-\frac{z^2}{4Dt}}, \quad t > 0 \tag{2.9}$$

The derivation of Eq. 2.7 and Eq. 2.9 are perhaps most easily done by using Laplace transforms to reduce the linear diffusion equation to an ordinary differential equation. A derivation following this approach can be found in the text by Glicksman [11].

### 2.2.2 Microscopic interplay

Instead of approaching an understanding of diffusion in a phenomenological manner, a much more grounded way is a physical and atomistic approach, by considering the random walk of the diffusing particles. The mathematical form of a random walk was derived by Albert Einstein in 1905.[12] He found a fundamental relation between the macroscopic quantity, the diffusivity ( $D$ ), and the microscopic quantity, the mean square displacement in a given time ( $\langle R^2(t) \rangle$ ):

$$D = \frac{\langle R^2(t) \rangle}{6t}. \tag{2.10}$$

It is well accepted that diffusion in solids is normally a thermally activated process, and ever since Kirkendall's experiment in 1947 the consensus has been that diffusion involves atomic exchange with intrinsic lattice imperfections. As intrinsic lattice imperfections are related to the entropy, thermodynamics of irreversible processes must be considered.

Figure 2.1 shows the energy barrier as a function of atomic position  $a$  for a jumping atom. A successful jump is conducted when an atom gathers the Gibbs free energy  $G_m$  to migrate over the barrier and reside on an equivalent equilibrium position by an exchange with a vacancy defect. The probability  $W$  that the atom acquires the energy

$G_m$  is given by the Boltzman factor as

$$W = \nu e^{-G_m/k_B T}, \quad (2.11)$$

where  $\nu$  is the vibration frequency ( $\approx$  the Debye frequency).[13] In addition, a successful jump also depends on whether the neighbor lattice site is vacant or not. The probability  $N_d$  that the site is occupied by a vacancy defect is

$$N_d = Z e^{-G_f/k_B T}, \quad (2.12)$$

where  $Z$  is a coordination factor depending on the crystal structure, and  $G_f$  is the Gibbs free energy of formation required to form the vacancy defect.[13] Multiplying the probability for migration and formation (Eq. 2.11 and Eq. 2.12, respectively), this provides the jump frequency  $\Gamma_s$ :

$$\Gamma_s = W N_d = Z \nu e^{-(G_m+G_f)/k_B T}. \quad (2.13)$$

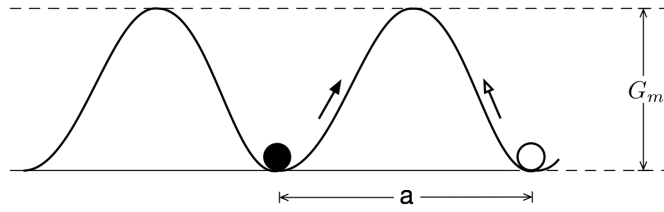


FIGURE 2.1: Energy-distance diagram for lattice diffusion.  $a$  is the atomic spacing and  $G_m$  is the free energy. Edited from [13].

For the three dimensional case and for a hexagonal close-packed structure there are two values of the jump frequency  $\Gamma_s$ , referring to jumps in the basal plane ( $\Gamma_1$ ) and out of the basal plane ( $\Gamma_2$ ), respectively. For the x and y directions the diffusion coefficient is expressed as[9]

$$D_{x,y} = \frac{a^2}{2} (3\Gamma_1 + \Gamma_2), \quad (2.14)$$

while for the z-axis as

$$D_z = \frac{3}{4} \Gamma_2 c^2, \quad (2.15)$$

where  $c$  is the atomic spacing in the z-direction, and under the assumption that the z-axis is parallel to the c-direction of the lattice. Considering only diffusion along the c-direction of the lattice, the diffusion coefficient ( $D$ ) can then be written as

$$D = \frac{3}{4} c^2 Z \nu e^{-(G_m+G_f)/k_B T}. \quad (2.16)$$

The Gibbs free energy ( $G$ ) relates to another thermodynamic potential, the Helmholtz free energy ( $H$ ), through[14]

$$G = H - TS, \quad (2.17)$$

where  $H$  is a measure of the total energy of the system (enthalpy) and  $S$  is the entropy. Using this, the diffusion coefficient (Eq. 2.16) can be expressed as

$$D = \frac{3}{4}c^2Z\nu e^{(S_m+S_f)/k_B} \times e^{-(H_m+H_f)/k_BT}, \quad (2.18)$$

or

$$D = D_0 e^{-(E_a/k_BT)}, \quad (2.19)$$

with  $D_0 = (3/4)c^2Z\nu e^{(S_m+S_f)/k_B}$  and  $E_a = H_m + H_f$ .

Eq. 2.19 is commonly known as the Arrhenius relation, after the swedish scientist Svante A. Arrhenius. It can be used to model the temperature variation of diffusion coefficients, and further estimate a value for the activation energy  $E_a$ . Moreover, if the crystal structure is known, it is also possible to evaluate the total entropy,  $S = S_m + S_f$ , from the prefactor  $D_0$ .

### 2.2.3 Mechanisms of diffusion

The way atoms migrate in a lattice depends on the crystal structure, the size of the diffuser atom relative to the host atoms and whether or not a defect-assisted process is required. Thus, diffusion in solid-state materials is a process sensitive to many factors. Figure 2.2 illustrates the fundamental mechanisms by which migration can take place in a simple cubic structure.

The direct interchange mechanisms (3) and (4) are two somewhat improbable events. The strong repulsion of the surroundings would hinder the occupation of the intermediate position where the two atoms would be at mid-path in a direct exchange mechanism (4). On the other hand, these repulsive forces would play a positive role for the ring-mechanism (3). However, no net mass transport in a given direction could be possible by such a ring-mechanism.

A far more energetically favorable diffusion mechanism involves point defects. If a lattice site is unoccupied, a neighboring atom can migrate to this site and leave behind a vacancy. This is the vacancy mechanism (1). However, a sufficient supply of vacancies is required for this mechanism to be dominant. In pure solids, the principal source of vacancies is the surface of the material and the formation of vacancies may thus be limited. On the other hand, semiconductors normally carry more structural bulk defects

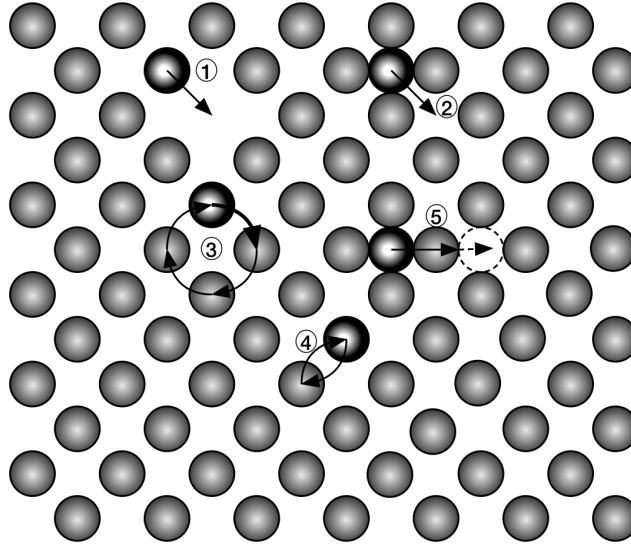


FIGURE 2.2: Schematics of the principal diffusion mechanisms: 1) vacancy mechanism, 2) interstitial mechanism, 3) ring mechanism, 4) direct exchange, 5) interstitialcy mechanism. Edited from [9].

(extended defects formed at processing) which may act as additional sources of vacancies and thereby lower the effective formation energy ( $G_f$ ) for vacancies.

Another mechanism involving point defects is the interstitial mechanism (2), where an interstitial atom is jumping between interstitial sites. An atom residing on an interstitial site encounters local repulsion from the nearby lattice atoms. For the atom to jump to a neighboring interstitial site, it has to overcome these repulsive forces by acquiring the migration energy  $G_m$ . Contrary to the vacancy mechanism, an interstitial atom does not require the formation of a defect to migrate. Thus, the activation energy for an already formed interstitial atom to migrate is just the enthalpy of migration:  $E_a = H_m$ , which indicates that the interstitial mechanism should be a rapid process. However, the strong repulsions from the surrounding lattice atoms typically imply high activation energies for interstitial diffusion to occur. Nevertheless, the interstitial mechanism is an important diffusion mechanism in solid-state materials that often dominates when the diffuser is sufficiently small compared to the host atoms.

A variant of the interstitial mechanism is the interstitialcy mechanism (5), also called the indirect interstitial mechanism, wherein the jump of a substitutional atom is assisted by the arrival of an interstitial atom. The nearby interstitial atom may kick-out the substitutional atom, placing it in the interstitial position, which then again replaces a neighboring lattice atom.

To perceive which mechanism of diffusion that dominates for a diffuser in a crystal, one can start out by modelling the experimental diffusion profiles, obtained by e.g. Secondary Ion Mass Spectrometry, to the general diffusion equation (Eq. 2.4). This will give a value for the diffusivity ( $D$ ) of the diffuser. By repeating this procedure for several temperatures it is then possible to obtain the activation energy ( $E_a$ ) for the diffuser from Eq. 2.19, which reflects the dominant diffusion mechanism in the crystal.

## 2.3 Infrared spectroscopy

Absorption of electromagnetic radiation is the exchange of energy from photons to matter. The energy can be taken up by the matter either by a change in a molecular dipole moment, electronic transitions, compton scattering or photoionization. The infrared (IR) region of the electromagnetic spectrum corresponds approximately to wavelengths spanning from 700 nm to 1 mm, or an energy in the range 1.24 meV - 1.7 eV. This is in the range of energies separating the quantum states of molecular vibrations, and thus makes IR spectroscopy a competent method for investigating the chemical composition of semi-transparent solid-state materials.

### 2.3.1 Vibrational transitions

A molecule composed of  $N$  atoms have  $3N$  degrees of freedom, 3 of which represents translational motion in mutually perpendicular directions and 3 representing rotational motion, the remaining  $3N - 6$  degrees of freedom are vibrational modes.[15] In a solid-state material the rotational and translational modes will not be available for excitation and only the vibrational modes may be considered.

In the simple case of a diatomic molecule, the displacements of the two atoms from their equilibrium positions can be approximated as a harmonic oscillator. That is, for small displacements the force ( $F$ ) is proportional to the displacement ( $q$ ) as described by Hook's law:  $F = -kq$ , where  $k$  is the force constant in units of N/m.[16] The vibration ( $q(t)$ ) may be described by using Newtons second law, and gives a quite accurate description of the molecular vibrations. However, this approach will fail to describe the interaction with light. For this a quantum mechanical approach is required.

The total energy or Hamiltonian ( $\hat{H}$ ) of a diatomic molecule with effective mass  $M$  and an effective force constant  $K$  is given by

$$\hat{H}(Q) = \frac{1}{2M}\hat{P}_Q^2 + \frac{K}{2}\hat{Q}^2, \quad (2.20)$$



where  $\hat{Q} = Q$  is the length of the normal coordinate (the change in bond length from its equilibrium value) and  $\hat{P}_Q = -i\hbar \frac{\partial}{\partial Q}$  is the momentum operator associated with the normal coordinate. The time-independent Schrödinger equation for this system may be expressed by

$$\hat{H} |\psi\rangle = E_{vib} |\psi\rangle, \quad (2.21)$$

where  $|\psi\rangle$  is the energy eigenstate and  $E_{vib}$  is the energy level. Substituting for the operators then yields:

$$-\frac{\hbar^2}{2M} \frac{d^2\psi(Q)}{dQ^2} + \frac{K}{2} Q^2 \psi(Q) = E_{vib} \psi(Q) \quad (2.22)$$

or rearranged,

$$\frac{d^2\psi(Q)}{dQ^2} + \frac{2M}{\hbar^2} \left( E_{vib} - \frac{K}{2} Q^2 \right) \psi(Q) = 0. \quad (2.23)$$

The differential equation (Eq. 2.23) may be solved by a 'brute force' power series method to produce wavefunctions constructed by Hermite polynomials. The vibrational energies  $E_{vib}$  are also found by solving the Schrödinger equation and the energies are restricted to discrete values[16]:

$$E_{vib} = \hbar\omega \left( n + \frac{1}{2} \right), \quad n = 0, 1, 2, \dots \quad (2.24)$$

where  $\hbar$  is the reduced Planck's constant ( $1.0546 \cdot 10^{-34}$  Js)[6],  $\omega = \sqrt{K/M}$  is the oscillator frequency and  $n$  represents the different eigenstates. Only transitions from one eigenstate to another are allowed, and thus these energy states describe the molecules ability to absorb light. In spectroscopy it is common to represent a wave by its spatial frequency in cycles per unit distance, wave number  $\tilde{\nu}(\text{cm}^{-1})$ , given by

$$\tilde{\nu} = \frac{1}{\lambda} = \frac{\omega}{2\pi c}, \quad (2.25)$$

where  $\lambda$  is the wave length and  $c$  is the speed of light ( $2.9979 \cdot 10^{10}$  cm/s)[6]. The energy of light is given as  $E = \hbar\omega$ , such that the wave number is proportional to the energy as  $E = 1.24 \cdot 10^{-4} \tilde{\nu}$  eVcm.

Electromagnetic waves can only interact with vibrational modes that are associated with a time-varying electric dipole moment. Consequently, symmetrical stretch modes like that of the  $\text{N}_2$ -molecule cannot be observed by IR-spectroscopy. These modes can, however, be observed by a complementary technique, referred to as Raman spectroscopy, which uses a laser to excite modes by inelastic scattering.

When a crystal is exposed to IR-light the whole lattice is affected and a collective excitation of vibrational modes will form. This collective excitation is called phonons and

they are quasi-particles which carry lattice vibrations throughout the crystal. The atoms may vibrate normal to- or in the same direction as the propagating wave, representing transversally- and longitudinally polarized phonons, respectively. Moreover, for crystals with two (or more) elements in the primitive unit cell, the elements may vibrate in phase or out of phase, corresponding to acoustical- and optical modes, respectively.

ZnO has four atoms in the primitive unit cell, and thus results in 12 different types of phonons: three longitudinal optical (LO), six transverse optical (TO), one longitudinal acoustic (LA) and two transverse acoustic (TA) modes.[2] The addition of impurities to a host crystal will perturb the lattice symmetry and introduce new vibrational modes. New modes with a wave number within the vibrational bands of the unperturbed lattice are termed band modes, while modes with higher wave number than the maximum band are called localized vibrational modes (LVM). These high-frequency LVM's have become an important probe of light-impurity defects in solid-state materials that provides information about defect structure and properties that often cannot be obtained by other methods.

### 2.3.2 Quantitative analysis

As radiation is transmitted through a sample, the intensity of the radiation decreases relative to that at the front face,  $I_0$ , with thickness  $d$  (cm) as

$$I(\tilde{\nu}) = I_0(\tilde{\nu})e^{-\alpha(\tilde{\nu})d}, \quad (2.26)$$

where  $\alpha(\tilde{\nu})$  is the linear absorption coefficient ( $\text{cm}^{-1}$ ) at  $\tilde{\nu}$ . [15] This attenuation is known as the Bouguer-Lambert-Beer law and is a fundamental law of quantitative spectroscopy. For a solid sample the beam may also be reflected from both the front and back surfaces, where the latter may also give rise to multiple internal reflections. Including reflectance  $R$ , the transmittance of the sample is given by [17]

$$T(\tilde{\nu}) = \frac{I(\tilde{\nu})}{I_0(\tilde{\nu})} = \frac{(1 - R)^2 e^{-\alpha(\tilde{\nu})d}}{1 - R^2 e^{-2\alpha(\tilde{\nu})d}}. \quad (2.27)$$

For ZnO,  $R$  is found to be  $\sim 0.11$  in the IR range.[17] Moreover, as  $e^{-2\alpha(\tilde{\nu})d} \leq 1$  for all  $\tilde{\nu}$  then the term  $R^2 e^{-2\alpha(\tilde{\nu})d}$  in the denominator in Eq. 2.27 will be a relatively small number, and may be excluded without introducing any significant error. Furthermore, in a linear regime one may write the absorption coefficient as  $\alpha = \alpha_1 + \alpha_2$ , where  $\alpha_1$  is the absorption from the host crystal and the free charge carriers, while  $\alpha_2$  is the defect

related absorption. By doing this, Eq. 2.27 is simplified to:

$$T(\tilde{\nu}) = (1 - R)^2 e^{-\alpha(\tilde{\nu})d} = (1 - R)^2 e^{-(\alpha_1(\tilde{\nu}) + \alpha_2(\tilde{\nu}))d} = C(\tilde{\nu}) e^{-\alpha_2(\tilde{\nu})d}. \quad (2.28)$$

The factor  $C(\tilde{\nu}) = (1 - R)^2 e^{-\alpha_1(\tilde{\nu})d}$  is assumed to only vary slowly as a function of the wave number, while the absorption from point defects may be seen as sharp peaks at low temperature, thereby enabling LVM's to be measured in simple terms.

The absorption coefficient for a defect  $i$  can in turn be written as a product of an absorption strength  $\epsilon$  and the absorbing defect concentration  $c_i$ . The absorbance is defined as

$$A(\tilde{\nu}) = -\ln(T(\tilde{\nu})), \quad (2.29)$$

such that the absorbance becomes linear with  $c$ ,

$$A(\tilde{\nu}) = -\ln(C(\tilde{\nu})) + \alpha_2(\tilde{\nu})d = \epsilon cd. \quad (2.30)$$

Since the absorption peaks for a defect  $i$  have a finite width, one usually defines the absorption strength  $\epsilon$  as

$$\epsilon_i = \frac{\int_a^b \alpha_i(\tilde{\nu}) d\tilde{\nu}}{c_i}, \quad (2.31)$$

where  $a$  and  $b$  cover the peak range. The total concentration of impurity that is found to contribute to the defect can be measured by a microsectioning technique like Secondary Ion Mass Spectrometry, while the integrated absorption coefficient for the defect can be quantified by infrared spectroscopy. Together, this will provide a lower limit of the absorption strength for the defect.

## 2.4 Crystalline Zinc Oxide

Zinc Oxide (ZnO) is a group II-VI compound semiconductor, normally grown in the wurtzite structure. ZnO is a promising material for short-wavelength optoelectronic devices due to its direct and wide bandgap of  $\sim 3.4$  eV at room temperature.[1] It is easily made n-type, making it an attractive candidate as a transparent conductive oxide (TCO), photodetector, and transparent thin film transistor. Another interesting property of ZnO is its large exciton binding energy ( $\sim 60$  meV) which could lead to lasing based on exciton recombination above room temperature. It is abundant and regarded as an environmentally safe and biocompatible alternative to other wide bandgap semiconductors, like GaN. An additional advantage of ZnO over GaN is the availability of large single crystals. Moreover, theoretical predictions suggest that room-temperature

carrier-mediated ferromagnetism should be possible in ZnO [3], enabling spintronic applications.

### 2.4.1 Crystal structure

At ambient conditions, the thermodynamically stable phase of ZnO is the hexagonal wurtzite structure where each Zn-ion is surrounded by four O-ions at the corners of a tetrahedron, and vice versa, as shown in Figure 2.3. The hexagonal unit cell of the wurtzite structure is described by the lattice parameters  $a$  and  $c$ . Experimental observations of the lattice parameters are found to be  $a = 3.25 \text{ \AA}$  and  $c = 5.21 \text{ \AA}$ . [2] The ratio between  $c$  and  $a$  for an ideal hexagonal closed packed structure ( $c/a = \sqrt{8/3} = 1.633$ ) deviates from the actual ratio ( $c/a = 1.60$ ). This distorted wurtzite structure, together with the partly ionic nature of the bonds give rise to a net dipole moment. This polarity causes ZnO to show a strong piezo-electric effect, and the two polar surfaces are referred to as O-face and Zn-face.

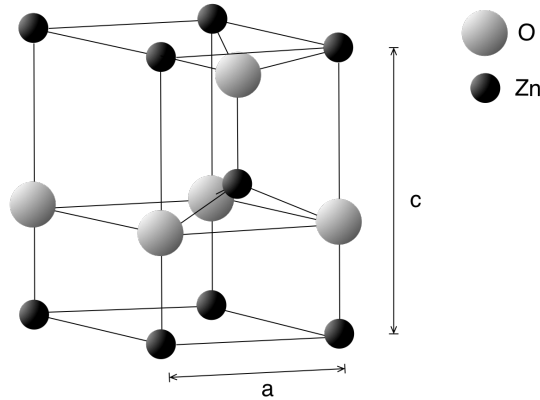


FIGURE 2.3: Illustration of the wurtzite ZnO structure.

### 2.4.2 Single crystal growth

There are various growth techniques to obtain oxide single crystals, and the crucial parameters are control of the temperature gradients and the purity of the precursors. The main procedures for growing single crystal ZnO bulk are the melt growth, seeded chemical vapor transport, and the hydrothermal (HT) growth method.

For the melt growth method, ZnO powder is used as the starting material. The ZnO powder is heated above  $1975^\circ\text{C}$  using radio frequency induction heating, under an over-pressure of oxygen. Once the molten state is attained the temperature is slowly lowered to allow crystallization of the melt. The melt growth is a challenging technique due

to the extreme growth conditions. Moreover, large temperature gradients arise during growth which result in materials with residual strain. However, materials of reasonable quality is made by this method with growth rates as high as 5 mm/h [18].

A method which produces very high quality single crystal ZnO bulk materials is the seeded chemical vapor transport method. The reaction takes place in a horizontal sealed tube. At one end of the tube ZnO powder is heated to 1150°C, while a single crystal seed is kept in the other end at a lower temperature of about 1100°C. Hydrogen is used as a transport agent to increase the growth rate. Hydrogen reacts with the ZnO powder, forming zinc and water vapor which is then transported to the cooler part of the reactor where the single crystal is formed due to the reverse reaction. The drawback of this method is the comparatively low growth rate of about 1mm/day that results in high costs of the wafers.[18].

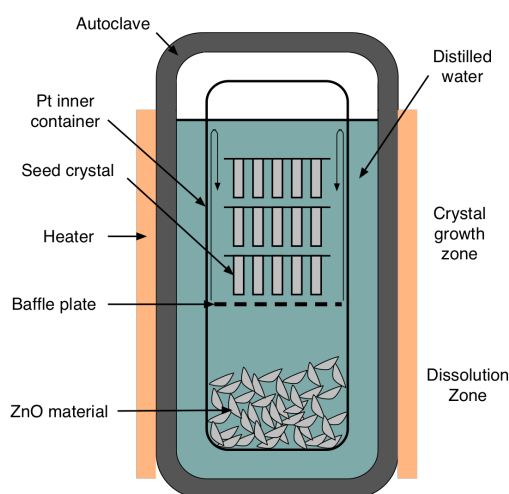


FIGURE 2.4: Schematic of the hydrothermal growth system. The inner container is filled with an aqueous solution of LiOH and KOH. A small temperature difference is maintained between the dissolution zone and crystal growth zone, resulting in convection transport of ZnO towards the seeds. Edited from [19].

In HT-growth, an aqueous solution containing LiOH and KOH are used under elevated temperature and pressure to dissolve and recrystallize ZnO material of high purity. The growth takes place inside a sealed autoclave fitted with a sealed inner container that is normally made of Pt, as illustrated in Figure 2.4. The ZnO feedstock are placed in the bottom part while ZnO seeds are positioned in the upper part. The inner container prevents contamination from the autoclave which is heated up to temperatures of 300°C to 400°C at pressures ranging from 80 MPa to 100 MPa.[19] A temperature difference of typically 5 – 30°C is maintained between the lower part (hot) and upper part (cold), which results in convection transport of ZnO towards the seeds.[18]. To ensure a constant mass flow, a baffle plate separating the feedstock and the seeds is incorporated. The aqueous solution is retained at conditions that are above the critical point of water.

This increases the waters acidity, which favors ionic processes. However, mineralizers are needed to increase the solubility, and a mixture between LiOH and KOH has been found to give the best crystalline quality. HT ZnO shows very good crystalline quality and the technique is relatively easily scalable. However, the presence of the mineralizers will inevitably contaminate the crystal and may strongly affect its electrical properties. Especially, Li is found to contaminate the resulting material. In this work, HT ZnO samples from the commercial producer Tokyo Denpa have been used.

### 2.4.3 Semiconductor – fundamentals

The atom comprises a heavy nucleus surrounded by electrons that are bound to the nucleus by the electromagnetic force. Two electrons can not occupy the same state (i.e., Pauli exclusion principle), thus the individual electrons occupy different atomic orbitals<sup>1</sup>. When a large number of atoms come together in a solid, each of the atomic orbitals splits into a large number of closely spaced energy levels, effectively forming a continuum, or band, of allowed levels.[20] These bands originate from different molecular orbitals, and may or may not overlap, depending on the electronic properties of the atoms and the strength of the bonding between them. The highest occupied band (in terms of energy) which contains the valence electrons, is called the valence band (VB), and the lowest unoccupied band is called the conduction band (CB). In the case when the (VB) is partially full, or if it overlaps in energy with the (CB), the solid is a metal. If, however, the (VB) is completely full and separated from the (CB), the solid is a semiconductor or an insulator. Consequently, a crystal structure where all the valence electrons are used in bonding is likely to form a semiconductor or an insulator. The difference between semiconductors and insulators is simply the size of the bandgap (i.e.,  $\sim 0.5 - 4$  eV for semiconductors and higher for insulators).

In semiconductors, the materials ability to conduct current depends mainly on the number of available charge carriers. Charge can be transported both by electrons in the (CB) or by holes<sup>2</sup> in the (VB). The semiconductor is said to be n-type if electrons are the main charge carriers, and p-type if the holes are the main charge carriers. Electrons and holes may also be intentionally introduced (doping) into the semiconductor from heterovalent impurities. The ability to locally introduce a large amount of charge carriers by doping, is an unique feature of semiconductors, and is the basis for the existence of all solid-state electronic devices.

<sup>1</sup>Electrons can have spin up or spin down, so two electrons with different spins (singlet configuration) can occupy any given orbital.

<sup>2</sup>A hole is a quasiparticle, referring to the situation where an electron is missing in the valence band.

#### 2.4.4 Unintentional n-type conductivity

Regardless of growth technique used, as-grown ZnO crystals reveal unintentional n-type conductivity. In fact, almost all semiconducting oxides are naturally n-type. The reason for this conductivity has long been a controversial subject.

From fundamental principles of electronic structures, this asymmetry can be argued. In ZnO, the valence band is composed of oxygen 2p-orbitals, which have a very low energy. Of course, this energy is modified when chemical bonding occurs in the oxide, but the valence band still tends to show a low energy.[21] This implies that the valence-band maximum (VBM) in ZnO lies far below the vacuum level (over 3 eV lower than the VBM for Si)[22]. Such a low energy of the VBM would require acceptor dopants with similarly low-energy atomic orbitals to provide holes into the valence band, which are not easily identified. Conversely, the conduction-band minimum (CBM) of ZnO corresponds to fairly large electron affinities, thus explaining the propensity of ZnO to exhibit n-type conductivity.[21]

Native point defects have long been speculated to be the origin of the unintentional n-type conductivity. Especially, based on the alteration on the electrical conductivity observed for different oxygen partial pressures led to the idea that  $V_O$  could be the source of this conductivity.[21] Later on, Kohan et al. [23], and Janotti and Van de Walle [24] concluded from density-functional-theory calculations that  $V_O$  is a deep double donor in ZnO, incapable of causing n-type conductivity. Another native defect in ZnO that acts as a donor is the zinc antisite ( $Zn_O$ ). However, this defect is found to have a high formation energy and is unlikely to be present in as-grown ZnO. The same argument holds for  $Zn_i$ , another shallow donor in ZnO. It is found to have a high formation energy in n-type material, and a migration barrier as low as 0.57 eV [24], ensuing diffusion even at room temperature. Thus, any nonequilibrium concentrations of  $Zn_i$  will easily diffuse out of the crystal or be trapped by other defects/impurities.

Without any accountable native point defects to answer for the inherent n-type conductivity in as-grown ZnO, it may be that the cause is due to residual impurities incorporated during growth.

#### 2.4.5 Residual impurities

Impurities that are present in as-grown ZnO single crystals at relatively high concentration ( $> 10^{15} \text{ cm}^{-3}$ ) can contribute to its electrical performance. Which residual impurities that are the most abundant will depend on the growth method. Some impurities, like H, Si, Mg and Al are common for all the three growth methods discussed

in Section 2.4.2, while Li is mainly found in HT-grown ZnO.[18] That Li is present in significant concentrations ( $\sim 10^{17}\text{cm}^{-3}$ ) in HT ZnO is as expected, since it is an important contributor in the growth process. Li can act both as a donor and an acceptor, depending on the atomic configuration.  $\text{Li}_{\text{Zn}}$  is found to be a shallow acceptor [25], while  $\text{Li}_i$  acts as a donor [26]. Vines et al. [27] provided strong evidence that Li in HT ZnO almost exclusively reside in the substitutional configuration ( $\text{Li}_{\text{Zn}}$ ), and thus act as an important acceptor in HT ZnO.

H, Al and Si are all residual impurities in HT ZnO and may all increase the donor activity. There is a plethora of evidence that H is at least partially responsible for the native n-type conductivity. A likely scenario is that a combination of several residual impurities is the source of the n-type activity in ZnO.

Ni is usually not present in significant concentration in HT-grown ZnO. A concentration of  $< 10^{15}\text{cm}^{-3}$  is typically observed for HT ZnO manufactured by Tokyo Denpa.[18] From density-functional calculations, Wardle et al. [28] have concluded that  $\text{Ni}_{\text{Zn}}$  may contribute to n-type conductivity in as-grown ZnO.

## 2.5 Previous work – Ni configuration in ZnO

There is a profusion of spectroscopic data on the absorption of transition metal ions in semiconductor crystals. Already in 1962, Weakliem [29] studied the absorption spectra of  $\text{Ni}^{2+}$ ,  $\text{Co}^{2+}$  and  $\text{Cu}^{2+}$  in crystals of ZnO, ZnS and CdS. In particular, he observed absorption lines at 4215 and 4248  $\text{cm}^{-1}$  in the spectra for Ni-doped ZnO, both believed to be related to  $\text{Ni}^{2+}$  on Zn sublattice (i.e., effectively  $\text{Ni}_{\text{Zn}}^0$ ). A few years later, Anderson [30] detected absorption lines at 4217 and 4248  $\text{cm}^{-1}$  in Ni-doped ZnO. However, it was not until Kaufmann et al. [31] in 1972 studied absorption lines at 4219, 4244 and 4250  $\text{cm}^{-1}$  that a satisfactory interpretation of these lines was provided. Kaufmann et al. [31] ascribed these latter lines as electronic  ${}^3T_1(F) \rightarrow {}^3T_2(F)$  transitions of  $\text{Ni}^{2+}$  with a dynamic Jahn Teller effect in the  ${}^3T_2(F)$  state of the defect, which allowed the observed fine structure of the  ${}^3T_2(F)$  state to be explained satisfactorily.

Ni-related absorption lines at 4216, 4240 and 4247  $\text{cm}^{-1}$  lines have been observed by Lavrov et al. [32–34] in hydrothermally (HT) grown ZnO, where also an absorption line at 4325  $\text{cm}^{-1}$  was discovered. The 4325  $\text{cm}^{-1}$  line has been observed in the spectra of ZnO doped with Ni, and have been suggested to be associated with Ni.[35] Lavrov et al. [35] have also studied the influence of uniaxial stress on the 4216, 4240 and 4247  $\text{cm}^{-1}$  absorption lines, which have further supported the assignment of these lines to internal transitions of Ni at substitutional Zn sublattice ( $\text{Ni}_{\text{Zn}}$ ).



The Jahn Teller effect (JTE), as already mentioned, is an example of electron-phonon coupling. The first complete explanation of the effect was given in 1936 by Jahn and Teller [36]. In its simplicity: for almost any set of degenerate electronic states associated with a molecular configuration there will exist some symmetry-breaking interaction in which molecular distortion is associated with the removal of the electronic degeneracy.[37] An implication of this occurs when a transition metal ion (i.e., it has a degenerate electronic state) is surrounded by a high-symmetry ionic configuration. In particular, when Ni-ions ( $d^8$ ) are present as substitutional impurities at Zn sublattice in ZnO (i.e., with surroundings approximating to that of a tetrahedral), the d-electron states split, thus giving rise to new possible internal electronic transitions. The energy split between some of the d-levels is in the IR range, and gives rise to absorption lines in the IR spectra that cannot be explained without invoking the JTE.

## Chapter 3

# Experimental techniques and procedure

The main characterization techniques applied in this thesis are secondary ion mass spectrometry, Fourier transform infrared spectroscopy and four-point resistivity probing, with a particular emphasis on the two former. The processing techniques that have been employed are sputtering and electron beam evaporation. A review of these techniques, together with details of the experimental procedure will be given in the following sections.

### 3.1 Secondary Ion Mass Spectrometry

Secondary Ion Mass Spectrometry (SIMS) is a technique where a focused primary ion beam is used to sputter a solid surface while collecting and analyzing the emitted secondary ions. The secondary ion beam is generated by accelerating the charged particles ejected from the surface. These secondary ions are then mass separated in a mass spectrometer before the ion intensity is measured as a function of time or position. Accordingly, it is possible to record a mass spectrum, lateral impurity distributions and impurity depth profiles. In addition, by the use of reference samples one can quantify the concentration of a given impurity as a function of depth in the sample. A diagram of the principles of SIMS is shown in Figure 3.1, illustrating the primary- and secondary ion beam and the spectrometer, together with the three different measurement alternatives. The very high detection sensitivity (in the range of ppm to ppb for most of the elements), high depth resolution and a dynamic range over 5 orders of magnitude make SIMS a prominent technique in the study of impurities in semiconductors.

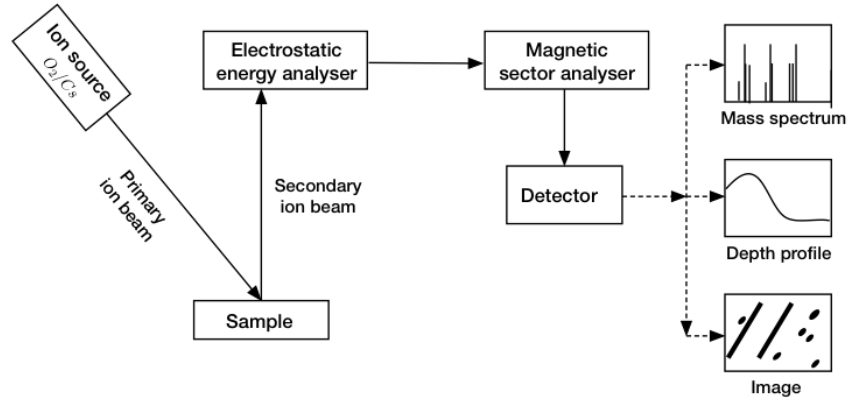


FIGURE 3.1: Principle of SIMS, showing the capability of recording both mass spectra, impurity depth profiles and ion images. Edited from [38].

### 3.1.1 Instrumentation

The microanalyser Cameca IMS-7f that combines both scanning ion microprobing and ion microscope, has been used in this thesis. A sketch of this instrument is shown in Figure 3.2. It is equipped with both a Duoplasmatron (mainly  $O_2$ ) and a cesium primary ion source, an electrostatic sector analyser, a magnetic sector analyser, and three detectors (electron multiplier, Faraday cup, and a fluorescent screen). The primary ion beam is rastered over an area in the range  $100 \times 100 \mu m^2$  and  $500 \times 500 \mu m^2$ , forming a crater in the sample. Ionized particles emitted from the sample can then be accelerated towards the analysers and detectors, forming a secondary ion beam. The base pressure in the sample chamber is of  $< 10^{-9}$  mbar, allowing a sufficient long mean free path for the ions, and a low deposition rate of impurities on the sample surface.

In this work, 10 keV  $O_2^+$  ions have been used as the primary ion beam. For high resistivity samples, the primary ion beam will cause a charge build-up. This excess charge must be removed for proper secondary ion extraction. In the Cameca IMS-7f a built-in electron gun is aimed at the sample for charge compensation.

### 3.1.2 The sputtering process

When an energetic ion impinges on a solid and penetrates, it causes a series of collisions with the target atoms. The directly impacted target atoms are set in motion, which in turn set other target atoms in motion. During this cascade evolution, some of the target atoms in the near surface region may obtain sufficient momentum in the outward direction to overcome the surface barrier height and leave the material.[39] This process is called sputtering. One defines a sputtering yield  $Y$  as the average number of

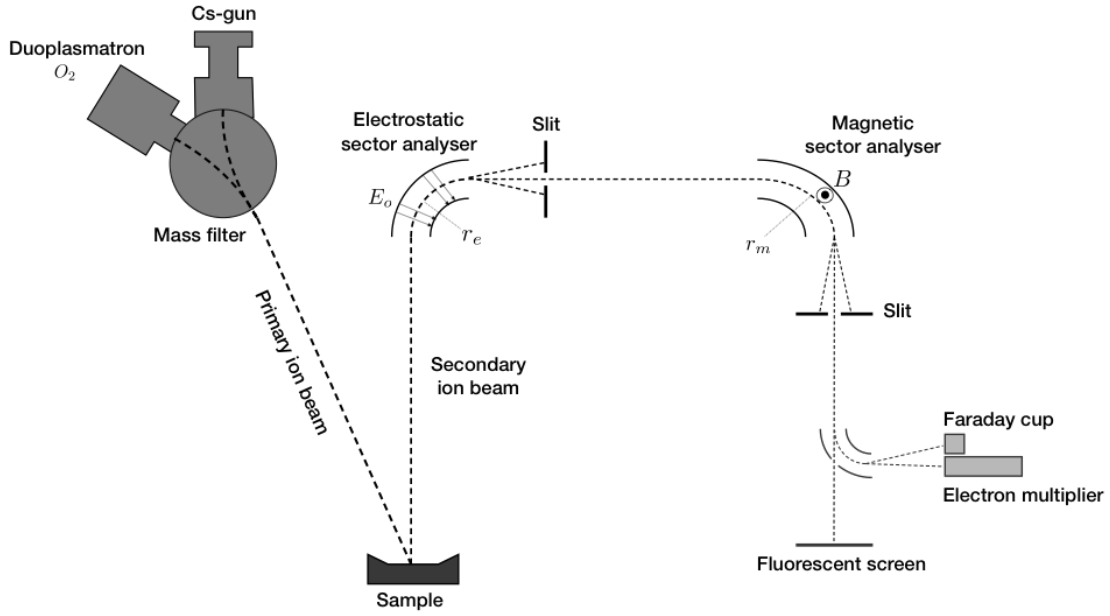


FIGURE 3.2: Simplified schematics of the Cameca IMS-7f SIMS. Primary ions are generated by either the duoplasmatron ( $O_2$ ) or a Cs-gun and focused onto the sample. Secondary ions are mass separated by passing through the electrostatic sector analyser (energy filtering) and then through the magnetic sector analyser (mass filtering). Finally, the secondary ions are monitored by the electron multiplier, Faraday cup, or by the fluorescent screen.

emitted target atoms<sup>1</sup> per primary impinging ion.  $Y$  depends on the mass and energy of the primary ions, the target atoms mass and surface barrier height for escape, in addition to the primary beam angle of incidence. For the energies applied in SIMS (5–15 keV),  $Y$  is typically in the range of 1–10 atoms/ion.[38] This collision cascade model, originally presented in 1969 by Sigmund [40], has led to a rather good understanding of the properties of sputtering. However, only the charged atoms emitted from the target may contribute to form a secondary ion beam. No quantitative theoretical description of the ionization process exists. Nevertheless, an empirical model has been developed where the probability for positive ionization of the target atoms depends exponentially on the ionization energy, while the negative ionization of the target atoms depends exponentially on the electron affinity. Thus, an ionization probability  $\gamma$  is introduced as the fraction of the sputtered atoms that are ionized ( $\sim 1\%$ )[41].

<sup>1</sup>In addition to atoms, molecules may as well be emitted from the targeted, ionized or not. For simplicity only atoms and ions will be narrated in this section.

### 3.1.3 Mass-to-charge analysis

When a secondary ion is formed near the surface of the target material it is accelerated toward the secondary optics by an extraction electrode. The secondary ion will then be analyzed by an electrostatic energy analyser (ESA), composed of two curved metallic plates in parallel (see Fig. 3.2). The inner and outer curved electrodes have voltages of opposite polarity so that the ions will follow the curvature. The centripetal force  $F$  applied to each ion equals the electric field  $E_0$  multiplied by the elementary charge  $q$

$$F = qE_0. \quad (3.1)$$

Furthermore, the magnitude of the centripetal force exerted on an ion with mass  $m$  moving at tangential speed  $v_e$  through the ESA, along a path with curvature radius  $r_e$  is

$$F = \frac{mv_e^2}{r_e}, \quad (3.2)$$

such that

$$qE_0 = \frac{mv_e^2}{r_e}. \quad (3.3)$$

In this way, only the ions with a kinetic energy matching  $r_e$  will be curved to pass through the ESA-exit slit and proceed towards the magnetic sector analyser (MSA). In the MSA the ions will experience a Lorentz force from a magnetic field  $B$  perpendicular to the their path,

$$F = qv_mB, \quad (3.4)$$

where  $v_m$  is the tangential speed of ions through the MSA, and  $F$  is perpendicular to both the trajectory and the magnetic field. By the same argument that led to Eq. 3.3, it follows that Eq. 3.4 equals

$$qv_mB = \frac{mv_m^2}{r_m} \Rightarrow qB = \frac{mv_m}{r_m}. \quad (3.5)$$

Assuming that no energy is lost when the ion travels towards the MSA, the speed of the ion in the ESA will equal the ion speed in the MSA:  $v_e = v_m$ . Combining Eq. 3.3 and Eq. 3.5 then results

$$\frac{m}{q} = \frac{(r_mB)^2}{r_eE_0}. \quad (3.6)$$

Only ions that satisfy this equation will pass through the MSA-exit slit and hit the detector. Hence, by varying the strength of the magnetic field  $B$ , ions already energy-filtered by the ESA is further filtered by momentum to yield a desired mass-to-charge ratio.

Note that the ESA serves two purposes. It narrows the range of ion energies that will proceed through the MSA, thus enabling high mass resolution, which may be further increased by reducing the MSA exit slit. In addition, the ESA also prevents a considerable amount of ionized molecules and other undesirable charged species to reach the detector. Since the sputtered mono-atomic ions tend to dominate the high energy spectrum, while the ionized molecules generally are abundant at low energies, one can arrange the ESA exit slit such that only the higher energy ions are accepted, and thus suppressing the unwanted ionized molecules. However, some ionized molecules do get through and can easily be mistaken for a faster-moving simple ion. Thus, it is crucial to be aware of the possible mass interferences in order to correctly interpret the SIMS spectra.

### 3.1.4 Data analysis

The measured secondary intensity  $I_i$  for a given element  $i$ , depends on the primary ion beam intensity  $I_P$ , an instrument transmission function  $T$ , the sputtering yield  $Y$  and ionization probability  $\gamma_i$  (introduced in Section 3.1.2), in addition to the concentration of element  $C_i$ . The instrument transmission function  $T$  expresses the amount of secondary ions that travel all the way to the detector. The intensity  $I_i$  can be expressed as

$$I_i = I_P Y \gamma_i T C_i. \quad (3.7)$$

However, the ionization probability  $\gamma$  is in general not known, and the atomic concentration can not be quantified directly from Eq. 3.7. It is common to measure a reference sample, implanted with a known dose of  $i$ , in combination with the sample of interest. Provided that the concentration in the reference sample does not deviate much from that in the studied sample, this will give a good measure of the four first proportionality factors on the right hand side of Eq. 3.7. This is commonly referred to as the relative sensitivity factor  $RSF = I_P Y \gamma T$ , and is found as the ratio between the secondary ion beam intensity  $I_i$  and the known concentration of the specific element from the reference sample. Under optimum conditions, SIMS data can be obtained with less than  $\pm 10\%$  error in accuracy.[38] However, since part of the uncertainty lies in the implanted dose of the reference sample, the error in precision may be lower than this.

When measuring depth profiles, the magnetic field is cycled through one or more values in accordance with the mass-to-charge ratio of interest. The secondary ion intensity  $I_i$  is then recorded as a function of time for each element  $i$ , to yield one or more impurity profiles as a function of time. To convert the time to depth, the sputtered crater depth was in this work measured with a Dektak 8 stylus profiler after the SIMS measurement. This procedure will only be valid if the erosion rate is constant throughout the profile.

A constant erosion rate is reasonable to assume for a homogenous material. However, when measuring heterostructures the erosion rate for each layer must be examined and taken into account in the conversion.

## 3.2 Fourier Transform Infrared Spectroscopy

Infrared (IR) absorption spectroscopy is a technique where IR radiation is absorbed by matter. IR-light propagating towards the sample of interest is either reflected, transmitted or absorbed, and the resulting spectrum is then compared to a reference spectrum (e.g., measured in vacuum) to rule out instrument specific absorption. This makes it possible to study the samples ability to absorb light, i.e., absorptivity. A technique that efficiently collects spectral data over a range of frequencies is the Fourier Transform Infrared Spectroscopy (FTIR). This prevalent technique has traditionally been used to study vibrations of molecular bonds in the gas- or liquid phase, but have also been extended to study defects in semitransparent solid state materials. Its functionality is based on interferometry, which will be described in the following.

### 3.2.1 Michelson interferometer

The two-beam interferometer originally designed by Michelson in 1891 [42] is the basic design of many interferometers used for IR absorption spectroscopy today. These two-beam interferometers have subsequently been developed further to achieve certain advantages over the Michelson interferometer. However, the underlying theory of all scanning two-beam interferometers is the same, and to gain an understanding of interferometry it is most enlightening to examine the elementary Michelson interferometer. Schematics of the Michelson interferometer is shown in Figure 3.3. It comprises a beamsplitter and two mutually perpendicular plane mirrors, in which one is movable along an axis perpendicular to its plane. A collimated beam of radiation from an external source is propagated toward the beamsplitter, where it is partially reflected to the fixed mirror ( $\sim 50\%$ ) and partially transmitted to the moving mirror ( $\sim 50\%$ ). Upon return to the beamsplitter the two beams interfere and are partially reflected and partially transmitted towards the detector and the source. The amount which is reflected and transmitted depends upon the beams phase properties before recombination, and thus the optical path difference  $\delta = 2(OM - OF)$  (see Fig. 3.3).

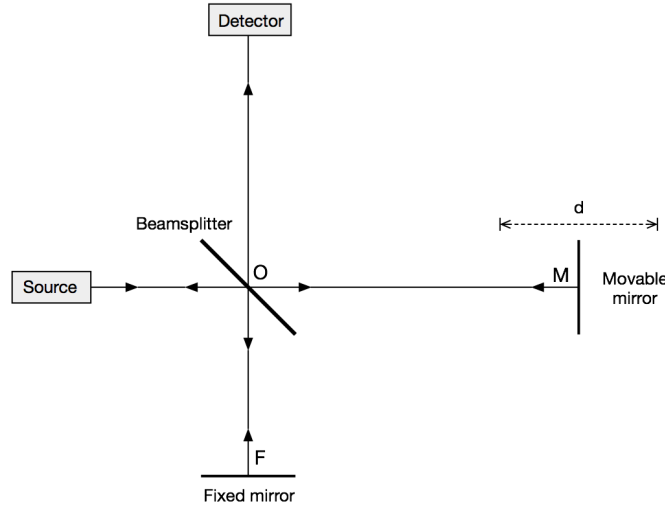


FIGURE 3.3: Michelson interferometer.

### 3.2.2 Formation of the interferogram

Upon recombination of the two beams at the beamsplitter they will experience interference. For simplicity, let's for a moment consider a monochromatic light source. The two beams will then superpose to form a resultant wave of greater or lower amplitude. If the optical path difference  $\delta$  is an integer multiple of the wavelength  $\lambda$ ,

$$\delta = n\lambda, \quad n = 0, 1, 2, \dots \quad (3.8)$$

the beams are said to interfere constructively, and the intensity of the beam passing to the detector is the sum of the two beams before recombination. If, however,  $\delta$  is an odd multiple of  $\lambda/2$ ,

$$\delta = (2n + 1)\frac{\lambda}{2}, \quad (3.9)$$

they will interfere destructively, and no light will pass to the detector.<sup>2</sup> Thus, if the mirror is moved at a constant velocity, the intensity  $I$  measured at the detector will vary sinusoidally with a maxima each time the retardation  $\delta$  is an integer multiple of  $\lambda$ ,

$$I(\delta) = \frac{I(\tilde{\nu})}{2} \left( 1 + \cos \left( \frac{2\pi\delta}{\lambda} \right) \right) \quad (3.10)$$

<sup>2</sup>No photons are of course destroyed upon recombination (apart from some inevitable absorption in the beamsplitter), they simply travel in a different direction, and that direction is back toward the source in a Michelson interferometer. This is easy to see if one realizes that a phase change of  $180^\circ$  occurs at reflection at the mirrors, a  $90^\circ$  phase change when reflected at the beamsplitter, and no change in the phase as the beam is transmitted through the beamsplitter. Consequently, when all the light passes to the source none is passed toward the detector, and vice versa.



or

$$I(\delta) = \frac{I(\tilde{\nu})}{2} (1 + \cos(2\pi\tilde{\nu}\delta)), \quad (3.11)$$

where  $I(\tilde{\nu})$  is the intensity of the source with wavenumber  $\tilde{\nu} = 1/\lambda$ . [15] The constant component  $I(\tilde{\nu})/2$  in Eq. 3.11 does not provide any particular useful information. It is the modulated component  $\frac{1}{2}I(\tilde{\nu}) \cos(2\pi\delta/\lambda)$  that is of interest in spectroscopic measurements, and is referred to as the interferogram  $b$ ,

$$b(\delta) = \frac{I(\tilde{\nu})}{2} \cos(2\pi\tilde{\nu}\delta). \quad (3.12)$$

In practice, additional factors affect the magnitude of  $b(\delta)$ , such as absorption in the mirrors, beamsplitter and sample, represented by  $B(\delta)$ . These factors may be incorporated in Eq. 3.12 by a single wavenumber-dependent correction factor  $G(\tilde{\nu})$  [15], which gives the modified interferogram

$$B(\delta) = \frac{G(\tilde{\nu})I(\tilde{\nu})}{2} \cos(2\pi\tilde{\nu}\delta). \quad (3.13)$$

Moreover,  $G(\tilde{\nu})I(\tilde{\nu})/2$  may be set equal to  $S(\tilde{\nu})$ , the single beam spectral intensity, thus providing a simple equation for representing the interferogram:

$$B(\delta) = S(\tilde{\nu}) \cos(2\pi\tilde{\nu}\delta). \quad (3.14)$$

When the source is a continuum, as is the case for FTIR, the ideal interferogram can be described by a weighted integral of cosine-functions over all wavenumbers,  $\tilde{\nu}$ :

$$B(\delta) = \int_{-\infty}^{\infty} S(\tilde{\nu}) \cos(2\pi\tilde{\nu}\delta) d\tilde{\nu}. \quad (3.15)$$

Eq. 3.15 can be recognized as the cosine Fourier transform of  $S(\tilde{\nu})$  and the spectrum may thus be retrieved by carry out the inverse Fourier transform:

$$S(\tilde{\nu}) = \int_{-\infty}^{\infty} B(\delta) \cos(2\pi\tilde{\nu}\delta) d\delta, \quad (3.16)$$

which may be written as

$$S(\tilde{\nu}) = 2 \int_0^{\infty} B(\delta) \cos(2\pi\tilde{\nu}\delta) d\delta, \quad (3.17)$$

because of the symmetry of the interferogram about the zero point of retardation  $\delta$ . Thus, in theory one could obtain an infinitely high resolution by measuring the complete spectrum from 0 to  $+\infty \text{ cm}^{-1}$ . However, to achieve this one would have to vary the retardation  $\delta$  between 0 and  $+\infty \text{ cm}$ . This entails that one would have to scan the

moving mirror an infinitely long distance, which is of course not possible in a real interferometer. By imposing limits on the mirror displacement,  $d$ , one effectively performs a multiplication of the interferogram by a truncation function,  $T(\delta)$ :

$$S(\tilde{\nu}) = 2 \int_0^\infty T(\delta) B(\delta) \cos(2\pi\tilde{\nu}\delta) d\delta, \quad (3.18)$$

where  $T$  is defined as 1 within the range of  $d$  and 0 otherwise.  $T(\delta)$  is just a simple boxcar truncation function, and its Fourier transform has the shape of the sine cardinal function,  $\sin(x)/x$ . Because of this rather abrupt truncation, the spectrum of a monochromatic source will not be an infinitely narrow line, but a broadened peak with adverse damped sidelobes on each side. These sidelobes complicate the quantification of the spectral intensity, and may even give rise to misinterpretation if incorrectly assigned to one or more absorption lines. To circumvent this and to suppress the sidelobes, more suitable truncation functions may be used instead prior to the Fourier transform. The most obvious advancement would be to apply a simple triangular truncation function, or even better, a gaussian shaped function. This process is called apodization, and several apodization functions have been investigated over the years. In this work a Blackman-Harris 3-term function is used[43]:

$$A(\delta) = \begin{cases} C_1 \cos(\frac{\pi\delta}{d}) + C_2 \cos(\frac{2\pi\delta}{d}) + C_3 \cos(\frac{3\pi\delta}{d}) & \text{if } n \text{ is even} \\ 0 & \text{otherwise} \end{cases} \quad (3.19)$$

where  $d$  is the maximum mirror displacement with the constants  $C_1 = 0.42323$   $C_2 = 0.49755$  and  $C_3 = 0.07922$ . By restricting the maximum mirror displacement using the apodization function  $A(\delta)$  in Eq. 3.19 the spectrum becomes

$$S(\tilde{\nu}) = 2 \int_0^\infty A(\delta) B(\delta) \cos(2\pi\tilde{\nu}\delta) d\delta. \quad (3.20)$$

The resolution,  $\Delta\tilde{\nu}$ , scales approximately as the inverse of the maximum mirror displacement [15]:

$$\Delta\tilde{\nu} \approx \frac{1}{d}, \quad (3.21)$$

such that an increase in  $d$  will give a greater spectral resolution. However, the measurement noise also increases linearly with  $d$ . Therefore, the optimum choice of  $d$  will vary, depending on the instrument and the measured sample. Moreover, the signal-to-noise ratio (SNR) of the spectrum is proportional to the resolution [44]:

$$\text{SNR} \propto \Delta\tilde{\nu}. \quad (3.22)$$

Instrumental configuration			
	Parameter	Specification	Spectral range (cm <sup>-1</sup> )
Performance	Resolution	0.5 cm <sup>-1</sup>	
	Scanner velocity	0.16 - 2.5 cm/s	
Optics	IR-sources	MIR Globar	100 - 6000
		NIR Tungsten	2000 - 25 000
	Beam splitters	KBr	200 - 13 000
		CaF <sub>2</sub>	1000 - 25 000
	Detectors	MCT	650 - 11 000
		InSb	1800 - 11 000

TABLE 3.1: Instrumental configuration of the Bruker IFS 125 HR FTIR instrument. Values are obtained from the instrument manual.

As a compromise between the resolution and SNR, a spectral resolution of  $\Delta\tilde{\nu} = 0.5 \text{ cm}^{-1}$  have been used in this work.

### 3.2.3 Instrumentation

The setup used in this work is a Bruker IFS 125 HR Fourier transform spectrometer equipped with MCT (HgCdTe) and InSb liquid nitrogen-cooled semiconductor detectors. In addition to have the ability to switch between a MIR globar (SiC) and a NIR (Tungsten bulb) light source, two different beamsplitters, KBr and CaF<sub>2</sub>, were accessible. Table 3.1 gives the performance and optical configuration of the spectrometer. The CTI-Cryogenics 8200 compressor cold finger cryostat was used to cool the sample down to  $\sim 20 \text{ K}$  in vacuum, and the temperature was recorded with a LakeShore 331 temperature controller. Figure 3.4 gives an overview of the beam path through the spectrometer.

### 3.2.4 Data analysis

When measuring solid materials, light can be reflected from both its front and back surface, which may cause multiple internal reflections that interfere with the directly transmitted light. This will be observed as a sinusoidal noise over the whole spectrum. To correct for this undesirable effects, it is customary to manipulate the interferogram prior to the Fourier transform. The sinusoidal interference fringes appear as peaks in the interferogram, and may be replaced by a stright line without significant spectral side effects.

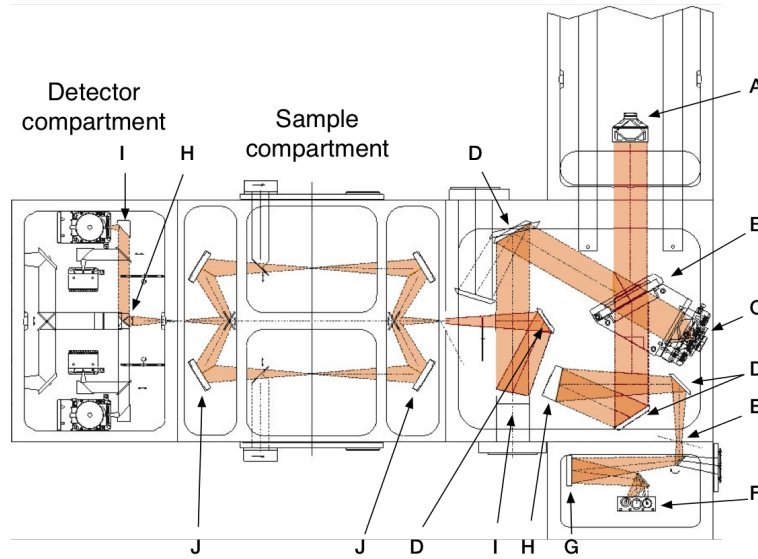


FIGURE 3.4: Optical path of the IR-beam in the Bruker IFS 125 HR, obtained and edited from the instrument manual. A) Movable retroreflecting mirror, B) Beam splitter, C) Fixed retroreflecting mirror, D) Folding mirror, E) Input aperture, F) Sources, G) Spherical mirror, H) Collimating parabolic mirror, I) Focusing parabolic mirror, J) Toroidal mirror.

For each sample measurement, a background measurement were performed by allowing the IR-light to propagate through an empty sample holder, having the same transmittance area as the sample. This enableed the calculation of the transmittance in Eq. 2.27, and thus a measure of the absorbance (Eq. 2.29). As a result of reflection from the sample surfaces and broad absorption features in the sample (e.g., free carrier absorption), the resulting absorbance spectrum is normally shifted over the zero absorbance level. A baseline correction is therefore performed by fitting a polynomial to the data, to facilitate the interpretation of the data.

### 3.3 Four-point probe

The four-point probe system is a sensitive technique for performing resistivity measurements. This device contains four thin co-linear Tungsten wire probes, which are brought in contact with the sample to be measured, as shown schematically in Figure 3.5. A current  $I$  is generated to flow between the outer probes, and a voltage  $V$  is measured across the two inner ones, ideally without drawing any current. The key advantage of four-terminal sensing is that the separation of the voltage and the current electrodes almost eliminates the contact resistances and the impedance contribution of the wiring. In this work the Jandel RM3-AR have been used for resistivity measurements.

If the sample is of semi-infinite volume and if the distance  $s$  between the probes are equal, then it can be shown that the resistivity of the semi infinite volume is given by [45]

$$\rho = 2\pi s \frac{V}{I}. \quad (3.23)$$

Practical samples, of course, are of finite size and a geometrical correction factor  $G$ , that is dependent on the thickness and the probe spacing, must be included:

$$\rho = 2\pi G s \frac{V}{I}. \quad (3.24)$$

Correction factors for six different boundary conditions have been derived by Valdes [46].

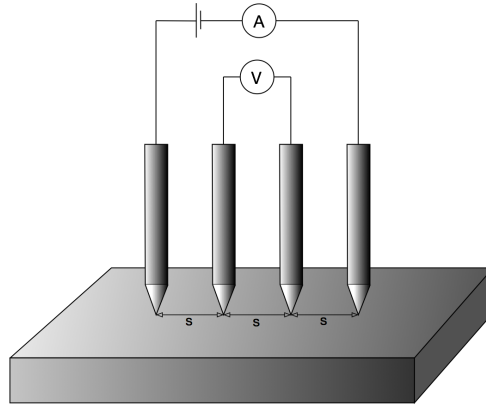


FIGURE 3.5: Schematic of the resistivity measurements setup.

In cases when measurements were difficult to obtain due to rough surfaces and thus insufficient contact between the probes and sample, the probe tips were dipped in eutectic InGa to improve the contact. Furthermore, for each measurement the voltage was measured for several applied currents. The resistivity was then calculated from the average of these values, to achieve higher statistical accuracy. Moreover, if the carrier mobility  $\mu$  of the sample is known, the carrier density  $n$  can be calculated from

$$n = \frac{1}{\rho q \mu}, \quad (3.25)$$

where  $q = 1.602 \cdot 10^{-19}$  C is the elementary electric charge. [6, 47]

### 3.4 Magnetron Sputtering

As already encountered in section 3.1.2, sputtering is a process whereby particles are emitted from a solid target material due to bombardment of the target by energetic ions. In addition to utilization in microsectioning techniques, sputtering is also widely applied for thin-film deposition.

An inert gas (Ar) is let into the pre-evacuated chamber ( $\sim 10^{-6}$  mbar) to yield a working pressure of  $\sim 0.1$  mbar. A plasma is initiated by applying a voltage across the target and the substrate. Once a plasma is formed, positively charged ions in the plasma are accelerated toward the cathode (target material). When they strike the surface, target atoms will be ejected from the surface with energies of typically 10 to 50 eV, and may travel across the chamber to be deposited on the sample surface (substrate). Secondary electrons are also released when the ions impinge the target. They will instantly be accelerated away from the cathode, and may collide with neutral inert gas atoms while crossing from cathode to anode. If the energy transfer is large enough the impacted atom will be ionized and accelerated toward the target. Given a high enough voltage, it is thus a self-sustaining process. However, only a small fraction of the inert gas is ionized ( $\sim 0.001\%$  [10]) in this arrangement, which implies a rather low sputter rate. It is possible to increase the sputter rate by applying a magnetic field across the target (magnetron sputtering). This will cause the released secondary electrons to follow a helical path towards the anode, thus increasing their pathlength and probability of collision with neutral atoms. If the magnetic field is large enough, the electrons may be trapped by the magnetic field and return to the target, where the cycle will repeat.

The Semicore Tri-Axis balanced field magnetron sputtering system has been used in this work to deposit Ni-doped ZnO films on ZnO-bulk substrate. The targets used were a 99.99% pure ZnO-target and a 99.99% Ni-target. The distance between the targets and substrate was kept at  $\sim 11$  cm.

### 3.5 Electron Beam Evaporation

Evaporation is a convenient and common method for thin-film deposition. The principle of the deposition is that a hot source material evaporates and condenses onto a substrate. The evaporation takes place in high vacuum ( $\sim 10^{-6}$  mbar), resulting in a long mean free path for the evaporated particles. This enables the evaporated material to travel directly to the substrate, without significant scattering from the ambience.

The source material may be heated in different ways. The simplest type of system is to resistively heat the source (e.g., by a wolfram filament). This will of course limit the ability to evaporate refractory metals. To overcome this one may instead place the source in a crucible, typically made of boron nitride and inductively heat the crucible. This allows the source to be heated to sufficient temperatures. The drawback for both of these systems is contamination from either the filament or crucible, which have direct impact on the thin-film quality. This effect can be avoided by heating only the source by an electron beam (e-beam) while cooling the crucible. In this work the Leybold E-beam evaporation L 560 K have been used, where an an electron gun situated under the crucible ejects an intense, high energy beam. The location of the filament minimizes contamination of filament material in the deposited film. The e-beam is bent through  $270^\circ$  by a strong magnetic field causing it to be incident on the surface of the source (Figure 3.6).

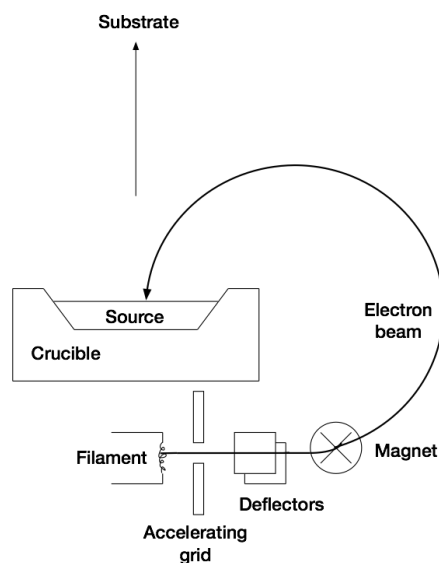


FIGURE 3.6: Electron beam evaporative source. A typical source arc in which the beam can be rastered across the surface of the source material. Edited from [10].

### 3.6 Experimental procedure

The samples used in this work is presented and a survey of the different treatment and characterization steps is outlined. Three different approaches employed for introducing Ni into the ZnO samples are then presented, with emphasis on strengths and drawbacks.

Current	32.0 A
Out Power	16.898 W
Frequency	50000 Hz
Speed	400 mm/s
Line Width	0.080 mm
Pulse Width	1.0 $\mu$ s

TABLE 3.2: Parameter settings applied for the cut and separation of the samples, using the PowerLine E-25 SHG laser cutter.

### 3.6.1 Samples and methodology

As-received ZnO wafers commercially available from Tokyo Denpa have been amended and studied in this work. The wafers were grown by the hydrothermal (HT) method and cut perpendicular to the c-axis to a size of  $10 \times 10 \times 0.5$  mm<sup>3</sup> and  $20 \times 20 \times 0.5$  mm<sup>3</sup>. Two as-recieved ZnO wafers with given resistivities  $\rho = 0.22$   $\Omega$ cm and  $\rho = 2618$   $\Omega$ cm were labeled 'A' and 'AA', respectively. The wafers were cut and separated by the use of a Rofin PowerLine E-25 SHG laser cutter, with parameter settings as shown in Table 3.2. Wafer A ( $10 \times 10 \times 0.5$  mm<sup>3</sup>) was separated into a total of 6 samples. Wafer AA was first cut into 4 sub-wafers to yield sizes of  $10 \times 10 \times 0.5$  mm<sup>3</sup>. 3 of these sub-wafers were then labeled B, C, and D and separated by the same method into a total of 18 samples. The cut were made on Zn-face (15 scans) for the separation, and a signature label (1-6) was engraved in the corner of each of the total 24 samples (1 scan), as seen in Figure 3.7. The labeling of each sample on Zn-face served as a way to differentiate between the two crystal directions and among the samples themselves. Figure 3.8 shows the sequential sample treatments and characterization steps conducted in this work.

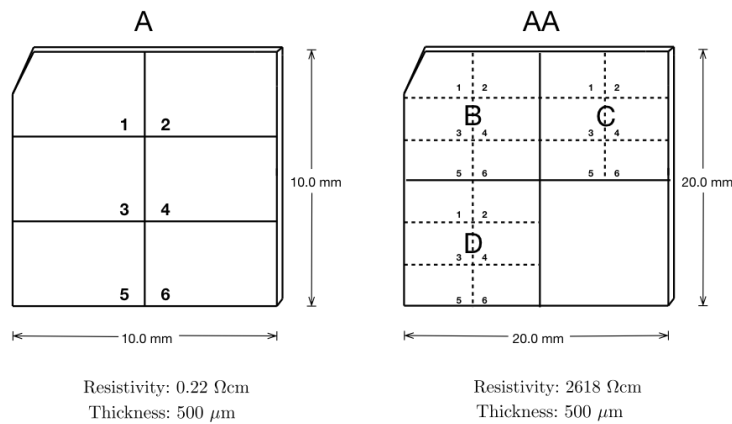


FIGURE 3.7: Hydrothermal grown ZnO wafers A and AA were cut to yield sample sizes of  $\sim 5.0 \times 3.3 \times 0.5$  mm<sup>3</sup> by the use of a laser. A signature (1-6) was engraved on the Zn-face of each sample with the purpose to distinguish between the samples in addition to be able to differentiate between Zn-face and O-face.



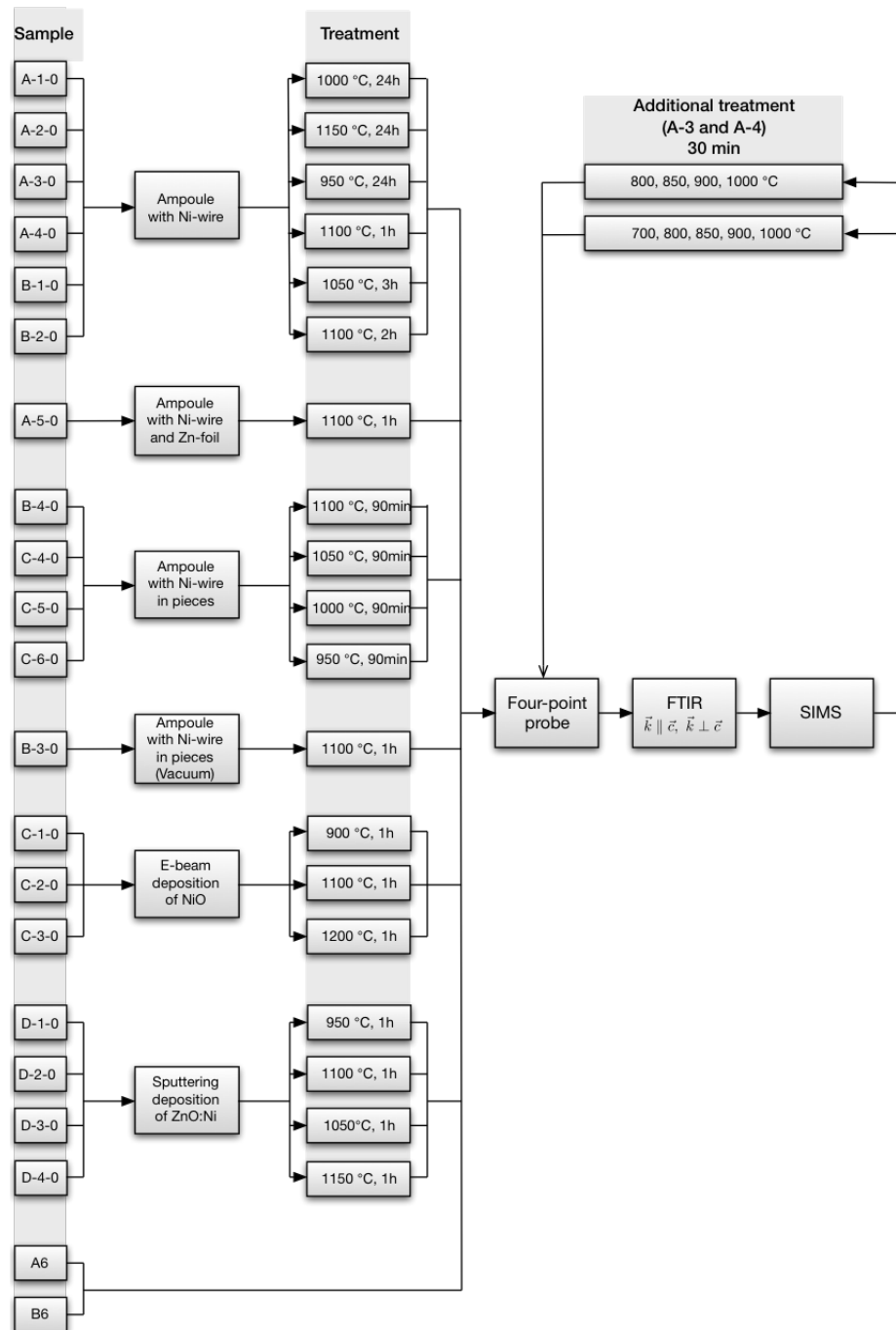


FIGURE 3.8: Overview of the samples workflow.

### 3.6.2 Introduction of Ni from gas phase

To introduce Ni into ZnO from gas phase, samples were sealed in quartz-ampoules together with a Ni-wire of purity 99.995% (Figure 3.9), followed by a heat treatment. The advantage of introducing Ni in this manner is that subsequent transmission measurements (e.g., FTIR) is not influenced by any external source, which would be the case for a predeposited film. The sealing was done at ambient pressure, except for sample B-3-0 where the ampoule was sealed while bridged to a rough vacuum pump to yield a pressure of  $\sim 0.5 \text{ atm}$ <sup>3</sup>. Another change in the default setup was made for sample A-5-0, in which a Zn-foil of purity 99.9% was included together with the Ni-wire. Altogether, 8 samples were treated with a Ni-wire. Furthermore, based on observed lateral non-uniformity of Ni-diffusion in these samples, 5 additional samples were prepared with a modification of the treatment configuration. The alteration was to cut the Ni-wire into pieces in order to have the Ni-source more uniformly distributed around the ZnO crystal.

It must be noted here that processing failure occurred during heat treatment of the sample A-3-0 (24 hour at 950°C), resulting in an additional temperature ramping. However, the total time of the heat treatment at 950°C still apply to 24 hours and the temperature did not exceed 950°C.

The pressure  $P$  inside an ampoule of volume  $V$  during heat treatment can be found by the ideal gas law [48]

$$PV = Nk_B T, \quad (3.26)$$

where  $N$  is the number of particles in the gas,  $k_B$  is the Boltzmann constant and  $T$  the absolute temperature. The volume can be taken as constant throughout the heat treatment, and the number of particles in the gas can be assumed to be the same just after desired temperature is reached. The pressure  $p_2$  during heat treatment at temperature  $T_2$  then relates to the pressure  $p_1$  at room-temperature  $T_1$ <sup>4</sup> as

$$\frac{N}{V} = \frac{p_2}{k_B T_2} = \frac{p_1}{k_B T_1}. \quad (3.27)$$

Solving for  $p_2$  and inserting  $p_1 = 1 \text{ atm}$ ,  $T_1 = 292 \text{ K}$  and the respective  $T_2$ , the pressure during heat treatment can be found. Table 3.3 gathers all the samples treated in ampoule, together with the amount of Ni-wire, treatment time and temperature, and the pressure inside the ampoules under heat treatment assuming the model described above.

<sup>3</sup>No pressure gauge was available during this processing, but a pressure of 0.5 atm was estimated.

<sup>4</sup>It is assumed that the temperature inside the ampoules during the sealing was 20°C. However, due to the heat from the gas burner during closing of the ampoules the real temperature may be higher, thus causing an overestimation of the pressure inside the ampoule at room-temperature.

	Sample	$m_{Ni}$ (g)	Time (h)	$T_2$ ( $^{\circ}C$ )	$p_2$ (atm)
Whole wire	A-1-0	0.11	24	1000	3.4
	A-2-0	0.10	24	1050	3.6
	A-3-0	0.07	24	950	3.3
	A-4-0	0.07	1	1100	3.8
	A-5-0 <sup>†</sup>	0.08	1	1100	3.8
	B-1-0	0.12	3	1050	3.6
	B-2-0	0.14	2	1100	3.8
	B-5-0	0.14	1.5	1100	3.8
Cut wire	B-3-0*	0.11	1	1100	1.9
	B-4-0	0.10	1.5	1100	3.8
	C-4-0	0.08	1.5	1050	3.6
	C-5-0	0.09	1.5	1000	3.4
	C-6-0	0.09	1.5	950	3.3

TABLE 3.3: Experimental configuration with the amount of Ni and annealing time for doping in ampoule, together with annealing temperature  $T_2$  and the corresponding estimated pressure  $p_2$ . For sample A-5-0 (<sup>†</sup>) an additional Zn-foil of  $m = 0.26$  g was included. Lastly, the room-temperature pressure for sample B-3-0 (\*) was 0.5 atm. For all the other an initial pressure of 1 atm were used for the calculation of  $p_2$ .



FIGURE 3.9: Method of Ni-introduction from gas phase. A closed quartz-ampoule containing a Ni-wire and the ZnO crystal is heat treated at desired temperature and time.

### 3.6.3 Introduction of Ni from predeposited NiO-film

In an attempt to improve the uniformity of Ni-diffusion in the ZnO crystals, a film of Nickel Oxide (NiO) were deposited onto the as-grown samples C-1-0, C-2-0 and C-3-0. The three samples were deposited simultaneously by E-beam evaporation to yield a film thickness of 290 nm, as measured by a combination of SIMS and stylus profilometry. After deposition the samples were annealed in ambient conditions for 1 hour at 900 $^{\circ}C$ , 1100 $^{\circ}C$  and 1200 $^{\circ}C$ , and labeled C-1-1, C-2-1 and C-3-1, respectively.

The reason for depositing a film of NiO, rather than a pure Ni-film was to ensure an O-rich stoichiometry near the boundary with the bulk crystal during heat treatment. This might not have been possible with a Ni-film, since oxygen could have migrated from the ZnO bulk towards the boundary where it might have formed NiO. This scenario

would have resulted in a Zn-rich condition near the boundary, and altered the diffusion conditions in an uncontrolled manner.

The deposition was done using the Leybold E-beam evaporation L560K, where a crucible containing 99.99(5)%<sup>5</sup> pure Ni was used as source. To form NiO an oxygen leak was maintained during deposition. After a series of development steps carried out on test-samples (glass), the optimal working pressure for the formation of NiO was found to be  $6 \cdot 10^{-4}$  mbar. The characterization of the test-samples were done with X-ray diffraction measurements and the procedure of the process development is outlined in some detail in Appendix B.1.

### 3.6.4 Introduction of Ni from predeposited ZnO:Ni-film

It was observed that the doping by NiO-film revealed a highly undefined boundary between the film and bulk material after heat treatment, as will be presented in Section 4.3. Such a non-distinct interface is undesirable when pursuing an understanding of the diffusive behaviour of a dopant, since clear boundary conditions need to be applied in modeling of the system. Motivated by this, further efforts were made in an attempt to maintain a clear transition between the film and bulk after heat treatments at high temperatures. A film of Ni-doped ZnO were deposited onto the samples D-1-0, D-2-0, D-3-0 and D-4-0 by co-sputtering a target of 99.99% pure ZnO and a 99.99% pure Ni-target. The sample chamber was evacuated to a base pressure of  $1.3 \cdot 10^{-6}$  mbar before an argon pressure of 0.13 mbar was established. The four samples were deposited simultaneously at 400°C for 240 min, with a speed of rotation of the samples of 12 rpm. The distance between the target and samples was 11 cm. A constant power of 50 W for the ZnO-target and 40 W for the Ni-target were maintained throughout the deposition. The resulting thickness of the films were found to be 750 nm, as obtained by a combination of SIMS and stylus profilometry. This gives a deposition rate of 3.1 nm/min for the particular conditions.

The relatively high power density used for the Ni-target is a consequence of the ferromagnetic property of Ni. Because of the magnetic behaviour of Ni a proportion of the magnetic field that is applied accross the Ni-target in a magnetron system will not penetrate entirely through the target. This will cause the sputter rate to be less than what one would expect from a magnetron sputtering system. In order to determine the Ni-target power density needed to achieve a desired ZnO-film with a Ni concentration on the order of  $10^{21} \text{ cm}^{-3}$ , a series of development steps were conducted and analysed

---

<sup>5</sup>The purity of the Ni source is not necessarily fully correct, due to the fact that the crucible have been refilled with Ni several times by different operators over the years who may have used different degrees of purity.

by Hall Effect measurements and Scanning Electron Microscopy (SEM). These measurements showed that a Ni-target power of 40 W resulted in a ZnO-film with approximately 3 at.% Ni or a Ni concentration of  $1.3 \cdot 10^{21} \text{ cm}^{-3}$ , as measured by SEM. The process development is outlined in some detail in Appendix B.2

## Chapter 4

# Results and discussion

The results of the experimental procedure outlined in Section 3.6 are presented and discussed, given first with regard to the SIMS results and, secondly, the results from the FTIR measurements (Sections 4.5 and 4.6).

### 4.1 Ni impurities in as-grown ZnO samples

Figure 4.1 show the Ni concentration as a function of depth for the two as-grown samples (A6 and B6) that originate from the two different wafers studied in this work. The Ni concentration is observed to be  $< 10^{16} \text{ cm}^{-3}$  from a depth of  $0.5 \text{ }\mu\text{m}$  to  $3 \text{ }\mu\text{m}$  into the bulk for both the samples. However, the near surface concentration shows about one order of magnitude higher Ni concentration. As the samples are of  $500 \text{ }\mu\text{m}$  in thickness, this will have only a small effect on the total Ni concentration, and one can infer that the HT-grown ZnO samples studied in this work do not contain any substantial amount of residual Ni-impurities.

### 4.2 Diffusion profiles – introduced from Ni gas phase

#### 4.2.1 Doping by Ni-wire

Figure 4.2 shows the Ni concentration vs depth profiles of the samples A-3-1, A-1-1 and A-2-1, that were deliberately doped in a closed-quartz amoule containing Ni-wire for 24 hours at  $950^\circ\text{C}$ ,  $1000^\circ\text{C}$  and  $1050^\circ\text{C}$ , respectively. The measurements were performed by SIMS on both the faces. As can be seen, the Ni-depth profiles increase in concentration and depth as a function of temperature. For the sample doped at  $1050^\circ\text{C}$ , the surface

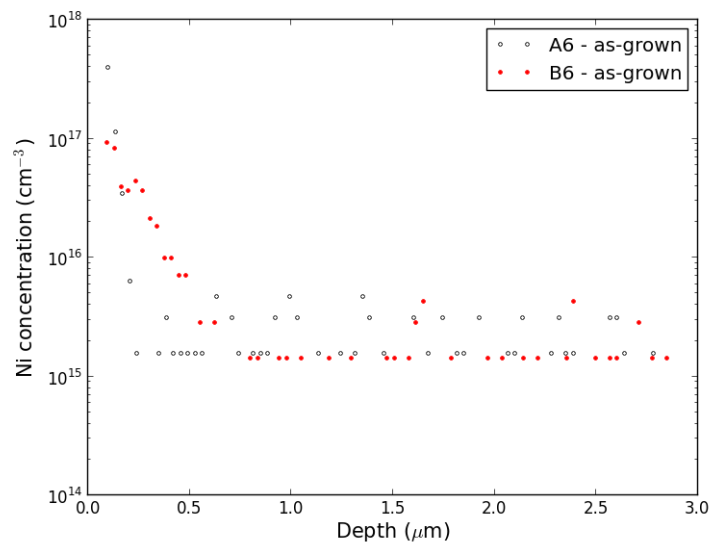


FIGURE 4.1: Ni concentration vs depth profiles of the as-grown samples A6 and B6 that originates from the two different wafers studied in this thesis.

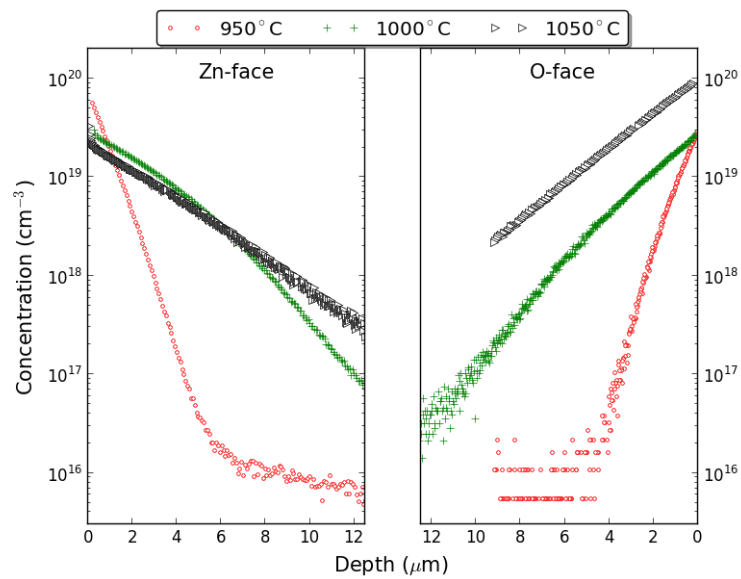


FIGURE 4.2: Comparison of the Ni concentration profiles of three samples after deliberate doping in a closed quartz-ampule containing Ni-wire at 950°C, 1000°C and 1050°C for 24h, as measured by SIMS on both faces.

concentration measured on O-face is almost one order of magnitude higher than that measured on the Zn-face. The opposite is observed for the sample treated at 950°C, with a surface concentration close to a factor of three higher at the Zn-face as compared to the O-face. The sample doped at 1000°C shows similar surface concentration when measured on both faces. Furthermore, the diffusion depth of the sample doped at 950°C is about 4  $\mu\text{m}$  when measured on O-face, while on Zn-face it extends to approximately 6  $\mu\text{m}$ . The depth measurements performed with stylus profilometry revealed a particular rough surface at the O-face for all the samples. This made accurate measurements of the crater depths difficult to achieve, and may explain the observed difference in diffusion depth between the two faces. The estimated dose of the profiles are summarized in Table 4.1, and elucidate the irregular amount of introduced Ni between the two faces. For the samples doped at 950°C and 1000°C the dose is found to be higher when measured on Zn-face, while the opposite is observed for the sample doped at 1050°C.

Figure 4.3 shows the concentration vs depth profiles of the samples A-4-1 and B-2-1 deliberately doped by Ni at 1100°C for 1 and 2 hours, respectively. The profiles were obtained on Zn-face and show a significant change in both the surface concentration and diffusion depth between the two samples; almost one order of magnitude difference in the surface concentration is observed. There is also a considerable difference in the diffusion depth, where the Ni-concentration exceeds the background concentration to a depth of about 14  $\mu\text{m}$  in the 2h treated sample. Furthermore, the two isothermal profiles depict an almost identical amount of Ni (see Table 4.1), indicating a limited source, and that the limited source model outlined in Section 2.2.1 (Eq. 2.9) could be applicable for the 2h profile. However, the profile does not resemble a characteristic Gaussian shape, and no reasonable fit using the limited source model was found.

Further, Ni-concentration vs depth measurements revealed a large variation in both the surface concentration and profile-shape, when measured at different locations on the sample surface. Figure 4.4 shows three different Ni concentration vs depth profiles (left) for sample A-3-1 (24h, 950°C), as measured at the Zn-face. The corresponding position of the measured areas are shown in the picture to the right, as obtained by optical microscopy. Crater 1 in the figure corresponds to the measurement done on the part of the sample that was closest to the Ni-wire during doping, consistent with the high surface concentration and dose observed for this profile. The apparent lateral non-uniformity of the Ni diffusion obtained for the samples doped by this method makes it challenging to gather and compare reliable diffusion profiles.

Figure 4.5 shows the Ni-concentration vs depth profile for the sample A-2-1, doped at 1050°C for 24h, together with the sample B-1-1 doped at same temperature for 3h. The surface concentration is found to be a factor of 5 lower for the sample doped for 24h.



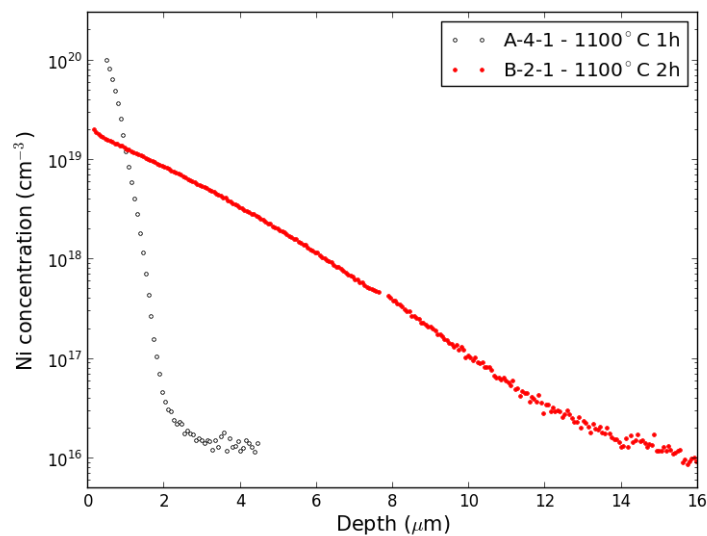


FIGURE 4.3: Ni concentration vs. depth profiles of sample A-4-0 and B-2-0, deliberately doped in a closed-quartz ampoule containing Ni-wire at 1100°C for 1 h and 2 h, respectively. The measurements were performed on Zn-face.

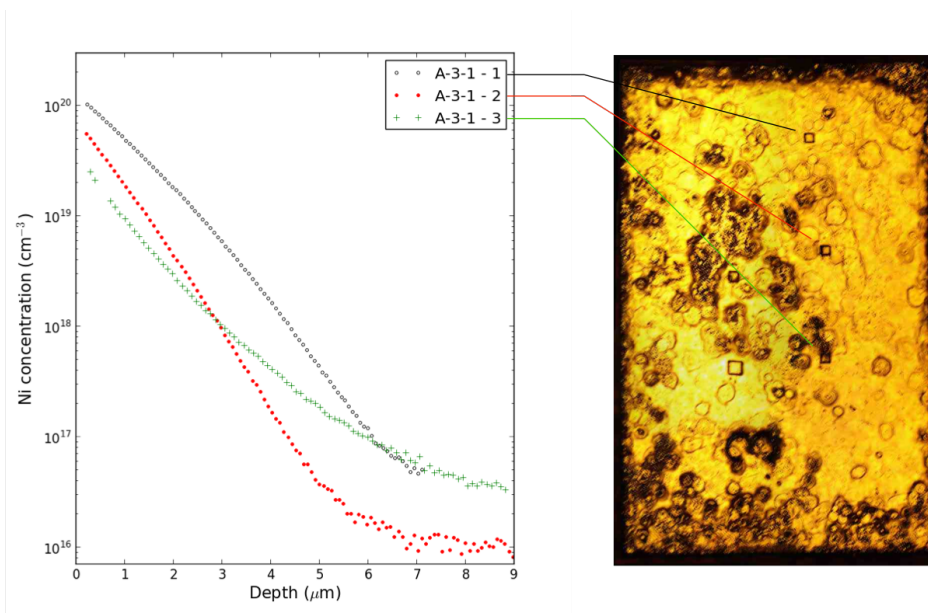


FIGURE 4.4: Lateral non-uniformity: Ni-concentration vs depth profiles (left) of the sample A-3-1 deliberately doped in a closed quartz-ampoule containing Ni-wire at 950°C for 24h, with the corresponding analysed area at the Zn-face of the sample (right). The Ni-wire was located closest to crater 1 (top of the picture) during the doping.

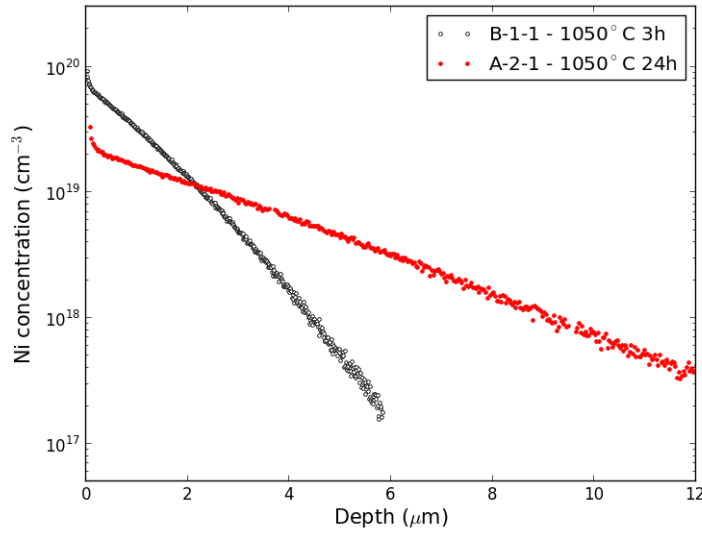


FIGURE 4.5: Ni concentration vs. depth profiles of the samples B-1-1 and A-2-1 deliberately doped in a closed quartz-ampoule containing Ni-wire at 1050°C for 3 and 24 hours, respectively. The measurements were performed on Zn-face.

In addition, the respective doses only differ by  $\sim 20\%$  (see Table 4.1), suggesting that the source is limited for treatment longer than 3 hours. However, as pointed out above, care must be taken when evaluating these results due to the lateral variation occurring during the introduction of Ni in the samples.

To further investigate the possible effect of the ZnO stoichiometry on the diffusion mechanisms of Ni in ZnO, one sample was doped by including a Zn-foil together with the Ni-wire inside the ampoule. Figure 4.6 shows the Ni concentration vs depth of the sample A-5-1 intentionally doped in a closed quartz-ampoule containing Zn-foil and Ni-wire at 1100°C for 1h. Ni is observed to migrate deep into the bulk, with a relatively high concentration,  $\sim 2 \cdot 10^{17} \text{ cm}^{-3}$ , at a depth of 8  $\mu\text{m}$ . The surface concentration of Ni is about 2 orders of magnitude lower compared to the sample doped without Zn-foil (sample A-4-1 in Fig. 4.3). Moreover, the dose is only  $2.31 \cdot 10^{14} \text{ cm}^{-2}$ , which is more than one order of magnitude lower than that observed for the sample doped without Zn-foil.

#### 4.2.2 Doping with a Ni-wire cut into pieces

To improve the lateral uniformity experienced with doping from Ni-wire, additional in-diffusion experiments were conducted using a Ni-wire cut into pieces and distributed around the ZnO samples. The weight of the Ni-wires were about 0.1 g (see Section 3.6.2, Table 3.3) and amounted to 10 pieces after splitting.

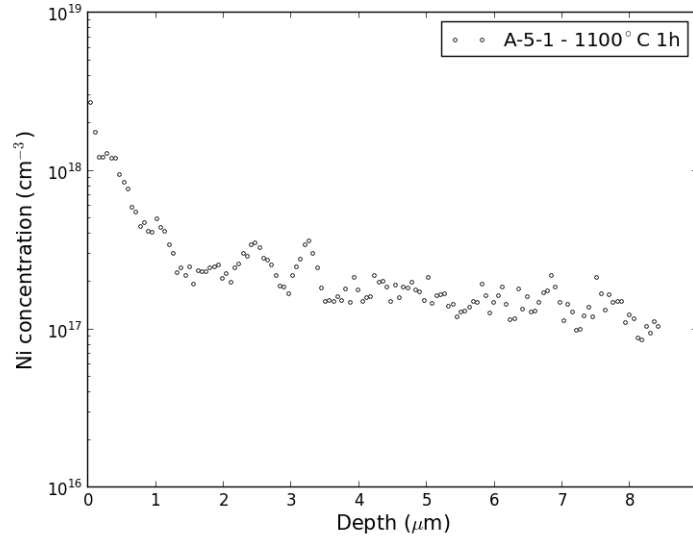


FIGURE 4.6: Ni concentration vs. depth profile of the sample A-5-1 deliberately doped in a closed-quartz ampoule containing Ni-wire and Zn-foil at 1100°C for 1 hour.

Sample	Treatment	Ni-dose (cm <sup>-2</sup> )	
		Zn-face	O-face
A-3-1	950°C 24h	5.01·10 <sup>15</sup>	2.12·10 <sup>15</sup>
A-1-1	1000°C 24h	7.03·10 <sup>15</sup>	5.63·10 <sup>15</sup>
A-2-1	1050°C 24h	6.75·10 <sup>15</sup>	2.04·10 <sup>16</sup>
B-1-1	1050°C 3h	8.47·10 <sup>15</sup>	-
A-4-1	1100°C 1h	4.45·10 <sup>15</sup>	6.73·10 <sup>15</sup>
B-2-1	1100°C 2h	4.34·10 <sup>15</sup>	-
A-5-1	1100°C 1h	2.31·10 <sup>14</sup>	-

TABLE 4.1: Total dose of the measured Ni-diffusion profiles obtained from the samples that were doped in a closed quartz-ampoule containing Ni-wire. '-' denotes that no measurement were conducted in the respective crystal direction.

Figure 4.7 shows the concentration of Ni as a function of depth for the samples deliberately doped for 90 min in a closed-quartz ampoule containing small pieces of the Ni-wire, distributed around the sample. The treatment temperature were 950°C, 1000°C, 1050°C and 1100°C for the samples C-6-1, C-5-1, C-4-1 and B-4-1, respectively, and the measurements were carried out at the Zn-face. As can be seen, the Ni-profiles increase in depth as a function of temperature. The small variation in the surface concentration as a function of temperature indicates that Ni is not limited by the solubility in ZnO, but is rather restricted by the source of Ni.

The integrated dose for each of the profiles in Figure 4.7 can be found in Table 4.2. A pronounced increase in the integrated dose is observed between the samples doped

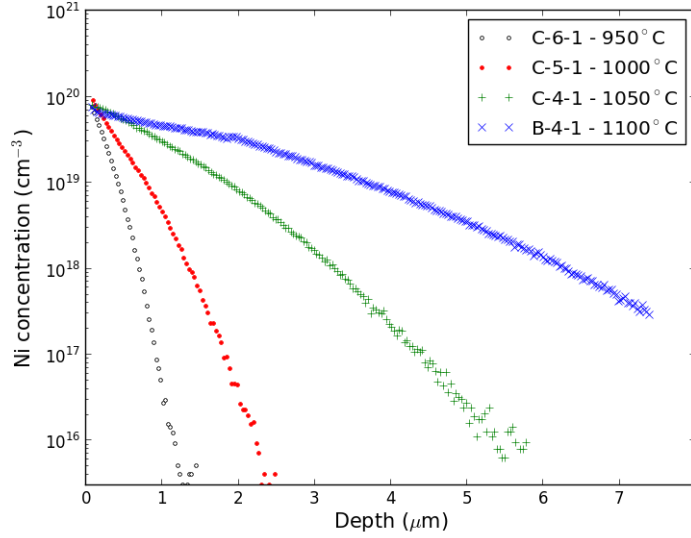


FIGURE 4.7: Ni concentration vs. depth profiles of the samples C-6-1, C-5-1, C-4-1 and B-4-1, deliberately doped in a closed-quartz ampoule containing Ni-wire in pieces at 950°C, 1000°C, 1050°C and 1100°C for 90 min, respectively. Measured by SIMS at the Zn-face.

at 1000°C, 1050°C and 1100°C, exemplified with an increase from  $1.64 \cdot 10^{15} \text{ cm}^{-2}$  to  $3.40 \cdot 10^{16} \text{ cm}^{-2}$  comparing the lowest and highest doping-temperatures.

In Figure 4.8 the semi-infinite source model (introduced in Section 2.2.1, see Eq. 2.7) has been applied to fit<sup>1</sup> the different diffusion profiles discussed above (Fig. 4.7). It is possible to deduce an activation energy for the migration of Ni from the modeled diffusion profiles in Figure 4.8. Using the Arrhenius relation (Eq.2.19) derived in Section 2.2.2, the activation energy  $E_a$  can be found from the slope of a linear fit to the diffusivities, as shown in Figure 4.9. Using this approach, an activation energy of  $E_a = 4.3 \text{ eV}$  for the Ni diffusion is obtained. Moreover, the intersection with the ordinate provides a value for the pre-exponential factor  $D_0$ , and is found to be  $6 \cdot 10^4 \text{ cm}^2\text{s}^{-1}$ . Both the activation energy and the pre-exponential factor are high. From a theoretical approach, Nickel [49] has estimated a pre-exponential factor of  $D_0^T \approx 0.7 - 5 \cdot 10^{-3} \text{ cm}^2\text{s}^{-1}$  for diffusion of hydrogen in crystalline ZnO. The assumption made by Nickel in this evaluation was a zero entropy for formation and migration of the defect, resulting in a simplified expression for the  $D_0$  given in Eq. 2.19. Although the value applies to hydrogen in ZnO, it provides a first approximation to which order of magnitude is expected for the pre-exponential factor

<sup>1</sup>The fit was made by the Levenburg-Marquardt gradient method to minimise the squared residuals between the model (erfc) and the measured profiles. This is an iterative non-linear least squares method and is provided by the leastsq-optimize package in Python. The implementation of the code can be found in Appendix C.

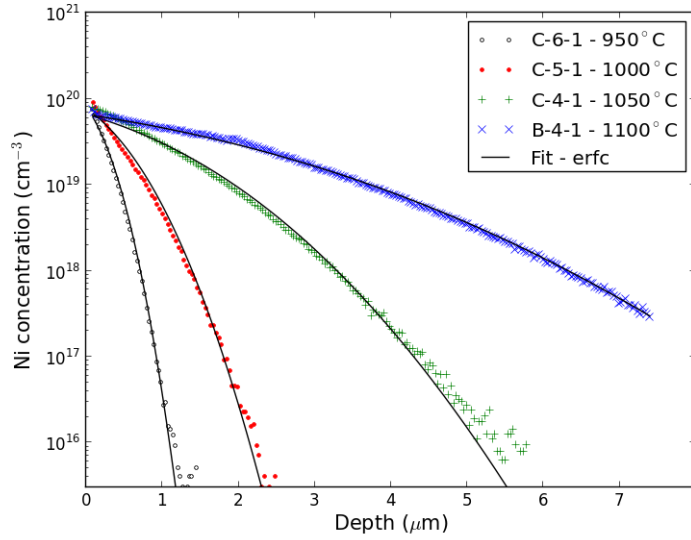


FIGURE 4.8: Ni concentration vs. depth profiles of the samples C-6-1, C-5-1, C-4-1 and B-4-1, deliberately doped in a closed-quartz ampoule containing Ni-wire in pieces at 950°C, 1000°C, 1050°C and 1100°C for 90 min, respectively. The semi-infinite source model has been applied for the fit of each profile.

for interstitial-type diffusion in ZnO. This indicates that the applied model does not reveal the full picture of the involved diffusion processes.

Supplementary measurements for the samples C-6-1, C-5-1 and C-4-1 showed a good lateral uniformity of the diffusion as a function of measurement position on the sample surface. However, for the sample B-4-1 (1100°C), some degree of variation was observed. The results for sample B-4-1 and C-5-1 are shown in Figure 4.10, where three SIMS measurements were performed equidistant from the sample side edge for both samples.

Figure 4.11 shows the concentration vs depth of the sample B-3-1 deliberately doped in a quartz-ampoule, closed in rough vacuum, containing Ni-wire in pieces at 1100°C for 1h. As can be seen, a significant migration of Ni occurs deep into the substrate. The diffusion shows similarities to that observed for the Zn-foil experiment (Fig.4.6), however, the average concentration is about one order of magnitude higher for the sample treated in rough vacuum, both indicating a high Ni-diffusivity. During the treatment, the sample changed from a thickness of 550  $\mu\text{m}$  to 430  $\mu\text{m}$ . One possible explanation for the decrease in thickness is an out-diffusion of oxygen in the reducing condition during the in-diffusion, which would lead to Zn-rich conditions.

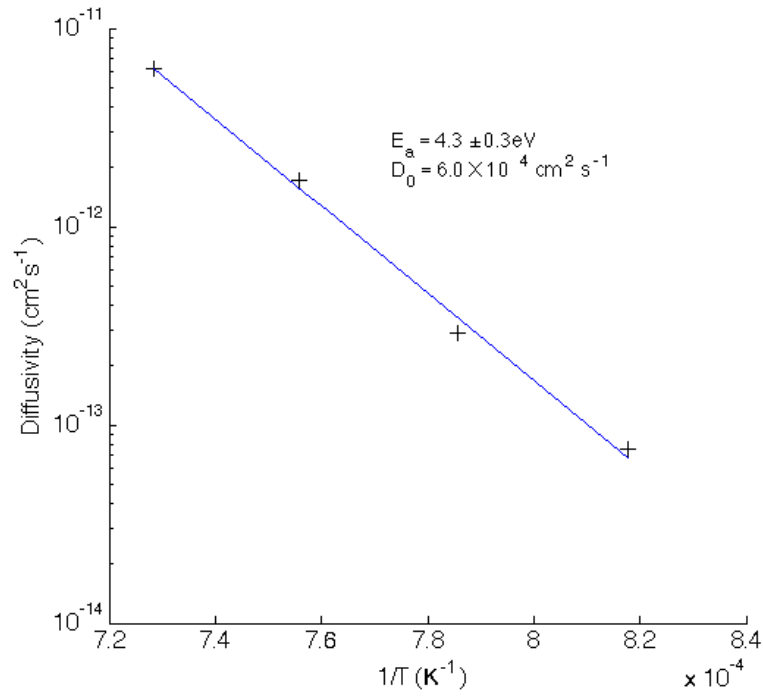


FIGURE 4.9: Ni diffusivity vs reciprocal absolute temperature for the samples C-6-1, C-5-1, C-4-1 and B-4-1, deliberately doped in a closed-quartz ampoule containing Ni-wire in pieces at 950°C, 1000°C, 1050°C and 1100°C for 90 min, as obtained from fit by the semi-infinite source model. The given uncertainty in the activation energy reflects the quality of the fit.

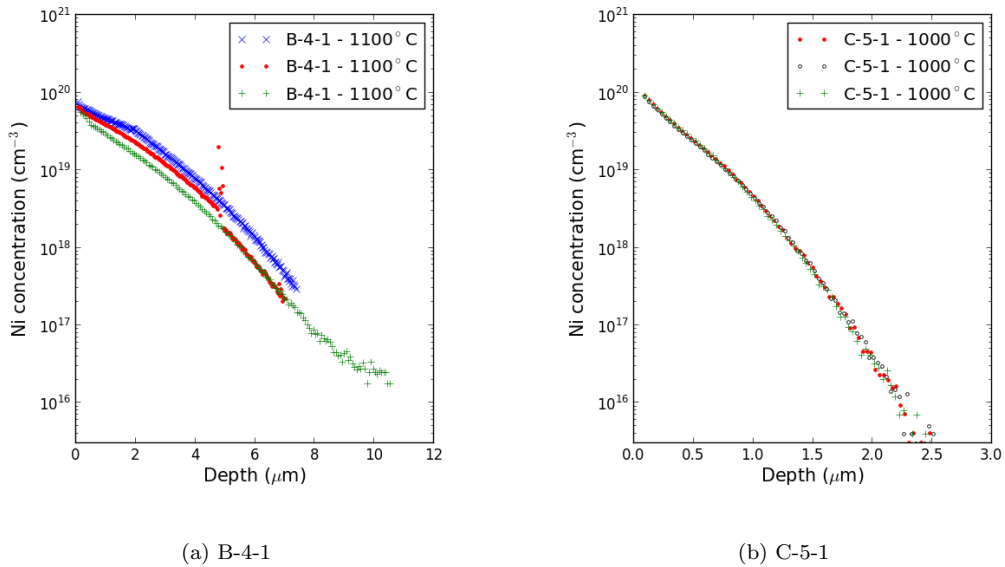


FIGURE 4.10: Lateral uniformity: Ni-concentration vs depth profiles of the samples B-4-1 and C-5-1. Three measurements were conducted on each sample and show the lateral non-uniformity at high temperature (a).

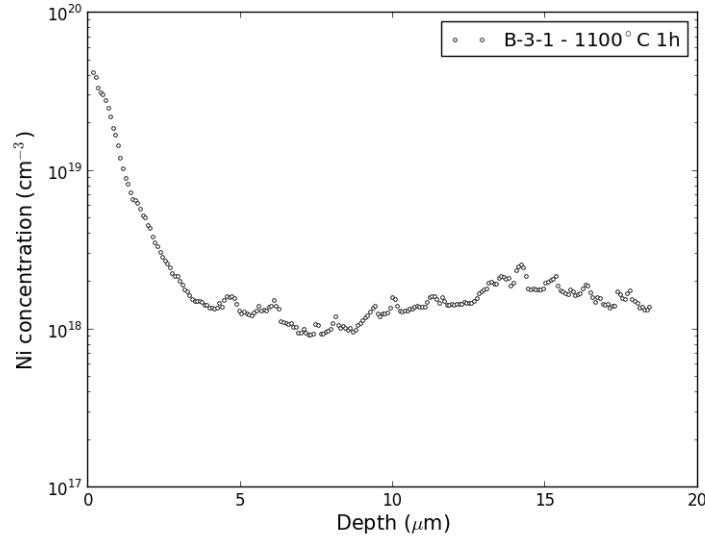


FIGURE 4.11: Ni concentration vs. depth profile of the sample B-3-1 deliberately doped in a low vacuum closed quartz-ampoule containing Ni-wire in pieces at 1100°C for 1 hour.

Sample	Treatment	Ni-dose (cm <sup>-2</sup> )	
		Zn-face	O-face
C-6-1	950°C 90 min	1.64·10 <sup>15</sup>	-
C-5-1	1000°C 90 min	3.02·10 <sup>15</sup>	-
C-4-1	1050°C 90 min	7.18·10 <sup>15</sup>	-
B-4-1	1100°C 90 min	1.32·10 <sup>16</sup>	-
B-3-1	1100°C 60 min	5.52·10 <sup>15</sup>	-

TABLE 4.2: Integrated dose of the measured Ni-diffusion profiles obtained from the samples that were doped in a closed quartz-ampoule containing Ni-wire in pieces. '-' denotes that no measurements were conducted in the respective crystal direction.

### 4.2.3 Comprehending the diffusive behavior

The similar values for the integrated doses observed between the different isothermal diffusion profiles in both Figure 4.3 and Figure 4.5, indicate that the Ni-wire behave as a limited source. The limitation may come from the fact that the Ni-wire may oxidise during the heat treatment. Indeed, upon visual inspection subsequent to the doping, all the wires were observed to have a green-yellow colour gradient that was more evident for the samples doped for long times and/or high temperature. The Ni oxide (NiO) has a substantially higher melting temperature as compared to the metallic state ( $\sim 1980^\circ\text{C}$  vs  $\sim 1450^\circ\text{C}$ ), thus effectively limiting the Ni-source.

The oxidation of the Ni-wire during the doping also has a secondary effect of reducing

the partial pressure of oxygen inside the ampoule. In turn this will affect the intrinsic properties of ZnO. From theoretical considerations by Janotti and Van de Walle [24] it is shown that at low partial oxygen pressure, the formation energy of oxygen vacancies in ZnO is low. As a consequence, the ZnO material will move toward a Zn-rich condition as a function of time during the treatment. In a similar manner as observed for Li in ZnO [50, 51], it is speculated that Ni at substitutional Zn sublattice ( $\text{Ni}_{\text{Zn}}$ ) will transform into interstitial Ni ( $\text{Ni}_{\text{i}}$ ) through a kick-out mechanism when the material becomes Zn-rich, by the following mechanism:



A diffusion of Ni by an interstitial mechanism is expected to have a higher diffusivity than Ni migrating by a vacancy mediated mechanism. If such a transition occurs, it would therefore lead to an enhanced diffusion of Ni, compared to diffusion under O-rich conditions. Similar to what is observed for Li diffusion in ZnO [52].

This hypothesis is supported by the experiments performed with Zn-foil (see Fig. 4.6) and under reduced initial pressure (see Fig. 4.11). In these circumstances a Zn-rich condition is expected, and in both cases an enhanced migration of Ni is observed. It is therefore suggested that the diffusion of Ni in the closed quartz-ampoule experiments, occurs by a two-step-process: a vacancy mediated and an interstitial mechanism, where the former dominates during the O-rich conditions while the latter prevails during Zn-rich conditions. Further, the conditions change during the in-diffusion treatment and are highly dependent on both time and temperature, and potentially also on the amount of Ni-metall vs ZnO within the ampoule.

Such a process may explain the high values of the activation energy  $E_a$  and pre-exponential  $D_0$  estimated in Section 4.2.2. It was observed a comparatively high Ni-diffusivity for the two samples treated at highest temperature, where it is conceivable that the oxidation rate of the Ni-wire is fastest. This implies a faster change towards a Zn-rich condition, and thus a shift for the equilibrium in Eq. 4.1 towards the  $\text{Ni}_{\text{i}}$  situation, resulting in an enhanced diffusion.

### 4.3 Diffusion profiles – introduced from NiO-film

To introduce Ni under O-rich conditions, in-diffusion of Ni was performed from a pre-deposited NiO film.

Figure 4.12 shows the Ni concentration vs depth profiles for the samples deposited by NiO-film and heat treated at 1100°C and 1200°C at ambient conditions for 1 hour. The



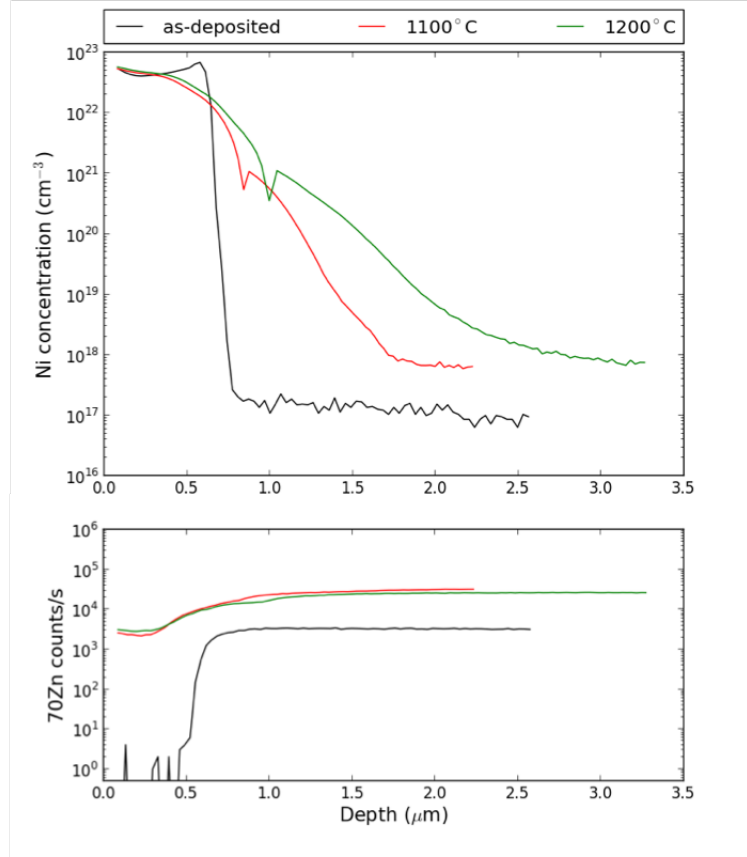


FIGURE 4.12: Top: Ni concentration as a function of depth of the samples deposited by NiO: the as-deposited sample C-1-1, and the samples heat treated at 1100°C (C-2-2) and 1200°C (C-3-2) for 1h at ambient conditions. The abrupt dips in the Ni-signal observed for the heat treated samples are caused by a shift from the Faraday Cup to the electron multiplier when detecting the secondary ions in the SIMS microanalyser.

Bottom: the corresponding signal of 70Zn vs depth profiles.

corresponding Zn-signal is shown in the lower part of the figure. The observed abrupt change in concentration at  $\sim 10^{21} \text{ cm}^{-3}$  in the Ni-diffusion profiles are caused by a shift from the Faraday cup to the electron multiplier as the detector during the SIMS-measurement. As can be seen, the Ni concentration vs depth profiles for the heat treated samples show similar shape, which increase in concentration and depth as a function of temperature. Furthermore, it appears that the NiO-film, to a large extent, is drained for Ni during the heat treatment. However, as can be seen in the lower part of the figure, a considerable amount of Zn has migrated from the ZnO-bulk and into the film. This could potentially alter the sputtering yield and/or ionization probability, which may be responsible for the apparent depletion of Ni near the interface.

The dissimilar erosion rate between the film and bulk material has not been taken into account for the Ni-profiles in Figure 4.12. Hence, the apparent depth of the interface observed in the figure ( $\sim 0.6 \mu\text{m}$ ) deviates from the actual measured value of  $0.29 \mu\text{m}$ .

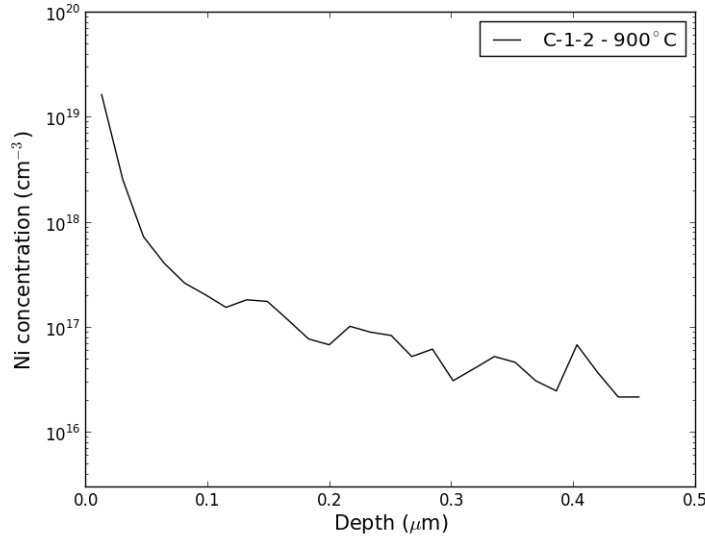


FIGURE 4.13: Ni concentration vs depth of the sample C-1-2, deliberately doped from a predeposited NiO-film at 900°C for 1h at ambient condotions. The zero point depth is the bulk surface, as the film detached after the heat treatment.

Nevertheless, the figure clearly demonstrates that the migration of Zn into the film results in a highly undefined interface. This makes it difficult to study the diffusive behaviour of Ni in these samples, and no further efforts were made to obtain a more correct concentration measure in the film.

Figure 4.13 shows the Ni concentration as a function of depth for the sample deposited by NiO-film and heat treated at 900°C for 1 hour at ambient conditions. At this low temperature, the film deteriorated and detached from the bulk crystal during the treatment. Therefore, the zero-point depth corresponds to the surface of the bulk material. As can be seen, no sufficient Ni-migration occurs at this low temperature.

#### 4.4 Diffusion profiles – introduced from ZnO:Ni-film

In order to preserve the interface between a pre-deposited film and the ZnO bulk material, new Ni in-diffusion experiments were performed from a pre-deposited Ni-doped ZnO film.

Figure 4.14 shows the Ni concentration as a function of depth for the samples that were pre-deposited by a Ni-doped ZnO film and heat treated at 950°C, 1050°C, 1100°C and 1150°C for 1 hour at ambient conditions. The corresponding Na signal vs depth profiles is shown in the bottom part of the figure. The Faraday cup is, at least partially, responsible for the apparently high Ni concentrations observed in the films for all

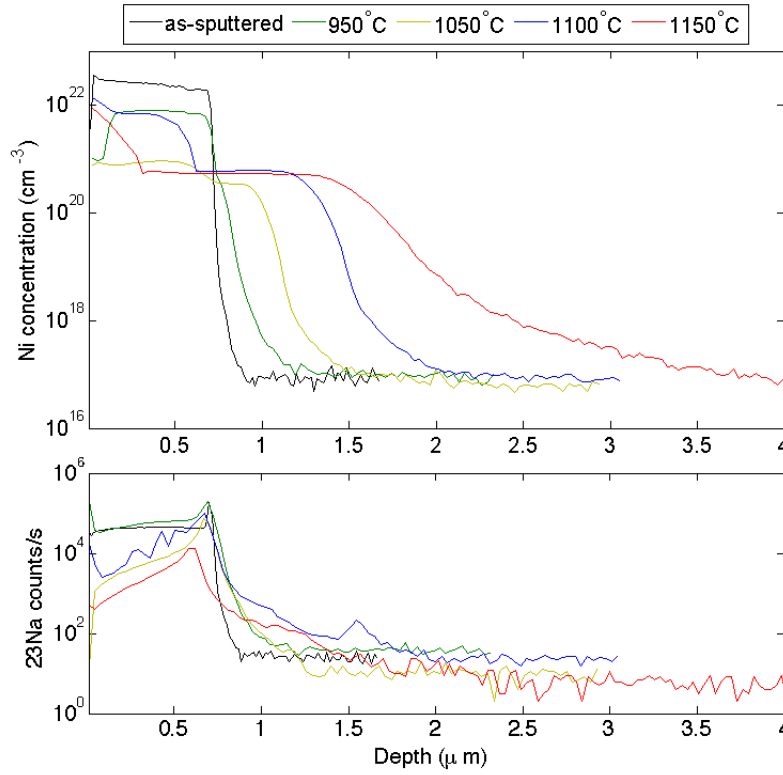


FIGURE 4.14: Top: Ni concentration vs depth profiles of the as-sputtered sample D-4-1, together with the sputtered samples D-1-2, D-3-2, D-2-2 and D-4-2 that were heat treated at 950°C, 1050°C, 1100°C and 1150°C for 1h at ambient conditions. Bottom: measured signal of  $^{23}\text{Na}$  vs depth profiles for the same samples. At concentrations  $> 1 \cdot 10^{21} \text{cm}^{-3}$  the Faraday cup was the operative detector.

the samples, except for the 1050°C one where the electron multiplier did not saturate. To be able to quantify these results also in the source region, new measurements are needed, nevertheless, the present data give some insight into the ongoing processes for Ni-diffusion under O-rich conditions. As can be seen, the film is gradually drained for Ni at temperatures above 950°C. Moreover, heat treatment temperatures in excess of 950°C are necessary to observe significant migration of Ni into the bulk material. At these temperatures, the Ni concentration as a function of depth resembles a box-profile, which increases in concentration and depth as a function of temperature. However, at 1100 and 1150 °C the concentration of the Ni-diffusion shoulder remains unchanged at  $\sim 5.5 \cdot 10^{20} \text{cm}^{-3}$ . It is interesting to note how the slope of the 1150°C profile deviates from the other profiles. The weaker gradient that is observed signifies that a different and faster diffusion mechanism (possibly interstitial diffusion) is involved at this high temperature.

As can be seen in the bottom part of Figure 4.14, the peak in the measured Na-signal agrees well with the interface between the film and bulk for the as-sputtered sample, and

Sample	Treatment	Ni-dose ( $\text{cm}^{-2}$ )
D-1-2	950°C 1h	$8.43 \cdot 10^{15}$
D-3-2	1050°C 1h min	$1.12 \cdot 10^{16}$
D-2-2	1100°C 1h min	$3.53 \cdot 10^{16}$
D-4-2	1150°C 1h min	$4.80 \cdot 10^{16}$

TABLE 4.3: Total dose (in bulk) of the measured Ni-diffusion profiles obtained from the samples that were doped from deposited ZnO:Ni-film. The interface for sample D-4-2 is adjusted for in the calculation of the dose.

is thus regarded as an indicator of the location of the interface. At high temperatures the Na peak is shifted toward the film surface, most likely due to a deterioration of the film. In that case, the film-thickness of the sample treated at 1150°C is observed to be reduced by 100 nm. This is not accounted for in the Ni-diffusion profiles in the figure, but must be taken into account if one is to model the data.

The 1 hour Ni-diffusion profiles in the above figure indicate a slower diffusivity than what was observed for the samples doped for 90 min in a closed quartz-ampoule containing Ni-wire in pieces (Fig. 4.7). The sample doped in ampoule for 90 min at 1050 °C holds a characteristic diffusion length ( $\lambda = 2\sqrt{Dt}$ ) of about 1.6  $\mu\text{m}$ . A similar 1h tretment would have resulted in a characteristic diffusion length of  $\lambda = \sqrt{2/3} \cdot 1.6 \mu\text{m} = 1.3 \mu\text{m}$ , assuming that the semi-infinite source model is applicable also at 1h. If one in a similar manner, as a rough estimate, assume that the 1050 °C profile in the above figure can be considered by the same definition of  $\lambda$ , a characteristic diffusion length of about 0.3  $\mu\text{m}$  is deduced. Even though this is a simplistic estimate, it indicates that a faster diffusion process occurs for the samples doped in a closed quartz-ampoule than when using a Ni-doped ZnO film at ambient conditions; consistent with a model where we have a combination of two contributing diffusion mechanisms.

The Ni concentration vs depth measurements performed on the sample treated at 1050°C show a Ni concentration of  $9.1 \cdot 10^{20} \text{cm}^{-3}$  in the film ( $\sim 400 \mu\text{m}$  from the film surface). Assuming that this concentration is representative also for the other samples, the Faraday cup can be regarded as responsible for much of the deviation in this region. Moreover, this corresponds rather well with the obtained Ni-concentration of  $1.3 \cdot 10^{21} \text{cm}^{-3}$ , as measured by the EDS detector in SEM on as-sputtered test samples (see Process development, Appendix B.2).

Measurement		Absorption peaks (cm <sup>-2</sup> )				
Sample	Orientation	3336	3483	3503	3516	3577
A6	$\vec{k} \parallel \vec{c}$	0.44	-	0.09	-	-
B6	$\vec{k} \parallel \vec{c}$	1.75	-	-	s	-
A6	$\vec{k} \perp \vec{c}$	0.22	0.25	s	-	0.30
B6	$\vec{k} \perp \vec{c}$	0.88	0.67	-	0.28	1.34

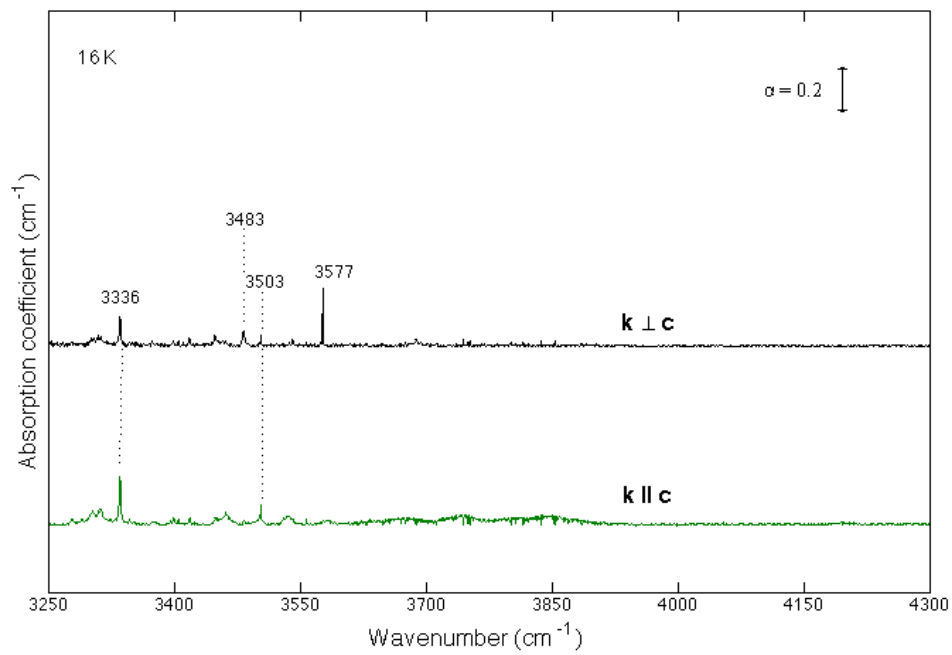
TABLE 4.4: IR peak intensities of the main observed peaks in the as-grown samples, as given by their integrated absorption coefficients. '-' denotes no observable peak, while 's' designates a small peak.

## 4.5 IR absorption spectra measured on as-grown samples

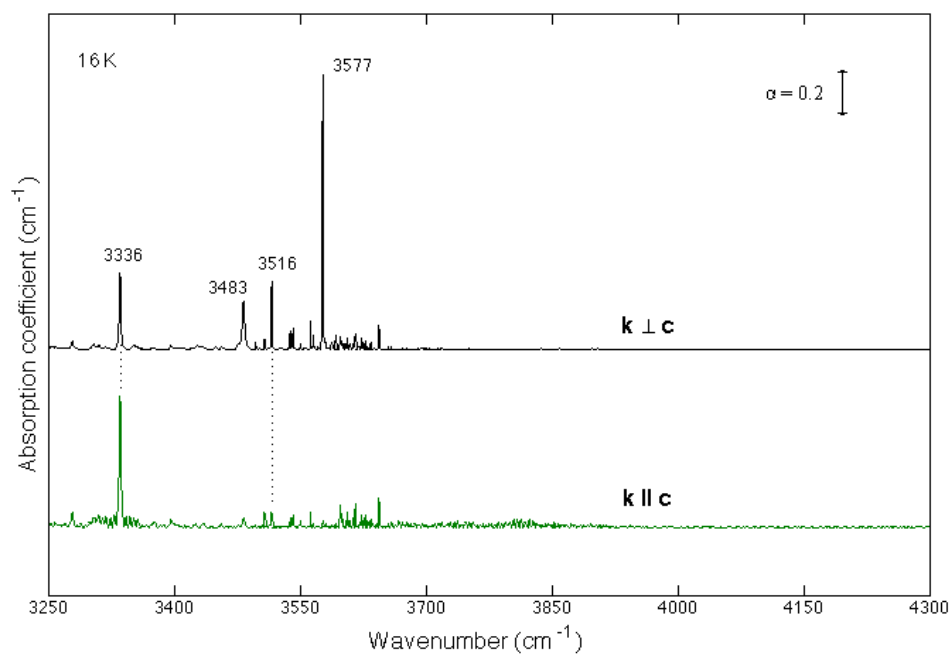
Figure 4.15 shows the IR spectra of the as-grown samples A6 (top figure (a)) and B6 (bottom figure (b)), as measured in both the  $\vec{k} \perp \vec{c}$  and  $\vec{k} \parallel \vec{c}$  orientations. The absorption lines observed in the range from 3300 to 3600 cm<sup>-1</sup> are characteristic of OH stretch modes. In both directions, all the shared absorption lines are more pronounced for the high resistive sample B6 than for the low resistive sample A6. The dominating lines are found at 3336 and 3577 cm<sup>-1</sup> and other weaker lines are observed at 3483, 3503 and 3516 cm<sup>-1</sup>. Several other weak lines occur in the spectra for sample B6, but will not be further discussed in this text. The intensity, or the integrated absorption coefficient, of the main absorption lines are given in Table 4.4.

The 3577 cm<sup>-1</sup> line has previously been identified as a localized vibrational mode (LVM) and assigned to a defect complex involving a single O-H bond (oriented along the c-axis of the crystal) perturbed by an adjacent Li<sub>Zn</sub>. [53, 54] The line is almost always found to dominate the spectra of undoped hydrothermal (HT) grown ZnO, and has been shown to be stable up to annealing at 1200°C for 30 min [32]. However, Johansen et al. [55] have shown that the complex starts to dissociate at lower temperatures, and that its apparent stability is highly dependent on the cooling process. Furthermore, the absorption lines at 3336 and 3483 cm<sup>-1</sup> are located in the region characteristic of O-H stretch vibrational modes and have previously been observed by Lavrov et.al [32] in HT-grown ZnO.

Previously, absorption lines at 4216, 4240 and 4247 cm<sup>-1</sup> have been observed in the IR-absorption spectra for HT-grown ZnO [32, 33], and has been identified as internal electronic transitions of substitutional Ni<sub>Zn</sub><sup>0</sup> [30, 31, 56] (see Section 2.5 for details). As can be seen in Figure 4.15, these lines are not present in the HT-grown ZnO wafers studied in this work. Together with the SIMS concentration measurement conducted on the as-grown samples (Fig. 4.1), this again supports that the samples studied in this work do not contain any substantial amount of residual Ni impurities. For a detailed



(a) As-grown sample A6



(b) As-grown sample B6

FIGURE 4.15: IR absorption spectra of the as-grown samples: a) A6 and b) B6, as measured in the  $\vec{k} \perp \vec{c}$  (top spectra) and  $\vec{k} \parallel \vec{c}$  (bottom spectra) orientations. The samples A6 and B6 originate from the two wafers A and AA, respectively.

Measurement			I (cm <sup>-2</sup> )		Ratio
Sample	Treatment	Orientation	4216	4247	I <sub>4247</sub> /I <sub>4216</sub>
B6	As-grown	$\vec{k} \parallel \vec{c}$	-	-	-
C-6-1	Ni 950°C 90 min	$\vec{k} \parallel \vec{c}$	0.13	0.83	6.4
C-5-1	Ni 1000°C 90 min	$\vec{k} \parallel \vec{c}$	0.17	1.15	6.8
C-4-1	Ni 1050°C 90 min	$\vec{k} \parallel \vec{c}$	0.45	2.96	6.6
B-4-1	Ni 1100°C 90 min	$\vec{k} \parallel \vec{c}$	1.91	12.40	6.5

TABLE 4.5: IR peak intensities of the Ni related absorption peaks given by their integrated absorption coefficients, together with their ratio. '-' denotes no observable peak.

overview of all the IR absorption measurements and intensities of the various peaks discerned in this work, see Appendix A.

## 4.6 IR absorption spectra after Ni-introduction

### 4.6.1 Ni related absorption lines

Figure 4.16 shows IR absorption spectra for the as-grown sample B6 together with the samples C-6-1, C-5-1, C-4-1 and B-4-1 deliberately doped with Ni from gas phase for 90 min at temperatures 950°C, 1000°C, 1050°C and 1100°C, respectively. The measurements were done in the  $\vec{k} \parallel \vec{c}$ -direction at a temperature of 20 K. The as-grown sample show no sign of absorption lines in the range between 4200 and 4300 cm<sup>-1</sup>, whereas well defined absorption lines appear at 4216 and 4247 cm<sup>-1</sup> after introduction of Ni. The peaks gradually increase as a function of in-diffusion temperature, consistent with the increasing integrated dose of Ni from the SIMS measurements. Moreover, the ratio between the two peaks appears to be the same for all the treated samples. A more accurate evaluation of the peak ratio is found by first integrating the absorption coefficient over the peak range, to yield an absorption peak intensity  $I$ . Table 4.5 gives the integrated intensity of the 4216 cm<sup>-1</sup> and 4247 cm<sup>-1</sup> absorption peaks together with their corresponding ratio. As can be seen, the ratio between the two peaks is nearly the same for all the samples, suggesting that they originate from the same defect. A broader peak at  $\sim 4323$  cm<sup>-1</sup> also appears in the spectra for the samples treated at high temperatures. This line has previously been observed to occur in the spectra of ZnO doped with Ni with approximately the same relative intensities to the 4216, 4240 and 4247 cm<sup>-1</sup> -transitions.[35]

The IR absorption spectra for the same samples, but measured in the  $\vec{k} \perp \vec{c}$ -direction, are shown in Figure 4.17. No absorption lines around 4200 cm<sup>-1</sup> are observed for the

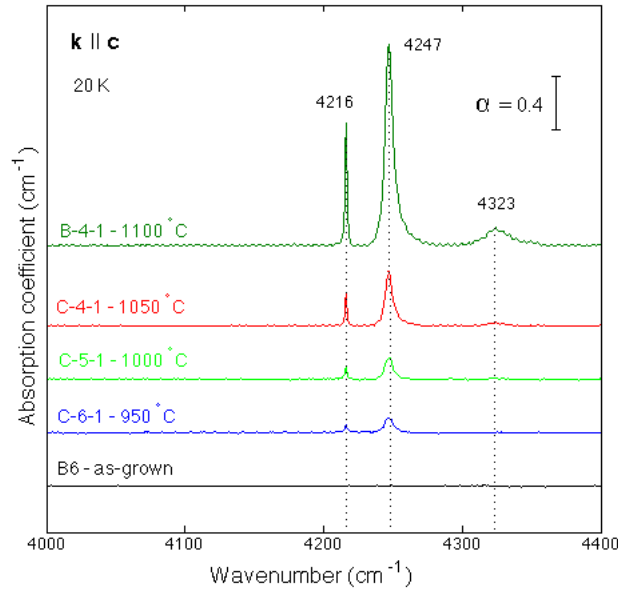


FIGURE 4.16: Comparison of the IR absorption spectra for the as-grown sample together with four corresponding samples deliberately doped with Ni from gas phase at temperatures 950°C, 1000°C, 1050°C and 1100°C for 90 min, as measured in the  $\vec{k} \parallel \vec{c}$ -orientation.

as-grown sample. Both the 4216  $\text{cm}^{-1}$  and 4247  $\text{cm}^{-1}$  lines emerge also in the  $\vec{k} \perp \vec{c}$ -orientation, though weaker than the lines observed in the  $\vec{k} \parallel \vec{c}$ -direction. In addition, an absorption line at 4240  $\text{cm}^{-1}$  appears in all the Ni-doped samples and is seen to be the dominant absorption line, consistent with previous observations [34]. Table 4.6 summarizes the peak intensities and the ratio of the peaks. The 4240  $\text{cm}^{-1}$  and 4247  $\text{cm}^{-1}$  peaks were not possible to resolve fully, and are therefore given as a total intensity. Furthermore, there is a weak indication of a broad peak emerging around 4323  $\text{cm}^{-1}$ , but it is too weak to be confirmed.

There is a significant difference in the Ni-related absorption peaks whether the IR measurement are performed in the  $\vec{k} \parallel \vec{c}$  or  $\vec{k} \perp \vec{c}$ -orientation, with a lower total intensity for the latter. This is in contrast to what is previously observed for as-grown HT ZnO with significant residual Ni impurities, Haug [57]. Moreover, the intensity of the 4216, 4240 and 4247  $\text{cm}^{-1}$  lines in Figure 4.17 are found to increase as a function of introduction temperature up to 1050°C. The sample treated at 1100°C is, however, found to deviate from this trend, with an apparent decrease in the intensity for the lines. This is unexpected, as the lines are believed to be from the same defect. A further discussion and a possible explanation of this, will be put forward in Section 4.6.2.

Figure 4.18 shows IR absorption spectra of the as-grown sample, A6, together with the samples A-3-1, A-1-1 and A-2-1 deliberately doped with Ni from gas phase (using a



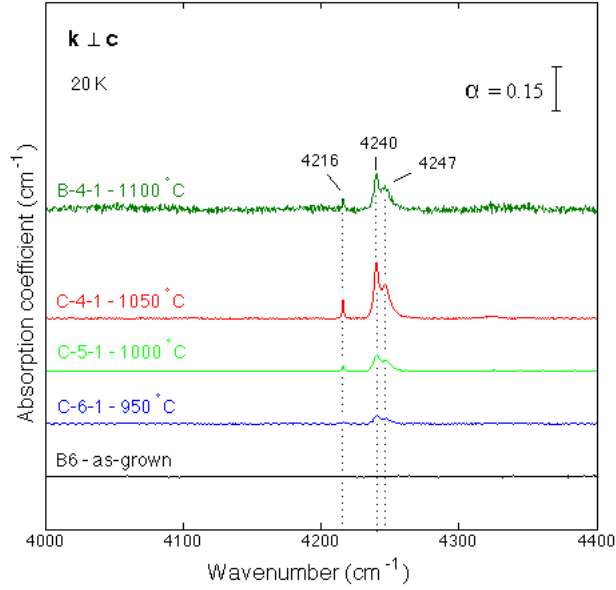


FIGURE 4.17: Comparison of the IR absorption spectra for the as-grown sample together with four corresponding samples deliberately doped with Ni from gas phase at temperatures 950°C, 1000°C, 1050°C and 1100°C for 90 min, as measured in the  $\vec{k} \perp \vec{c}$ -orientation.

Measurement			I (cm <sup>-2</sup> )		Ratio
Sample	Treatment	Orientation	4216	4240/4247	I <sub>4240/4247</sub> /I <sub>4216</sub>
B6	As-grown	$\vec{k} \perp \vec{c}$	-	-	-
C-6-1	Ni 950°C 90 min	$\vec{k} \perp \vec{c}$	s	0.25	-
C-5-1	Ni 1000°C 90 min	$\vec{k} \perp \vec{c}$	0.03	0.46	15.3
C-4-1	Ni 1050°C 90 min	$\vec{k} \perp \vec{c}$	0.08	1.36	17.0
B-4-1	Ni 1100°C 90 min	$\vec{k} \perp \vec{c}$	0.06	0.98	16.3

TABLE 4.6: IR peak intensities of the Ni related absorption peaks given by their integrated absorption coefficients, together with their ratio. '-' denotes no observable peak and 's' designates a small peak.

whole wire) for 24 hours at temperatures 950°C, 1000°C and 1050°C, respectively. The measurements were done in the  $\vec{k} \parallel \vec{c}$ -direction. Again, the as-grown sample show no sign of absorption lines around 4200 cm<sup>-1</sup>, whereas well defined absorption lines appear at 4216, and 4247 cm<sup>-1</sup> after introduction of Ni. The integrated intensity values of the 4216, and 4247 cm<sup>-1</sup> peaks are given in Table 4.7.

The Ni-related absorption peaks in Figure 4.18 have the largest intensity for the sample that was treated at the highest temperature. The samples treated at 950°C and 1000°C show almost no difference in the intensity. However, as pointed out in Section 3.6.2, processing failure occurred during the heat treatment of sample A-3-1 (950°C), resulting

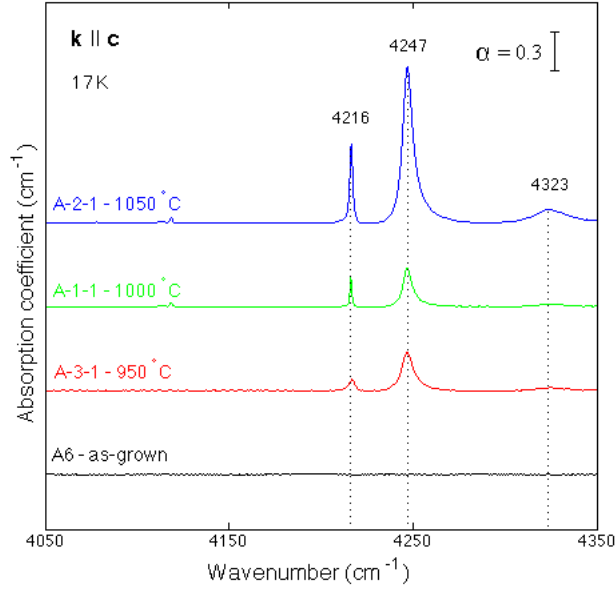


FIGURE 4.18: Comparison of the IR absorption spectra for the as-grown sample together with three corresponding samples deliberately doped with Ni from gas phase at temperatures 950°C, 1000°C and 1050°C for 24 hours, as measured in the  $\vec{k} \parallel \vec{c}$ -orientation.

Measurement			I (cm <sup>-2</sup> )		Ratio
Sample	Treatment	Orientation	4216	4247	I <sub>4247</sub> /I <sub>4216</sub>
A6	As-grown	$\vec{k} \parallel \vec{c}$	-	-	—
B6	As-grown	$\vec{k} \parallel \vec{c}$	-	-	—
A-3-1	Ni 950°C 24h	$\vec{k} \parallel \vec{c}$	0.50	3.48	7.0
A-1-1	Ni 1000°C 24h	$\vec{k} \parallel \vec{c}$	0.49	3.30	6.7
A-2-1	Ni 1050°C 24h	$\vec{k} \parallel \vec{c}$	2.17	14.42	6.6
B-1-1	Ni 1050°C 3h	$\vec{k} \parallel \vec{c}$	0.46	2.90	6.3
B-2-1	Ni 1100°C 2h	$\vec{k} \parallel \vec{c}$	1.58	11.49	7.3
A-4-1	Ni 1100°C 1h	$\vec{k} \parallel \vec{c}$	0.56	3.57	6.4

TABLE 4.7: IR peak intensities of the Ni related absorption peaks given by their integrated absorption coefficients. ‘-’ denotes no observable peak.

in an additional temperature ramping for this sample. This may explain the similar peak intensities at low temperatures. No IR-measurements were possible in the  $\vec{k} \perp \vec{c}$ -orientation for the samples, most likely caused by the high free carrier absorption.

Figure 4.19 shows a comparison of the IR spectra for the sample B-1-1 and A-2-1 deliberately doped in a closed quartz-ampoule containing Ni-wire at 1050°C for 3 and 24 hours, respectively. The measurements were performed in the  $\vec{k} \parallel \vec{c}$ -orientation. All the above mentioned Ni-related ( $\vec{k} \parallel \vec{c}$ -active) absorption peaks are also observed in

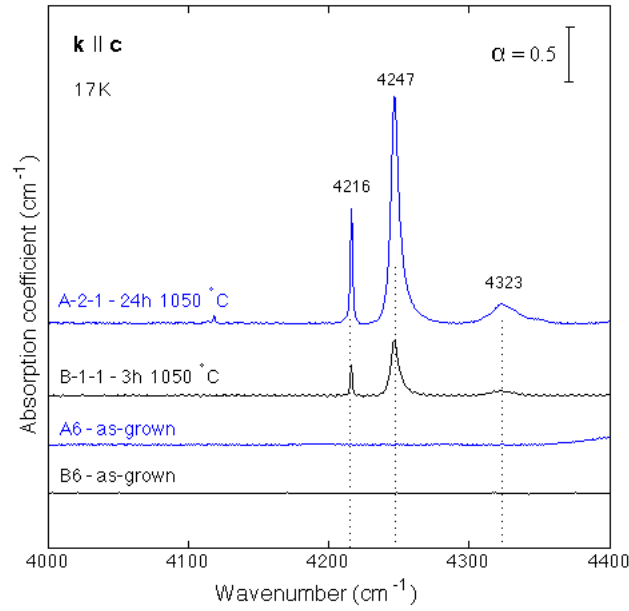


FIGURE 4.19: Comparison of the IR absorption spectra for the as-grown sample together with the samples B-1-1 and A-2-1 deliberately doped in a closed quartz-ampoule containing Ni-wire at 1050°C for 3h and 24h, respectively. Measured in the  $\vec{k} \parallel \vec{c}$ -orientation.

these Ni-doped samples. The total intensity of the 4216 and 4247  $\text{cm}^{-1}$  peaks is about a factor of 5 higher for the sample doped for 24 hours relative to those after 3h.

Figure 4.20 shows the IR absorption spectra of the samples A-5-1, A-4-1 and B-2-1, deliberately doped in a closed quartz-ampoule containing Ni-wire (whole) at 1100°C for 1, 1, and 2 hours, respectively. For A-5-1, a Zn-foil was included in the ampoule during the heat treatment. No signs of the 4216, 4247 and 4323  $\text{cm}^{-1}$  lines are found for the sample doped in Zn-rich atmosphere. Despite the low signal-to-noise ratio, any notable peaks would be expected to be visible. Furthermore, the total intensity of the 4216 and 4247  $\text{cm}^{-1}$  peaks is over 3 times higher for the sample treated for 2h (B-2-1) than that treated for 1h (A-4-1). This is inconsistent with the almost identical integrated dose of Ni observed from the SIMS measurements, indicating that the lateral non-uniformity is accidentally responsible for the apparent similar integrated SIMS-dose for the samples treated with (whole) Ni-wire.

It is interesting that there are no signs of the Ni-related lines for sample A-5-1, since it was observed by SIMS measurements in Section 4.2.2 (see Fig.4.6) to have a Ni concentration of  $\sim 2 \cdot 10^{17} \text{ cm}^{-3}$  at a depth of 8  $\mu\text{m}$  into the bulk. This suggests that the Zn-rich condition has affected the formation of substitutional  $\text{Ni}_{\text{Zn}}^0$ , or that it has

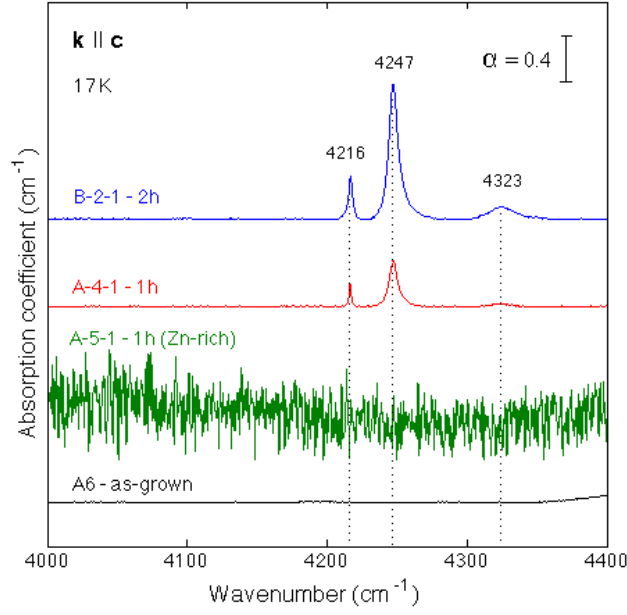


FIGURE 4.20: Comparison of the IR absorption spectra for the as-grown sample together with three samples deliberately doped in a closed quartz-ampoule containing Ni-wire at 1100°C for 1h and 2h, as measured in the  $\vec{k} \parallel \vec{c}$ -orientation. For sample A-5-1, a Zn-foil were present inside the ampoule during doping.

resulted in other Ni-related complexes, again consistent with the notion of interstitial Ni-diffusion under Zn-rich conditions.

#### 4.6.2 Effect of doping on the IR-transmission in the $\vec{k} \perp \vec{c}$ -direction

The Ni-related absorption lines observed in last section showed a considerable variation in intensity, whether the measurements were done in the  $\vec{k} \parallel \vec{c}$  or  $\vec{k} \perp \vec{c}$ -orientation. As these lines are considered to arise from internal electronic transitions of the same defect, this variation is unexpected. Furthermore, the measurement conducted in the  $\vec{k} \parallel \vec{c}$ -orientation (see Fig. 4.16) demonstrated a marked increase in the peak intensities as a function of treatment temperature. This was, however, not observed for the measurements performed in the  $\vec{k} \perp \vec{c}$ -orientation (see Fig. 4.17), and especially the sample B-4-1 (1100°C) deviated from this trend. One possible explanation for the difference in the absorption intensities between the two directions is that the doping of Ni causes a high free-carrier absorption, resulting in a relatively low IR-transmittance near the surface. This notion is illustrated for a  $\vec{k} \perp \vec{c}$ -measurement in Figure 4.21, and shows how a non-uniform distribution of the transmitted IR-light may arise due to the Ni-doped surface regions. The light that has propagated through the center of the sample and reaches the detector will thus suppress the information contained in the light that has

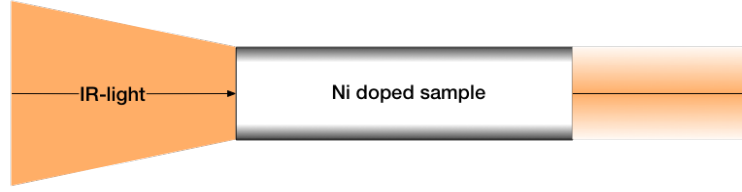


FIGURE 4.21: Illustration of the transmittance of IR-light through a Ni-doped sample in the  $\vec{k} \perp \vec{c}$ -orientation. The transmitted light shows a non-uniform distribution caused by a higher free carrier absorption in the doped regions.

passed through the Ni-doped regions. This would result in a lower apparent absorption intensity for any active defect that may be located near the surface.

This would also be the case for a measurement performed in the  $\vec{k} \parallel \vec{c}$ -direction, as diffusion of Ni is to expect also in the  $\vec{k} \perp \vec{c}$ -orientation for the closed quartz-ampoule doping. However, the extent of these Ni-doped regions would be relatively small compared to the total transfer area ( $\sim 0.3 \times 0.5 \text{ cm}^2$ ), such that the effect is practically negligible for measurements in the  $\vec{k} \parallel \vec{c}$ -direction.

This could also explain why the sample B-4-1 in Figure 4.17 shows a lower-than-expected absorption intensity for the 4216, 4240 and 4247  $\text{cm}^{-1}$  lines, as it holds a deeper Ni-diffusion profile (Fig. 4.7) and a higher dose of Ni (Tab. 4.2) than the samples treated at lower temperatures. Assuming that the free-carrier density is higher in the doped regions, a higher free-carrier absorption would be expected for B-4-1, resulting in a higher non-uniformity of the transmitted IR-light and an apparent reduction in the Ni-related absorption peaks. This interpretation could also be supported by resistivity measurements. Sample B-4-1 (1100°C) is found to have a resistivity of 0.2  $\Omega\text{cm}$ , which is lower than what was measured for the samples C-4-1 (0.4  $\Omega\text{cm}$ ), C-5-1 (1.0  $\Omega\text{cm}$ ) and C-6-1 (1.7  $\Omega\text{cm}$ ), treated at 1050°C, 1000°C and 950°C, respectively. However, this argument is only valid if the variation in resistivity originates from the doped regions (e.g.,  $\text{Ni}_{\text{Zn}}^+$  acting as a donor). This is not necessarily the case, as the carrier density of HT grown ZnO previously has been observed to progressively increase after heat treatments in ambient air at temperatures up to 1500°C.[27] The observed decrease in resistivity as a function of introduction temperature, may therefore also result from the effect of the temperature itself (e.g., out diffusion of unintentionally introduced acceptor-like impurities), rather than as a direct consequence of the amount of incorporated Ni.

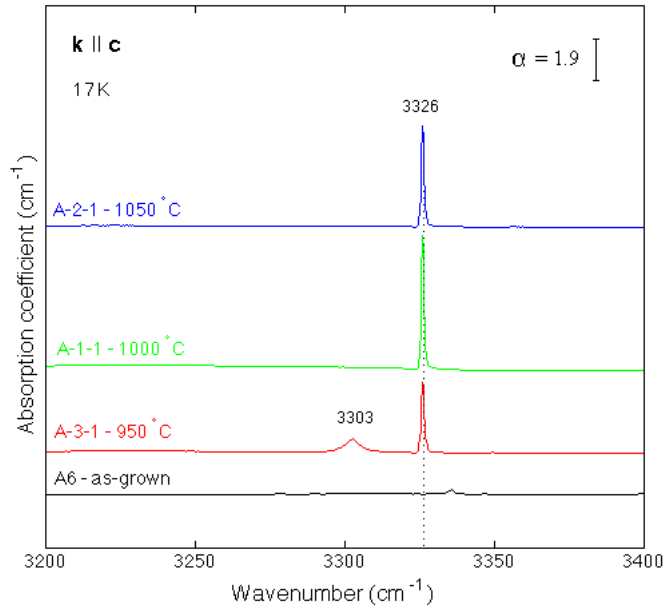


FIGURE 4.22: IR absorption spectra of the samples deliberately doped in a closed quartz-ampoule containing Ni-wire for 24h at 950, 1000 and 1050 °C, as measured in the  $\vec{k} \parallel \vec{c}$ -orientation.

#### 4.6.3 O-H localized vibrational modes

Figure 4.22 shows the IR absorption spectra of the samples A-3-1, A-1-1 and A-2-1 deliberately doped in a closed quartz-ampoule containing Ni-wire for 24 hours at 950, 1000 and 1050 °C, respectively. As can be seen, a line at  $3326 \text{ cm}^{-1}$  emerges after the introduction of Ni. This line has previously been observed by McCluskey et al. [58] after in-diffusion of hydrogen in single crystal ZnO. Different models have been proposed for the  $3326 \text{ cm}^{-1}$  line, and more recently a calcium-hydrogen (CaH) complex [59] and a Zn vacancy passivated by a hydrogen atom in the negative charge state ( $V_{Zn}H^-$ ) have been suggested [60].

From the SIMS measurements presented in Section 4.2 there is reason to believe that the samples A-3-1, A-1-1 and A-2-1 were in a Zn-rich condition during the long-lasting introduction of Ni. It would, therefore, be interesting to measure the Ca concentration for these samples. No such measurements have been performed, and it is beyond the scope of this work to conclude on this subject.

Figure 4.23 shows the IR absorption spectra of the sample A-4-1 deliberately doped in closed quartz-ampoule containing Ni wire at 1100°C for 1 hour, together with the effect of additional (subsequent) heat treatments in ambient air at 700 and 800 °C for 30 min. The  $3577 \text{ cm}^{-1}$  line is observed to increase marginally, while the 3336 and 3483

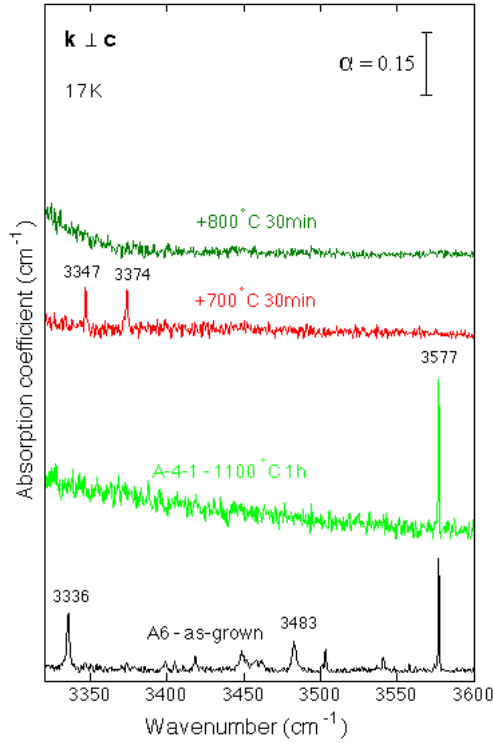


FIGURE 4.23: IR absorption spectra of the as-grown sample A6, together with the sample A-4-1 deliberately doped in closed quartz-ampoule containing Ni-wire, and after additional heat treatments for 30 min at 700 and 800 °C. The measurements are performed in the  $\vec{k} \perp \vec{c}$ -orientation.

$\text{cm}^{-1}$  lines disappear after the introduction of Ni. After additional heat treatments in ambient air at 700°C, two new lines emerge at 3347 and 3374  $\text{cm}^{-1}$  and then disappear after further heat treatment at 800°C. Lavrov et al. [61], have previously ascribed these latter lines to a  $(\text{OH})_2\text{-Cu}_{\text{Zn}}$  complex, and Cu might have been unintentionally introduced during the additional heat treatment in air. More surprisingly, the 3577  $\text{cm}^{-1}$  line is observed to disappear after heat treatment at 700°C for 30 min. As mentioned in Section 4.5, this line is attributed to a OH-Li complex and has previously been shown by Lavrov et al. [32] to be highly stable, even withstanding heat treatment at 1200°C for 30 min. On the other hand, Johansen et al. [55] have demonstrated that this is not the true stability of the OH-Li complex, but rather reflects the recapture of H by  $\text{Li}_{\text{Zn}}$  during the cooling down process. The results in Figure 4.23 would imply that such a recapture is suppressed in sample A-4-1, but it is beyond the scope of this work to conclude on this subject. However, it is possible to suggest that the introduction of Ni could also be accompanied by other impurities, which subsequently affect the dissociation or recapturing of the OH-Li complex during the additional heat treatment in air.

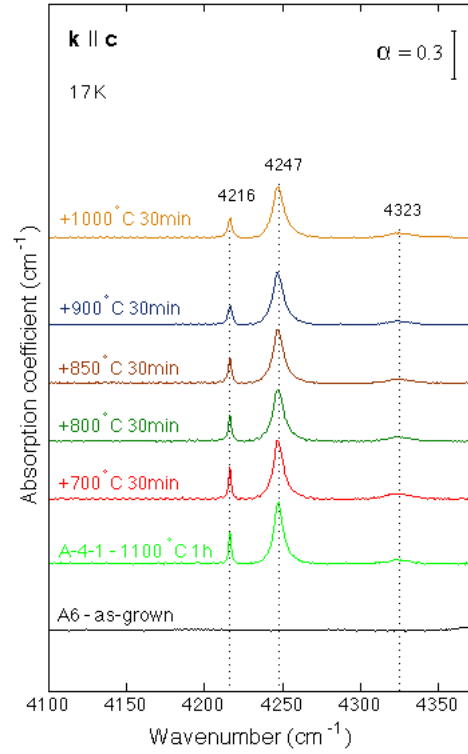


FIGURE 4.24: IR-spectra showing the thermal stability of the Ni-related absorption lines for the sample A-4-1, deliberately doped in a closed quartz-ampoule containing Ni-wire, as measured in the  $\vec{k} \parallel \vec{c}$ -orientation. The additional heat treatments were performed in ambient air for 30 min at temperatures ranging 700 - 1000 °C.

#### 4.6.4 Thermal stability

Figure 4.24 shows the IR absorption spectra of the sample A-4-1 deliberately doped in a closed quartz-ampoule containing Ni-wire, and after additional heat treatments in ambient air for 30 min at temperatures ranging from 700 to 1000 °C, as measured in the  $\vec{k} \parallel \vec{c}$ -direction. No significant variation in the intensity of the 4216, 4247 and 4323  $\text{cm}^{-1}$  peaks is observed, showing that the Ni-defect is stable for heat treatments up to 1000°C for 30 min. Figure 4.25 shows how the resistivity changes after doping and subsequent heat treatments. After doping, the resistivity is practically unchanged as compared to its as-grown state. After additional heat treatment a doubling in the resistivity is observed, and then it remains almost uncanged upon further heat treatments.

Figure 4.26 shows the IR spectra for the same samples as in Figure 4.24, but displays the region characteristic for O-H stretch modes. All the main absorption lines in the as-grown sample disappear after the Ni-doping. New lines at 3303, 3347 and 3374  $\text{cm}^{-1}$  appear after the doping. The 3303  $\text{cm}^{-1}$  line has previously been assigned by Haug



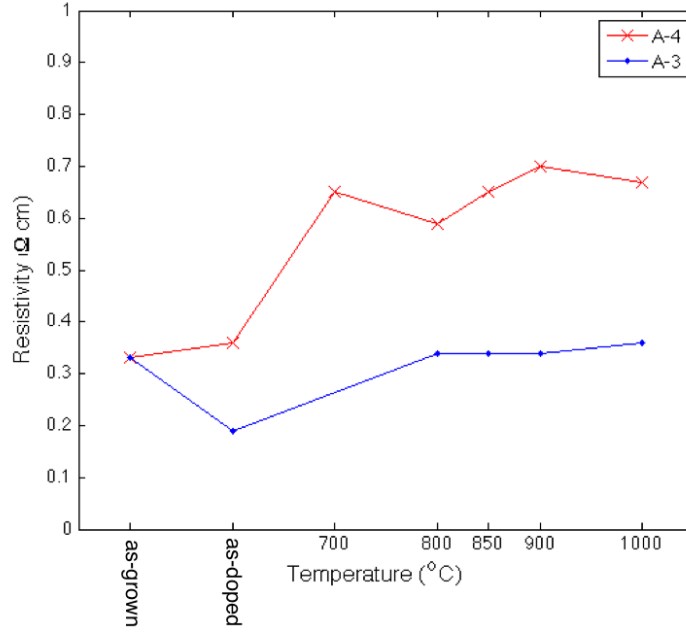


FIGURE 4.25: Resistivities of the samples A-4 and A-3 deliberately doped in a closed quartz-ampoule with Ni-wire at 1100°C for 1h and at 950°C for 24h, respectively. Also shown: resistivities after additional heat treatments at temperatures in the range 700 - 1000°C at ambient conditions.

[57] to consist of two O-H bonds associated to an unknown impurity atom, while the 3347 and 3374  $\text{cm}^{-1}$  lines have been ascribed to a  $(\text{OH})_2\text{-Cu}_{\text{Zn}}$  complex, as discussed in Section 4.6.3. After additional heat treatment in ambient air, the 3303  $\text{cm}^{-1}$  line disappears and a new line at 3315  $\text{cm}^{-1}$  emerges. The 3315  $\text{cm}^{-1}$  line has previously been observed by Haug [57] in HT grown ZnO after heat treatment in mixed  $\text{H}_2/\text{D}_2$  gas, but have not been ascribed to a known impurity, to our knowledge.

## 4.7 Ni absorption strength

From the measured Ni concentration profiles and the Ni absorption lines it is possible to evaluate a minimum absorption strength  $\epsilon$  for the  $\text{Ni}_{\text{Zn}}^0$  defect, as defined in Eq. 2.31. The results for the samples that were intentionally doped by Ni in a closed quartz-ampoule are given in Table 4.9, for both the  $\vec{k} \parallel \vec{c}$  and  $\vec{k} \perp \vec{c}$ -orientation. The integrated absorption  $I$  is given as a total of the 4216, 4240 and 4247  $\text{cm}^{-1}$  lines, and the average Ni concentration has been estimated from the measured dose of the profiles, as given in Tables 4.1 and 4.2. Where the Ni depth profiles were measured only at Zn face, an equivalent dose was assumed at O-face. As can be seen, the value of  $\epsilon_{\text{Ni}}$  in the  $\vec{k} \parallel \vec{c}$ -direction varies with a factor of 8.3 depending on the sample treatment. It must

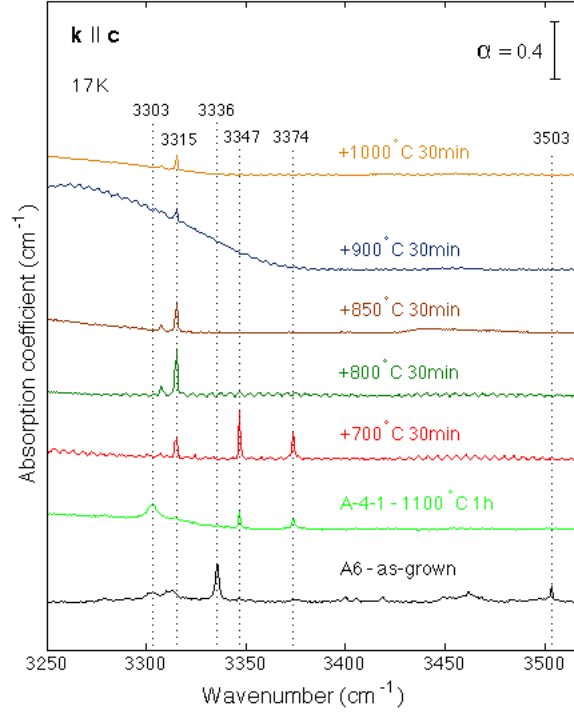


FIGURE 4.26: IR-spectra showing the thermal stability of the O-H absorption lines for the sample A-4-1, deliberately doped in a closed quartz-ampoule containing Ni-wire, as measured in the  $\vec{k} \parallel \vec{c}$ -orientation. The additional heat treatments were performed in ambient air for 30 min at temperatures ranging 700 - 1000 °C.

be recalled that the samples doped from a whole Ni-wire revealed a high lateral non-uniformity in the Ni concentration vs depth profiles. The samples that did show a good consistency in the SIMS measurements were C-4-1, C-5-1 and C-6-1, and will therefore be considered as the only truly reliable samples for the estimation of  $\epsilon_{Ni}$ . In that case, the value of  $\epsilon_{Ni}$  is seen to vary only by a factor of 1.25 in the  $\vec{k} \parallel \vec{c}$ -orientation.

The absorption strength in the  $\vec{k} \perp \vec{c}$ -orientation is found to be almost an order of magnitude lower than what is observed along the c-axis. This can be explained by the model presented in Section 4.6.2, where it was proposed that the IR absorption measurements in the  $\vec{k} \perp \vec{c}$ -direction are affected by the doped Ni-regions, to yield an apparent decrease in the Ni-related absorption lines.

It is important to realize that the values for  $\epsilon_{Ni}$  assume that all of the Ni atoms measured by SIMS contribute to the absorption. This may not be the case, as Ni could also be found in other configurations and charge states. The true  $\epsilon_{Ni}$  is thus either equal to or larger than the highest value estimated in Table 4.9. The largest reliable  $\epsilon_{Ni}$  is found

Measurement		4-point probe
Sample	Treatment	Resistivity $\rho$ ( $\Omega\text{cm}$ )
A6	As-grown	0.33
A-1-1	Ni-wire 1000 °C 24h	0.26
A-2-1	Ni-wire 1050 °C 24h	0.30
A-3-1	Ni-wire 950 °C 24h	0.19
A-3-2	800 °C 30 min	0.34
A-3-3	850 °C 30 min	0.34
A-3-4	900 °C 30 min	0.34
A-3-5	1000 °C 30 min	0.36
A-4-1	Ni-wire 1100 °C 1h	0.36
A-4-2	700 °C 30 min	0.65
A-4-3	800 °C 30 min	0.59
A-4-4	850 °C 30 min	0.65
A-4-5	900 °C 30 min	0.70
A-4-6	1000 °C 30 min	0.67
A-5-1	Ni-wire + Zn-foil 1100 °C 1h	0.031
B6	As-grown	2618 (given)
B-1-1	Ni-wire 1050 °C 3h	0.20
B-2-1	Ni-wire 1100 °C 2h	NO
B-3-1	Ni-pieces 1100 °C 1h (vac)	0.21
B-4-1	Ni-pieces 1100 °C 90min	0.20
C-1-2	NiO-film 900 1h°C	NO
C-2-2	NiO-film 1100 1h°C	106
C-3-2	NiO-film 1200 1h°C	5.4
C-4-1	Ni-pieces 1050 °C 90min	0.40
C-5-1	Ni-pieces 1000 °C 90min	1.01
C-6-1	Ni-pieces 950 °C 90min	1.71
D-3-1	ZnO:Ni-film as-sputtered	986
D-1-2	ZnO:Ni-film 950°C 1h	4090
D-2-2	ZnO:Ni-film 1100°C 1h	10.7
D-3-2	ZnO:Ni-film 1050°C 1h	32.7
D-4-2	ZnO:Ni-film 1150°C 1h	6.1

TABLE 4.8: Resistivity of all the samples and for the subsequent annealing, measured on Zn-face.

for sample C-6-1 in the  $\vec{k} \parallel \vec{c}$ -orientation, thus resulting in an absorption strength of

$$\epsilon_{Ni} \geq 1.5 \cdot 10^{-17} \text{ cm.} \quad (4.2)$$

One plausible explanation for the difference in  $\epsilon_{Ni}$  is that the higher Ni concentration in C-4-1 and C-5-1 leads to formation of other Ni-related complexes than  $\text{Ni}_{\text{Zn}}$ , resulting in a relatively lower absorption. Another possibility is that the doping at high temperatures result in a higher proportion of  $\text{Ni}_i$  due to a more Zn-rich condition caused by a faster oxidation of the source. Furthermore, it may be the case that not all the Ni ions present

Sample	$I_{\text{Ni,tot}}(\vec{k} \parallel \vec{c})$ (cm <sup>-2</sup> )	$I_{\text{Ni,tot}}(\vec{k} \perp \vec{c})$ (cm <sup>-2</sup> )	Average $[Ni]$ (cm <sup>-3</sup> )	$\epsilon_{\text{Ni}}(\vec{k} \parallel \vec{c})$ (cm)	$\epsilon_{\text{Ni}}(\vec{k} \perp \vec{c})$ (cm)
A6	0	0	$\leq 1 \cdot 10^{16}$	-	-
A-3-1	3.98	-	$1.3 \cdot 10^{17}$	$3.1 \cdot 10^{-17}$	-
A-1-1	3.79	-	$2.4 \cdot 10^{17}$	$1.6 \cdot 10^{-17}$	-
A-2-1	16.59	-	$5.0 \cdot 10^{17}$	$3.3 \cdot 10^{-17}$	-
A-4-1	4.13	-	$2.1 \cdot 10^{17}$	$2.0 \cdot 10^{-17}$	-
B6	0	0	$\leq 1 \cdot 10^{16}$	-	-
C-6-1	0.96	0.25	$6.2 \cdot 10^{16}$	$1.5 \cdot 10^{-17}$	$4.0 \cdot 10^{-18}$
C-5-1	1.32	0.49	$1.1 \cdot 10^{17}$	$1.2 \cdot 10^{-17}$	$4.5 \cdot 10^{-18}$
C-4-1	3.41	1.44	$2.7 \cdot 10^{17}$	$1.3 \cdot 10^{-17}$	$5.3 \cdot 10^{-18}$
B-4-1	14.31	1.0	$5.0 \cdot 10^{17}$	$2.9 \cdot 10^{-17}$	$2.0 \cdot 10^{-18}$
B-1-1	3.36	-	$3.4 \cdot 10^{17}$	$9.9 \cdot 10^{-18}$	-
B-2-1	13.07	-	$1.6 \cdot 10^{17}$	$8.2 \cdot 10^{-17}$	-

TABLE 4.9: Estimated absorption cross sections  $\epsilon_{\text{Ni}}$  for the Ni absorption lines at 4216, 4240 and 4247 cm<sup>-1</sup>.

in the samples C-4-1 and C-5-1 take part in the absorption because they are not in the effectively neutral charge state,  $\text{Ni}_{\text{Zn}}^0$ . Schulz and Thiede [56], have previously observed that Ni in ZnO shows luminescence from another charge state, suggesting a single donor-like behaviour,



This indicates that sample C-6-1 (1.7  $\Omega\text{cm}$ ) would have an effectively lower concentration of  $\text{Ni}_{\text{Zn}}^0$  than C-4-1 (0.4  $\Omega\text{cm}$ ) and C-5-1 (1.0  $\Omega\text{cm}$ ), such that a lower apparent absorption strength would be expected for the sample C-6-1. This is, however, disputed by the observed values of  $\epsilon_{\text{Ni}}$ , which show a higher absorption strength for the most resistive sample (C-6-1). Consequently, the perhaps most likely explanation for the variation in  $\epsilon_{\text{Ni}}$  is that a formation of other Ni-related complexes increases as a function of Ni-concentration, or that the proportion of Ni at interstitial lattice site increases as a function of introduction temperature (a faster change toward a more Zn-rich condition).

# Chapter 5

## Summary

Hydrothermal grown ZnO single crystals, have been doped by in-diffusion of Ni from gas phase, NiO-film and ZnO:Ni-film, and then investigated by SIMS, FTIR and four-point resistivity measurements.

### 5.1 Conclusion

Experimental data for in-diffusion of Ni from gas phase have been modelled with the semi-infinite source model, yielding an activation energy for the diffusivity of 4.3 eV and a pre-exponential factor of  $6 \cdot 10^4 \text{ cm}^2\text{s}^{-1}$ . It is suggested that these high values estimated for the diffusion parameters are due to a change in the ZnO stoichiometry, toward a Zn-rich condition during the gas phase experiments. It is further proposed that both a vacancy mediated and an interstitial mechanism are operative, where the former one dominates during O-rich conditions, while the latter one prevails during Zn-rich conditions.

In-diffusion of Ni under O-rich conditions from Ni-doped ZnO-film has revealed a rather complex process. It is observed that the diffusion of Ni resembles a box-profile, which increases in concentration and depth as a function of temperature up to 1100°C. At higher temperature it appears that a different and faster diffusion mechanism is involved, possibly an interstitial-related mechanism.

Absorption lines at 4216, 4240 and 4247  $\text{cm}^{-1}$ , previously assigned to internal electronic transitions of substitutional  $\text{Ni}_{\text{Zn}}^0$  [30, 31, 35, 56], are observed in the Ni-doped samples. The intensity of the lines is found to correlate with the total concentration of Ni, thus supporting the original assignment of these lines. In addition, a broad absorption line at 4323  $\text{cm}^{-1}$  is detected with approximately the same relative intensity to the other

transitions in the different samples. An absorption strength of  $\epsilon_{Ni} \geq 1.5 \cdot 10^{-17}$  cm has been estimated for the 4216, 4240 and 4247  $\text{cm}^{-1}$  lines.

## 5.2 Suggestions for further research

First of all, an applicable model should be developed in order to satisfactorily explain the diffusion of Ni from the gas-phase experiments. New isothermal experiments would provide further insight into the suggested two-step diffusion process, which can then be used to estimate the influence of the changing conditions during the in-diffusion treatment. This could possibly yield a measure of the proposed kick-out mechanism as a function of time.

Additional in-diffusion experiments from Ni-doped ZnO-film are needed in order to comprehend the diffusive behaviour of Ni under O-rich conditions. Isochronal heat treatments above 1150°C would provide an extended view of the process, while isothermal heat treatments carried out at e.g., 1100°C would give deeper insight into the behaviour of the Ni box like profiles. It was also observed that the Ni concentration in the sputtered films was gradually drained during the in-diffusion treatments. For that reason, greater efforts with regard to the quality of the deposited film should be carried out in order to obtain a film which can be considered as a semi-infinite source, preferably with the use of a sputtering assembly designed to handle magnetic targets.

It would be of interest to measure the Ca concentration in the samples doped from gas phase for 24h, which revealed the 3326  $\text{cm}^{-1}$  absorption line. This could potentially shed light on whether the CaH-complex model [59] or the  $V_{Zn}H^-$  model [60], that have previously been proposed for the 3326  $\text{cm}^{-1}$  line, is the correct model.

The observed disappearance of the 3577  $\text{cm}^{-1}$  absorption line after heat treatment in ambient air at 700°C for 30 min, would be interesting to follow up with new experiments. Similar doped samples that also display this line are in possession and can therefore, without further in-diffusion experiments, undergo corresponding additional heat treatments in ambient air to elucidate the kinetics of the defect of the 3577  $\text{cm}^{-1}$  line.

## Appendix A

### IR peak intensities

All the measured IR absorption peak intensities, given as the integrated absorption coefficient, presented in this work are listed in Table A.1. The integration was performed by defining a point on each side of the peak range, drawing a straight line between these two points and extract the enclosed area.

Measurement			Absorption peaks (cm <sup>-2</sup> )															
Sample	Treatment	Orientation	O-H LVM's												Ni <sup>2+</sup> -transitions			
			3192	3303	3315	3326	3336	3347	3374	3483	3503	3508	3516	3577	4216	4240	4247	4323
A-1-1	Ni 1000°C 24h	$\vec{k} \parallel \vec{c}$	-	-	-	6.56	-	-	-	-	-	-	-	-	0.49	-	3.30	s
A-1-1	Ni 1000°C 24h	$\vec{k} \perp \vec{c}$	NO	NO	NO	NO	NO	NO	NO	NO	NO	NO	NO	NO	NO	NO	NO	NO
A-2-1	Ni 1050°C 24h	$\vec{k} \parallel \vec{c}$	-	-	-	5.19	-	-	-	-	-	-	-	-	2.17	-	14.42	3.28
A-2-1	Ni 1050°C 24h	$\vec{k} \perp \vec{c}$	NO	NO	NO	NO	NO	NO	NO	NO	NO	NO	NO	NO	NO	NO	NO	NO
A-3-1	Ni 950°C 24h	$\vec{k} \parallel \vec{c}$	-	2.94	-	4.0	-	-	-	-	-	-	-	-	0.50	-	3.48	s
A-3-1	Ni 950°C 24h	$\vec{k} \perp \vec{c}$	NO	NO	NO	NO	NO	NO	NO	NO	NO	NO	NO	NO	NO	NO	NO	NO
A-3-2	800°C 30 min	$\vec{k} \parallel \vec{c}$	-	-	0.44	-	-	0.37	0.15	-	-	-	-	-	0.33	-	1.63	s
A-3-2	800°C 30 min	$\vec{k} \perp \vec{c}$	-	-	0.59	-	-	0.67	0.24	-	-	-	-	-	-	s	-	-
A-3-3	850°C 30 min	$\vec{k} \parallel \vec{c}$	-	-	0.83	-	-	0.13	s	-	-	-	-	-	0.39	-	2.02	s
A-3-3	850°C 30 min	$\vec{k} \perp \vec{c}$	-	-	0.57	-	-	0.16	s	-	-	-	-	-	-	s	-	-
A-3-4	900°C 30 min	$\vec{k} \parallel \vec{c}$	-	-	0.58	-	-	-	-	-	-	-	-	-	0.35	-	1.91	s
A-3-4	900°C 30 min	$\vec{k} \perp \vec{c}$	-	-	0.31	-	-	-	-	-	-	-	-	-	-	s	-	-
A-3-5	1000°C 30 min	$\vec{k} \parallel \vec{c}$	-	-	0.19	-	-	-	-	-	-	-	-	-	0.30	-	2.28	s
A-3-5	1000°C 30 min	$\vec{k} \perp \vec{c}$	-	-	s	-	-	-	-	-	-	-	-	-	-	s	-	-
A-4-1	Ni 1100°C 1h	$\vec{k} \parallel \vec{c}$	s	0.57	-	-	-	0.12	0.08	-	-	-	-	-	0.56	-	3.57	s
A-4-1	Ni 1100°C 1h	$\vec{k} \perp \vec{c}$	-	-	-	-	-	-	-	-	-	-	-	0.56	-	s	-	-
A-4-2	700°C 30 min	$\vec{k} \parallel \vec{c}$	-	-	0.18	-	-	0.32	0.24	-	-	-	-	-	0.56	-	3.46	s
A-4-2	700°C 30 min	$\vec{k} \perp \vec{c}$	-	-	-	-	-	s	s	-	-	-	-	-	-	s	-	-
A-4-3	800°C 30 min	$\vec{k} \parallel \vec{c}$	-	-	0.40	-	-	-	-	-	-	-	-	-	0.44	-	2.96	s
A-4-3	800°C 30 min	$\vec{k} \perp \vec{c}$	-	-	-	-	-	-	-	-	-	-	-	-	-	s	-	-
A-4-4	850°C 30 min	$\vec{k} \parallel \vec{c}$	-	-	0.25	-	-	-	-	-	-	-	-	-	0.30	-	2.85	s
A-4-4	850°C 30 min	$\vec{k} \perp \vec{c}$	-	-	-	-	-	-	-	-	-	-	-	-	-	s	-	-
A-4-5	900°C 30 min	$\vec{k} \parallel \vec{c}$	-	-	0.12	-	-	-	-	-	-	-	-	-	0.43	-	2.96	s
A-4-5	900°C 30 min	$\vec{k} \perp \vec{c}$	-	-	-	-	-	-	-	-	-	-	-	-	-	s	-	-
A-4-6	1000°C 30 min	$\vec{k} \parallel \vec{c}$	-	-	0.12	-	-	-	-	-	-	-	-	-	0.41	-	3.13	s
A-4-6	1000°C 30 min	$\vec{k} \perp \vec{c}$	-	-	-	-	-	-	-	-	-	-	-	-	-	s	-	-
A-5-1	Ni + Zn 1100°C 1h	$\vec{k} \parallel \vec{c}$	NO	NO	NO	NO	NO	NO	NO	NO	NO	NO	NO	NO	NO	NO	NO	NO
A-5-1	Ni + Zn 1100°C 1h	$\vec{k} \perp \vec{c}$	NO	NO	NO	NO	NO	NO	NO	NO	NO	NO	NO	NO	NO	NO	NO	NO
A6	As-grown	$\vec{k} \parallel \vec{c}$	-	-	-	-	0.44	-	-	-	0.09	-	-	-	-	-	-	-
A6	As-grown	$\vec{k} \perp \vec{c}$	-	-	-	-	0.22	-	-	0.25	0.05	-	-	0.30	-	-	-	-
B-1-1	Ni 1050°C 3h	$\vec{k} \parallel \vec{c}$	-	6.12	-	-	-	-	-	-	-	-	-	-	0.46	-	2.90	s
B-1-1	Ni 1050°C 3h	$\vec{k} \perp \vec{c}$	NO	NO	NO	NO	NO	NO	NO	NO	NO	NO	NO	NO	NO	NO	NO	NO
B-2-1	Ni 1100°C 2h	$\vec{k} \parallel \vec{c}$	-	3.22	-	-	-	-	-	-	-	-	-	-	1.58	-	11.49	2.28
B-2-1	Ni 1100°C 2h	$\vec{k} \perp \vec{c}$	NO	NO	NO	NO	NO	NO	NO	NO	NO	NO	NO	NO	NO	s	s	-
B-3-1	Ni 1100°C 1h (vac)	$\vec{k} \parallel \vec{c}$	NO	NO	NO	NO	NO	NO	NO	NO	NO	NO	NO	NO	NO	NO	NO	NO
B-3-1	Ni 1100°C 1h (vac)	$\vec{k} \perp \vec{c}$	NO	NO	NO	NO	NO	NO	NO	NO	NO	NO	NO	NO	NO	NO	NO	NO
B-4-1	Ni 1100°C 90min	$\vec{k} \parallel \vec{c}$	2.17	1.34	-	-	-	-	-	-	-	-	-	-	1.70	-	12.22	2.81
B-4-1	Ni 1100°C 90min	$\vec{k} \perp \vec{c}$	-	-	-	-	-	-	-	-	-	-	-	0.13	0.06	0.88*	s	-
B6	Ni As-grown	$\vec{k} \parallel \vec{c}$	-	-	-	-	1.75	-	-	0.15	-	s	s	-	-	-	-	-
B6	Ni As-grown	$\vec{k} \perp \vec{c}$	-	-	-	-	0.88	-	-	0.67	-	0.04	0.28	1.34	-	-	-	-
C-3-1	NiO-film	$\vec{k} \parallel \vec{c}$	-	-	-	-	2.77	-	-	-	-	-	-	-	-	-	-	-
C-3-1	NiO-film	$\vec{k} \perp \vec{c}$	-	-	-	-	1.15	-	-	1.23	-	s	0.40	1.44	-	-	-	-
C-1-2	900 °C 1h	$\vec{k} \parallel \vec{c}$	-	-	-	-	-	-	-	-	-	-	-	-	-	-	-	-
C-1-2	900 °C 1h	$\vec{k} \perp \vec{c}$	-	-	-	-	-	-	-	-	-	-	-	2.17	-	-	-	-
C-2-2	1100 °C 1h	$\vec{k} \parallel \vec{c}$	-	-	-	-	-	-	-	-	-	-	-	-	0.3	-	2.5	s
C-2-2	1100 °C 1h	$\vec{k} \perp \vec{c}$	-	-	-	-	-	-	-	-	-	-	-	3.22	-	1.32*	s	-
C-3-2	1200 °C 1h	$\vec{k} \parallel \vec{c}$	-	-	-	-	-	-	-	-	-	-	-	-	0.8	-	9.8	2.1
C-3-2	1200 °C 1h	$\vec{k} \perp \vec{c}$	-	-	-	-	-	-	-	-	-	-	-	3.28	0.10	2.97*	s	s
C-4-1	Ni 1050 °C 90min	$\vec{k} \parallel \vec{c}$	3.08	0.89	-	-	-	-	-	-	-	-	-	-	0.43	-	2.91	0.49
C-4-1	Ni 1050 °C 90min	$\vec{k} \perp \vec{c}$	0.68	-	-	-	-	-	-	-	-	-	-	3.77	0.08	1.36*	s	s
C-5-1	Ni 1000 °C 90min	$\vec{k} \parallel \vec{c}$	1.26	0.95	-	-	-	-	-	-	-	-	-	-	0.19	-	1.11	s
C-5-1	Ni 1000 °C 90min	$\vec{k} \perp \vec{c}$	0.25	-	-	-	-	-	-	-	-	-	-	3.66	0.02	0.47*	s	-
C-6-1	Ni 950 °C 90min	$\vec{k} \parallel \vec{c}$	1.96	s	-	-	-	-	-	-	-	-	-	-	0.08	-	0.74	-
C-6-1	Ni 950 °C 90min	$\vec{k} \perp \vec{c}$	0.31	-	-	-	-	-	-	-	-	-	-	3.37	s	0.23*	s	-

TABLE A.1: List of all the IR peak intensities reported in this work, given by their integrated absorption coefficients. '-' denotes no observable peak. 's' denotes a small peak, in instances where the intensity could not be accurately determined. 'NO', denotes that spectroscopic data were not obtainable in the respective region, e.g because of too high electronic absorption. Finally, \* denotes that the value is given as the total integrated area under the 4240 and 4247 cm<sup>-1</sup> peaks.



## Appendix B

# Process development

### B.1 NiO-film deposition by E-beam evaporation

Section 3.6.4 presented a method for doping ZnO-bulk material by Ni from a pre-deposited NiO-film obtained by E-beam evaporation. The development steps carried out to determine the optimal working pressure for the formation of NiO will be described in the following.

The deposition of NiO was performed by evaporating a Ni source while maintaining an oxygen-leak into the chamber. Two pieces of glass were used as test samples. The first sample was deposited for 1 hour with an oxygen-leak corresponding to a working pressure of  $2 \cdot 10^{-4}$  mbar, and labeled  $S_1$ . The other sample was deposited for 30 min at a working pressure of  $6 \cdot 10^{-4}$  mbar, and labeled  $S_2$ . The deposition rate was maintained at  $\sim 0.5 \text{ \AA s}^{-1}$ .

For characterizing the deposited films the samples were analysed by the Bruker AXS D8 Discover X-ray diffraction (XRD) measurement system. Figure B.1 and Figure B.2 shows the XRD-spectra of sample  $S_1$  and  $S_2$ , respectively. As can be seen, NiO-related reflections are observed for both the samples. However, sample  $S_1$  (Fig. B.1) also shows a Ni-related (111) reflection at  $44.5^\circ$ , indicating that the film is a composite of Ni and NiO. The spectra of sample  $S_2$  (Fig. B.2) show no sign of any Ni-reflections, and therefore suggests a working pressure of  $6 \cdot 10^{-4}$  mbar for the formation of a NiO-film.

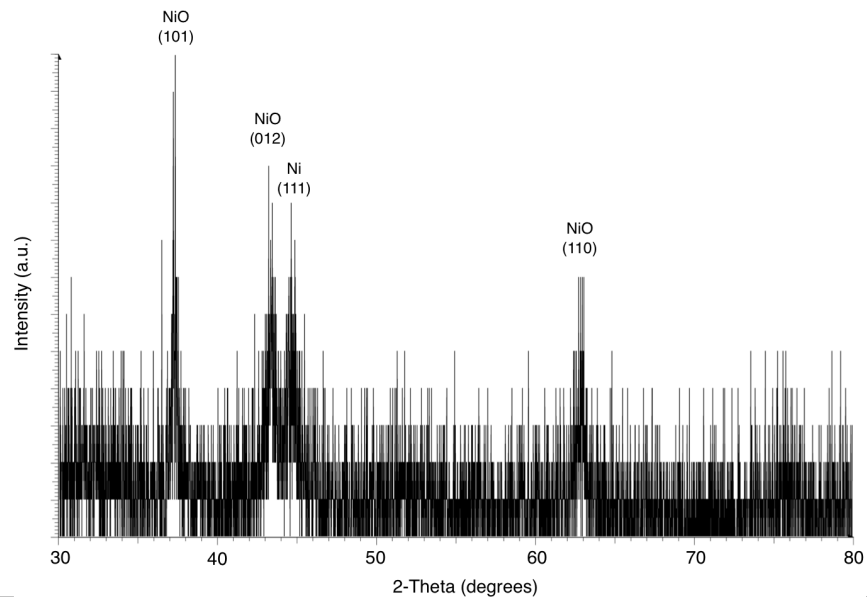


FIGURE B.1: XRD spectra of the sample  $S_1$ , deposited at a working pressure of  $2 \cdot 10^{-4}$  mbar.

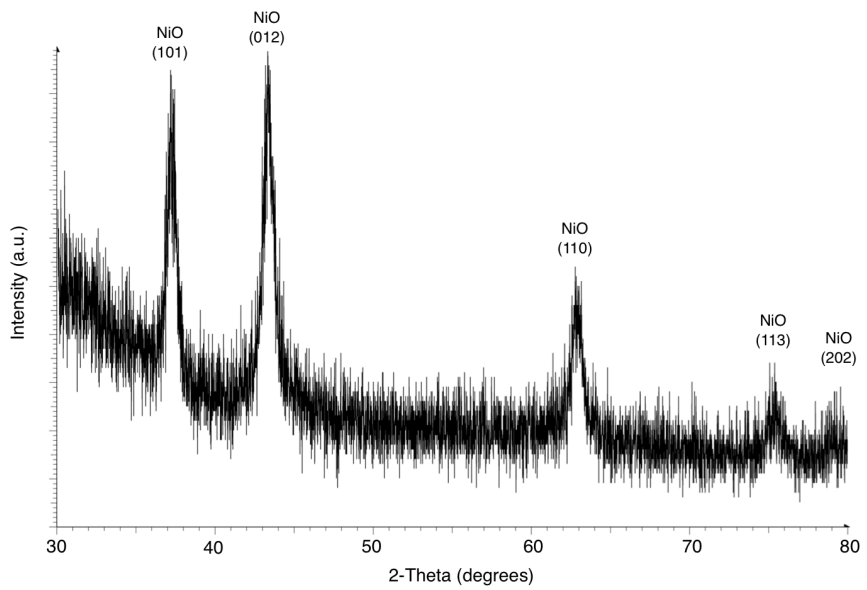


FIGURE B.2: XRD spectra of the sample  $S_2$ , deposited at a working pressure of  $6 \cdot 10^{-4}$  mbar.

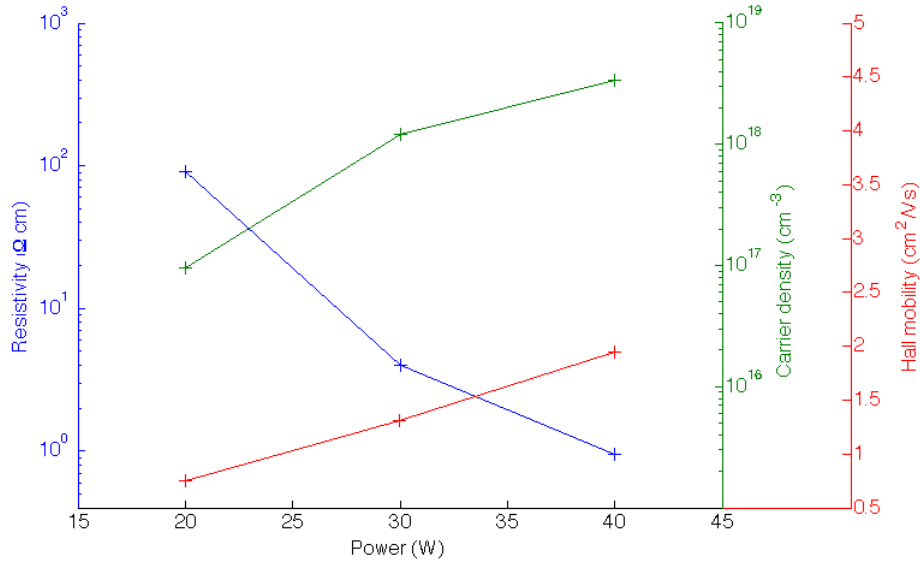


FIGURE B.3: Electrical properties as a function of Ni-target power of the Ni-doped ZnO films deposited on Si substrate, as obtained by Hall effect measurements.

## B.2 Ni-doped ZnO film deposition by magnetron sputtering

Section 3.6.4 presented a method for doping ZnO-bulk material by Ni from a pre-deposited Ni-doped ZnO film obtained by magnetron co-sputtering. Here, the development steps that were carried out in order to determine the optimal Ni-target power density will be described.

Three minor pieces of a Si wafer and three pieces of glass were used as test samples. One of each were deposited together for 60 min with a Ni-target (RF) power of 20, 30 or 40 W, yielding a film-thickness of 190 nm. The ZnO-target (RF) power was kept at 50 W for all three depositions. A temperature of 400°C, as well as a rotation of the samples at 12 rpm, was maintained during deposition. The sample chamber was evacuated to a base pressure of  $1.3 \cdot 10^{-6}$  mbar before a 70 sccm argon flow was established to yield a working pressure of 0.13 mbar. The electrical properties of the films were analyzed on the glass sample after each deposition by the use of a Lakeshore 7704A Hall effect measurement system. Figure B.3 shows the resistivity, carrier density and Hall mobility as a function of the Ni-target power used for the three depositions. The resistivity decreases with higher Ni-target power, while there is a concurrent increase in the hall mobility and carrier density. The increase in electron density suggests that Ni act as a donor or promotes the formation of intrinsic defects that act as donors.

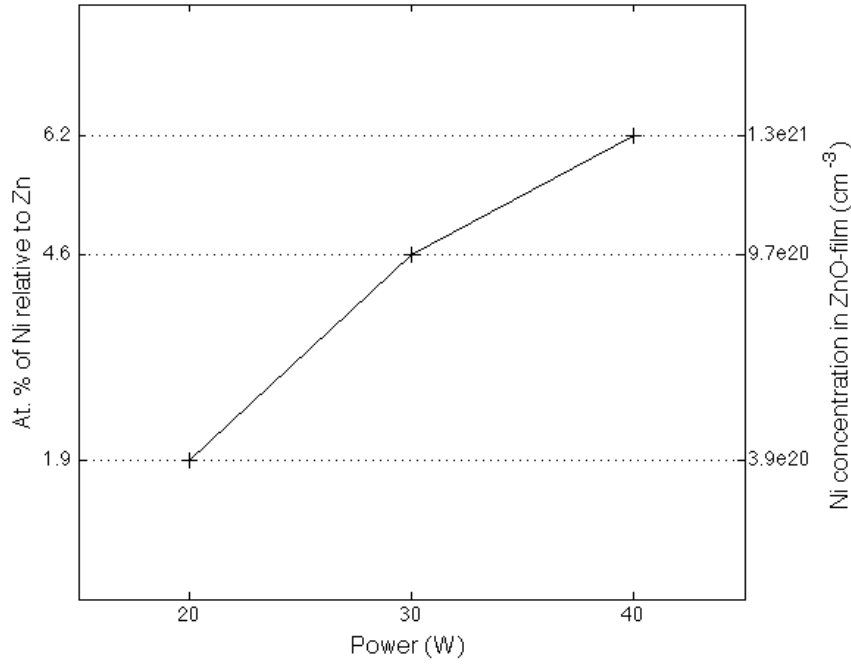


FIGURE B.4: Amount of Ni vs Ni-target power in the Ni-doped ZnO films deposited on Si substrates by magnetron co-sputtering, as measured by the EDS-detector in SEM. Both the measured at.% of Ni relative to Zn (left axis) and the corresponding estimated Ni concentration in the ZnO-film (right-axis) are shown. The ZnO target power was kept at 50 W.

For determining the Ni concentration in the films a Hitachi TM3000 tabletop Scanning electron microscope (SEM) was utilized. The built-in Energy-dispersive X-ray spectroscopy (EDS) detector was used to quantify the amount of Ni relative to Zn in the films deposited on the Si samples. Figure B.4 shows the measured at.% of Ni relative to the at.% of Zn for the films deposited by a Ni-target power of 20, 30 and 40 W. The SEM measurements were performed perpendicular to the film surface and thus any Ni or Zn impurities within the x-ray escape region in the Si bulk material could potentially contribute to the measured characteristic x-ray signal for the two elements. However, it is reasonable to assume that neither Zn or Ni are present in Si in notable concentration. For that reason it is presumed that the characteristic x-ray signal of the two elements originates from the film, and that the obtained Ni concentration relative to Zn is trustworthy.

## Appendix C

# Documentation of Python script

The Python script used to read SIMS data and model the diffusion profiles is given below.

---

```
#Script to read and model SIMS data from standard output file (.dp_rpc_asc)
#from Cameca IMS-7f at MiNaLab.
```

```
#Packages
```

```
from pylab import *; from collections import defaultdict
import matplotlib.pyplot as plt; from scipy import *
import scipy.optimize as optimize; import numpy as np
from scipy import special; import collections
```

```
#Read data from file
```

```
def read(d,i):
    for line in lines[16:]:
        if line.isspace() or len(line.split()) < 2*len(impurity):
            break
        else:
            value = line.split()
            k = 0
            for j in impurity:
                d[j]['Depth'].append(float(value[2*k]))
                d[j]['Intensity'].append((float(value[2*k+1])))
                k += 1
    return d
```

```
#Plot data
```

```
def data(d, i, Ni, colors):
    depth = d[impurity[Ni]]['Depth'] #Depth data
    C = d[impurity[Ni]]['Intensity'] #Concentration/intensity data
    temp1 = ['Data',lines[3].split()[-1]] #Extract ID name from file
    label = ': '.join(temp1)
    plt.figure(1)
    plt.plot(depth, C, colors[i], label=label)
    list = [lines[2].split()[-1][: -3], 'eps']
    filename = '.'.join(list)
```

```

#Model diffusion profiles, using the optimize.leastsq package
#based on the Levenburg-Marquardt gradient method to
#minimise the squared residuals
#between the model (erfc) and the measured profiles
def model(d, Ni, i, D, colors):
    depth = d[impurity[Ni]]['Depth']
    C = d[impurity[Ni]]['Intensity']
    Errorfunc = lambda q, x: q[0]*special.erfc(x/(2*sqrt(q[1]))) #Model
    Residuals = lambda q, x, y: Errorfunc(q, x) - y #Residuals to be minimized
    Param = collections.namedtuple('Param','C0 Dt')
    q_guess = Param(C0=1.e20, Dt=0.02)
    q, cov, infodict, mesg, ier = optimize.leastsq(Residuals,
                                                    q_guess, args=(depth[:], C[:]),
                                                    full_output=True, maxfev=10000)

    q=Param(*q) #Solution
    print q

    time = 1*90*60.
    diffusivity = 'D = '+ repr(q[1]*10**(-8)/time)
    print diffusivity
    D.append(np.log((q[1]*10**(-8))/time)) #Given depth values in microns
    label = 'Fit - erfc'
    figure(1)
    plt.plot(depth, Errorfunc(q, depth), colors[-1], label=label)
    return D

#Estimate activation energy and pre-exponential factor
def arrhenius(D):
    kelvin = 273.15
    T = [950, 1000, 1050, 1100] #Relevant treatment temperatures (Celsius)
    k = 8.617e-5 # Boltzmann constant (eV/K)
    K = [1./(T[0]+kelvin), 1./(T[1]+kelvin),
          1./(T[2]+kelvin), 1./(T[3]+kelvin)]
    (Ea,b) = polyfit(K,D,1) #Least squares polynomoal fit of degree 1

    yp = polyval([Ea,b],K) #Evaluate polynomial at the specific values
    fig = plt.figure(2)
    plt.plot(K,exp(yp))
    plt.yscale('log')
    plt.ylabel('Diffusivity (cm$^2$s$^{-1}$)')
    plt.xlabel('1/T (K$^{-1}$)')
    ticklabel_format(axis='x',style='sci',scilimits=(1,4))
    D0 = exp(b) #Pre-exponential facor
    Ea = Ea*k #Activation energy
    s = 'Ea for diffusion is Ea = '+ repr(Ea) +\
    ' eV, with D0 = '+ repr(D0)+' cm^2/s'
    print s

d = defaultdict(list) #Store data in dictionary
D = [] #Diffusivities
colors = ['k.','r.', 'g+', 'bx', 'g>', 'g', 'b', 'k'] #Plot-color

#Loop over data sets
#The file name(s) can be given as argument in the comand line
for i in range(len(sys.argv) - 1):

```

---

```
if len(sys.argv) < 2:
    filename = raw_input('Give filename:') #Message if file not given
else:
    filename = '/HomeDirectory/.../' + str(sys.argv[i+1])
f = open(filename, 'r')
lines = f.readlines()
f.close
impurity = []
impurities = lines[13]
impurity = impurities.split()
for p in impurity:
    d[p] = {}
    d[p]['Depth'] = []
    d[p]['Intensity'] = []
Ni = impurity.index('58Ni')
read(d, i)
data(d, i, Ni, colors)
model(d, Ni, i, D, colors)
if i==3: arrhenius(D)
if i<3:
    plt.xlabel('Depth ' + r'($\mu$m)', fontsize=15)
    plt.ylabel('Ni concentration (cm'+r'$^{-3}$)', fontsize=15)
    plt.yscale('log')
    plt.legend(loc='upper right')
plt.show()
```

---

# Bibliography

- [1] S. J. Pearton *et al.* Recent progress in processing and properties of zno. *Progress in Materials Science*, 50:293–340, 2005.
- [2] Ü. Özgür *et al.* A comprehensive review of zno materials and devices. *Journal of Applied Physics*, 98(041301), 2005.
- [3] C. Liu *et al.* Ferromagnetism of zno and gan: A review. *Journal of Materials Science: Materials in Electronics*, 6:555–597, 2005.
- [4] C. Kittel. Introduction to solid state physics. *John Wiley & Sons, Inc.*, 8 edition, 2005.
- [5] D. B. Holt and B. G. Yacobi. Extended defects in semiconductors: Electronic properties, device effects and structures. *Cambridge University Press*, 2007.
- [6] C. Angell and B.E. Lian. Fysiske størrelser og enheter - navn og symboler. *Universitetsforlaget*, 4 edition, 2004.
- [7] J. Philibert. One and a half century of diffusion: Fick, einstein, before and beyond. *Diffusion Fundamentals 2*, 2005. URL [http://www.uni-leipzig.de/diffusion/journal/pdf/volume2/diff\\_fund\\_2\(2005\)1.pdf](http://www.uni-leipzig.de/diffusion/journal/pdf/volume2/diff_fund_2(2005)1.pdf).
- [8] A. Fick. On liquid diffusion (translated and reprinted). *Journal of membrane science*, 100:33–38, 1995.
- [9] J. Philibert. Atom movements – diffusion and mass transport in solids. *Les Editions De Physique*, 1991.
- [10] S.A. Campbell. Fabrication engineering at the micro- and nanoscale. *Oxford University Press*, 4 edition, 2013.
- [11] M.E. Glicksman. Diffusion in solids – field theory, solid-state principles, and applications. *John Wiley & Sons, Inc.*, 2000.
- [12] A. Einstein. A. einstein, investigations on the theory of the brownian movement, edited with notes by r. furt. *Dover publications*, 1956.



- [13] D. Gupta and P.S. Ho. Diffusion phenomena in thin films and microelectronic materials. *Noyes Publications*, 1988.
- [14] D.V. Schroeder. An introduction to thermal physics. *Addison Wesley Longman*, 2000.
- [15] P.R. Griffiths and J.A. de Haseth. Fourier transform infrared spectrometry. *John Wiley & Sons, Inc.*, 2 edition, 2007.
- [16] D.J. Griffiths. Introduction to quantum mechanics. *Pearson Education Inc.*, 2 edition, 2005.
- [17] P.Y. Emelie *et al.* Free carrier absorption and lattice vibrational modes in bulk zno. *Journal of Electronic Materials*, 35(4):525–529, 2006.
- [18] L. Vines and A. Kuznetsov. Semiconductors and semimetals: Bulk growth and impurities. *Elsevier Inc.*, 88, 2013.
- [19] K. Maeda *et al.* Growth of 2 inch zno bulk single crystal by the hydrothermal method. *Semiconductor Science and Technology*, 20:49–54, 2005.
- [20] J. Nelson. The physics of solar cells. *Imperial College Press*, 2003.
- [21] J. L. Lyons *et al.* Semiconductors and semimetals: Theory and modelling of oxide semiconductors. *Elsevier Inc.*, 88, 2013.
- [22] C. G. Van de Walle and J. Neugebauer. Universal alignment of hydrogen levels in semiconductors, insulators and solutions. *Nature*, 423, 2003.
- [23] A. F. Kohan *et al.* First-principles study of native point defects in zno. *Physical Review B*, 61(22), 2000.
- [24] A. Janotti and C. G Van de Walle. Native point defects in zno. *Physical Review B*, 76(16), 2007.
- [25] O. F. Schirmer. The structure of the paramagnetic lithium center in zinc oxide and beryllium oxide. *J.Phys.Chem. Solids*, 29:1407–1429, 1968.
- [26] J. J. Lander. Reactions of lithium as a donor and an acceptor in zno. *J. Phys. Chem. Solids*, 15:324–334, 1960.
- [27] L. Vines *et al.* Lithium and electrical properties of zno. *Journal of Applied Physics*, 107, 2010.
- [28] M. G. Wardle *et al.* Theory of fe, co, ni, cu, and their complexes with hydrogen in zno. *Physical Review B*, 72(155108), 2005.

- [29] H. A. Weakliem. Optical spectra of  $\text{ni}^{2+}$ ,  $\text{co}^{2+}$  and  $\text{cu}^{2+}$  in tetrahedral sites in crystals. *The Journal of Chemical Physics*, 36(8), 1962.
- [30] R. S. Anderson. Lattice-vibration effects in the spectra of  $\text{zno:ni}$  and  $\text{zno:co}$ . *Physical Review*, 164(2), 1967.
- [31] U. Kaufmann *et al.* Near infrared absorption of  $\text{ni}^{2+}$  in  $\text{zno}$  and  $\text{zns}$ : Dynamic jahn-teller effect in the  $3t_2$  state. *Journal of Physics C: Solid State Physics*, 6, 1973.
- [32] E.V. Lavrov *et al.* Dominant hydrogen-oxygen complex in hydrothermally grown  $\text{zno}$ . *Physical review B*, 71, 2005.
- [33] E. V. Lavrov *et al.* Comment on “infrared absorption spectroscopy on  $\text{oh-ni}$  complex in hydrothermally grown  $\text{zno}$ . *Journal of Applied Physics*, 106, 2009.
- [34] E. V. Lavrov. Infrared absorption spectroscopy of hydrogen-related defects in  $\text{zno}$ . *Physica B*, 340–342:195–200.
- [35] E. V. Lavrov *et al.* Effect of uniaxial stress on substitutional  $\text{ni}$  in  $\text{zno}$ . *Solid State Communications*, 159, 2013.
- [36] H. Jahn and E. Teller. Stability of degenerate electronic states in polyatomic molecules. *Physical Review*, 49:874–880, 1936.
- [37] M. C. M. O’Brien and C. C. Chancey. The jahn-teller effect: An introduction and current review. *Am. J. Phys*, 61(8), 1993.
- [38] R. G. Wilson *et al.* Secondary ion mass spectrometry: A practical handbook for depth profiling and bulk impurity analysis. *John Wiley and Sons, Inc.*, 1989.
- [39] P. C. Zalm. Secondary ion mass spectrometry. *Vacuum*, 45(6).
- [40] P. Sigmund. Theory of sputtering. i. sputtering yield of amorphous and polycrystalline targets. *Physical Review*, 184(2):383–416.
- [41] M. K. Linnarsson. Compound semiconductors; defects and relocation of atoms during growth, sputtering and diffusion. (doctoral dissertation). *KTH, Royal Institute of Technology*, 1997.
- [42] P. Connes. Early history of fourier transform spectroscopy. *Pergamon Press Ltd*, 24:69–93, 1984.
- [43] D.A. Naylor and M.K. Tahic. Apodizing functions for fourier transform spectroscopy. *J. Opt. Soc. Am*, 24(11), 2007.

- [44] B.C. Smith. Fundamentals of fourier transform infrared spectroscopy. *CRC Press*, 2 edition, 2011.
- [45] F.M Smits. Measurement of sheet resistivities with the four-point probe. *Bell System Technical Journal*, 34:711 –718, 1958.
- [46] L.B. Valdes. Resistivity measurements on germanium for transistors. *Proceedings of the IRE*, pages 420–427, February 1954.
- [47] B.G. Streetman and S.K. Banerjee. Solid state electronic devices. *Prentice Hall*, 6 edition, September 2005.
- [48] J. P. Sethna. Statistical mechanics: Entropy, order parameters, and complexity. *Oxford University Press*, 2006.
- [49] N. H. Nickel. Hydrogen migration in single crystal and polycrystalline zinc oxide. *Physical Review B*, 73(195204), 2006.
- [50] P. T. Neuvonen *et al.* Intrinsic point-defect balance in self-ion-implanted zno. *Phys. Rev. Lett.*, 110(015501), 2013.
- [51] A. Yu. Azarov *et al.* Impurity sublattice localization in zno revealed by li marker diffusion. *Phys. Rev. Lett.*, 110(175503), 2013.
- [52] K. E. Knutsen *et al.* Diffusion and configuration of li in zno. *Journal of Applied Physics*, 113(023702), 2013.
- [53] L. E. Halliburton *et al.* Infrared absorption from oh- ions adjacent to lithium acceptors in hydrothermally grown zno. *Journal of Applied Physics*, 96(12), 2004.
- [54] G. Alvin Shi *et al.* Identification of an oh-li center in zno: Infrared absorption spectroscopy and density functional theory. *Physical Review B*, 73(8), 2006.
- [55] K. M. Johansen *et al.* Thermal stability of the oh-li complex in hydrothermally grown single crystalline zno. *Applied Physics Letters*, 97(211907), 2010.
- [56] H. J. Schulz and M. Thiede. Optical spectroscopy of 3d7 and 3d8 impurity configurations in a wide-gap semiconductor (zno:co,ni,cu). *Physical Review B*, 35(1), 1987.
- [57] H. Haug. Hydrogen-related defects in hydrothermally grown zno studied by fourier transform infrared spectroscopy, master’s thesis. *University of Oslo*, 2010.
- [58] M. D. McCluskey *et al.* Infrared spectroscopy of hydrogen in zno. *Applied Physics Letters*, 81(20), 2002.

- 
- [59] M.D. McCluskey and S.J. Jokela. Sources of n-type conductivity in zno. *Physica B*, 441–402:355–357, 2007.
- [60] E.V. Lavrov *et al.* Hydrogen motion in zno. *Physica B*, 401–402:366–369, 2007.
- [61] E. V. Lavrov *et al.* Copper dihydrogen complex in zno. *Physical review B*, 77(15), 2008.